UNIVERSIDAD DE CONCEPCIÓN
FACULTAD DE INGENIERÍA
Departamento de Ingeniería Química

Incorporación de nuevos elementos a la topología global de fases: Elementos de química computacional, sistemas ternarios y comportamiento no-clásico de la región crítica

por

Mauricio Flores Ruiz

Tesis presentada a la

Escuela de Graduados de la Universidad de Concepción

para optar al grado de

Doctor en Ciencias de la Ingeniería
con Mención en Ingeniería Química

Profesor Patrocinante: Dr. Hugo Segura
Profesor Comisión Interna: Dr. Andrés Mejía
Profesor Comisión Externa: Dr. José Valderrama

Ciudad Universitaria, marzo 2013

SUMARIO

Numerosos procesos tecnológicos y naturales ocurren en sistemas heterogéneos, caracterizados por fases de propiedades mecánicas distintas y constituidos por mezclas de componentes de diversa naturaleza físico-química. La fuente convencional de información de equilibrio de fases es la experimentación directa sobre las mezclas a separar, metódica que suele estar caracterizada por un alto costo de infraestructura, además de elevados costos de operación y tiempo. Sin embargo, el desarrollo de modelos físicos, llámese modelos de exceso, ecuaciones de estado (EOS) o el enfoque de dinámica molecular, han permitido conocer el comportamiento de mezclas sin la necesidad de experimentar en todo el rango. Una EOS permite, a través de un modelo común, conocer el comportamiento de una mezcla y reducir notablemente los costos de infraestructura, operación y tiempo. En tal sentido la Teoría Estadística del Fluido Asociado (SAFT), es una muy buena herramienta para intra y extrapolar comportamientos de equilibrio de fases, considerando su inpiración teórico-molecular y su buena representación de la realidad.

El desarrollo de un Diagrama Global de Fases con una EOS como SAFT es una potente herramienta, pues permite conocer el comportamiento de una mezcla en todo el rango de condiciones. En tal dirección es que esta investigación incorpora la región de la corona, condición de alta presión donde el comportamiento de las líneas críticas presentan inflexiones. Las mezclas que presentan este tipo de comportamiento son candidatas a extracción supercrítica. La conducta barotrópica, que corresponde a la inversión de densidades másicas, es estudiada a profundidad, encontrándose un mecanismo transicional válido para equilibrios heteroazeotrópicos, probado en los sistemas CO_2+n-alcanos y perfluroalcanos+n-alcanos.

Por una parte se verifica la buena correspondencia entre el comportamiento experimental y el predicho por SAFT. Esto entrega confianza de la extrapolación de comportamientos, encontrándose fenómenos bastante particulares en la región de altas presiones. Desde un punto de vista estructural, el hecho de que una EOS como SAFT considere formalmente el efecto de forma a través de un término de cadena, permite obtener regiones de

miscibilidad del equilibrio de fases, mayores que EOS que incluyen el efecto de forma a través del factor acéntrico.

Finalmente el estudio de la barotropía, propició el desarrollo de un mecanismo transicional consistente termodinámicamente hablando y con buena concordancia del comportamiento experimental válido para sistemas asimétricos.

AGRADECIMIENTOS

- Al Departamento de Ingeniería Química y a la Escuela de postgrado de la Universidad de Concepción.
- Al programa MECESUP y CONICYT por el financiamiento otorgado para llevar a cabo mis estudios de postgrado.
- Al Dr Hugo Segura, profesor patrocinante de la presente tesis, por su apoyo y dirección.
- Al Dr Andrés Mejía cuyos consejos fueron importantes en esta investigación.
- A CCTE-UDT, que ha permitido insertarme al mundo laboral y financió la presentación de los resultados de este trabajo en Europa.
- A mi familia, padres y hermanos, por todo el apoyo y comprensión, que hicieron de este largo proceso una experiencia más grata.
- A Rafael y Christian, por su apoyo y consejos que fueron muy importantes en el periodo de mis estudios doctorales
- A mis amigos por su apoyo y los buenos momentos que me han brindado.

TABLA DE CONTENIDOS

NOMECLATURA Y SIMBOLOGIA I

ABREVIACIONES I

INDICE DE FIGURAS II

INDICE DE TABLAS III

CAPITULO I

1. INTRODUCCION 1
   - 1.1. Antecedentes Generales 1
   - 1.2. Aproximación sistemática al problema de equilibrio de fases 1
   - 1.3. Ecuaciones de estado 3
   - 1.4. Fluidos SAFT 4
   - 1.5. Concepto de Globalidad Topológica 6
     - 1.5.1. Diagrama Global de Fases 8
   - 1.6. Motivación y Objetivo 11

CAPITULO II

2. TOPOLOGIA GLOBAL DE FASES 12
   - 2.1. GPD para la EOS SAFT. Moléculas de igual diámetro 13
     - 2.1.1. Región de la Corona 16
   - 2.2. GPD modelo SAFT. Moléculas de distinto diámetro 18
   - 2.3. Efecto de la contribución de longitud de cadena en la topología global 20
   - 2.4. Aplicación práctica de la teoría de GPD 22
     - 2.4.1. spd-GPD 22
     - 2.4.2. spd-GPD CH_4+ n-alcanos 24

2.4.3. spd-GPD CO_2+ n-alcanos 27

CAPITULO III

3. COMPORTAMIENTO BAROTROPICO EN EL EQULIBRIO TRIFASICO 31
3.1. Barotropía*: Un gas que se hunde en un líquido* 31
3.2. Aproximación a la descripción de la barotropía 31
3.3. Aproximación topológica a la barotropía en mezclas binarias asimétricas 33
3.3.1. Límite Barotrópico para una serie homóloga 36
3.3.2. Discusión desde un perspectiva experimental de la serie CO_2 + n-C_nH_{2n+2} 38
3.3.3. Análisis Perfluoroalcanos + n-C_nH_{2n+2} 39

CAPITULO IV

4. Condiciones límites para el comportamiento de plato de presión en el Diagrama Global de Fases de mezclas binarias compuestas por moléculas esféricas de igual tamaño 42

CAPITULO V

5. Aproximación topológica del fenómeno barotrópico másico en mezclas asimétricas 55

CONCLUSIONES 67

ANEXOS

Anexo I: Equilibrio de Fase y tensión interfacial en sistemas metil tert butil éter+ acetona+ciclohexano, metil tert butil éter+acetona y metil tert butil éter+ciclohexano 70

REFERENCIAS 82

NOMECLATURA Y SIMBOLOGIA

A	:	función de energía de Helmholtz
a		parámetro cohesivo de la ecuación de estado
b	:	covolumen de la ecuación de estado
G	:	energía de Gibbs
k_{12}	:	parámetro de interacción de la regla de mezclado para el término cohesivo
M	:	Masa molar
N	:	número de carbonos de la serie alifática
P	:	Presión
R	:	constante universal de los gases
T	:	temperatura absoluta
V	:	Volumen
X	:	fracción molar

Símbolos Griegos

ξ	:	diferencia de diámetro molecular
ζ	:	diferencia de energía cohesiva a presión infinita
λ	:	efecto de mezclado por moléculas distintas
ρ	:	Densidad
σ	:	diámetro molecular
μ	:	Potencial químico
η	:	fracción de empaquetamiento

ABREVIACIONES

BP	:	Punto de inversión barotrópico
CS	:	relativo al término de esfera rígida Carnahan-Starling
DCEP		Punto crítico terminal doble
EOS	:	relativo a la ecuación de estado

GPD	:	relativo al Diagrama Global de Fases
LCEP	:	punto terminal crítico inferior
LGE	:	relativo al equilibrio líquido-gas
LLE	:	relativo al equilibrio líquido-líquido
LLG	:	relativo al equilibrio líquido-líquido-gas
RK	:	relativo a la ecuación Redlich Kwong
TC		Transición tricrítica
UCEP	:	punto terminal crítico superior
vdW	:	relativo a la ecuación de van der Waals

INDICE DE FIGURAS

Figura 1.1	:	Proceso de formación de moléculas de cadena y de asociación de esferas duras en el modelo de SAFT
Figura 1.2	:	Tipos Topológicos clásicos predichos por la EOS vdW
Figura 1.3	:	Diagrama Global de Fases para el modelo de van der Waals
Figura 2.1	:	GPD para la EOS SAFT ξ =1 y m_1=m_2=1
Figura 2.2	:	Transición Tipo I^h-II
Figura 2.3	:	Región de la corona para la EOS SAFT ξ =1 y m_1=m_2=1
Figura 2.4	:	GPD moléculas de distinto tamaño y forma molecular para EOS SAFT m_1=1;m_2=6
Figura 2.5	:	GPDs de vdW y RK con igual razón de tamaño molecular que el GPD para modelo SAFT con m_1=1;m_2=6
Figura 2.6	:	Representación esquemática del spd-GPD
Figura 2.7	:	Relación entre propiedades moleculares y número de carbonos para la serie de hidrocarburos
Figura 2.8	:	spd-GPD modelo SAFT para serie CH_4+n-alcanos

Figura 2.9 : spd-GPD modelo PC-SAFT para mezcla CO_2+n-alcanos

Figura 3.1 : Esquema del experimento realizado por Kamerlingh Onnes en el que observó el fenómeno de inversión de densidades

Figura 3.2 : Comportamiento de equilibrio de fases para CO_2+n-C^*

Figura 3.3 : spd-GPD para la serie CO_2+n-alcano

Figura 3.4 : Equilibrio de fases representativo de un sistema Tipo II con comportamiento barotrópico

Figura 3.5 : Equilibrio de fases en la vecindad del cruce CMaDIEP y DCEP

Figura 3.6 : spd-GPD para la serie CF_4+$C_{2n}H_{2n+2}$ y C_2F_6+$C_{2n}H_{2n+2}$

INDICE DE TABLAS

Tabla 2.1 : Parámetros moleculares del CO_2 para el modelo PC-SAFT

Tabla 2.2 : Parámetros correlación propiedades moleculares de n-alcanos con M, en el modelo PC-SAFT

CAPITULO I

1. INTRODUCCION

1.1 Antecedentes Generales

Numerosos procesos tecnológicos y naturales ocurren en sistemas heterogéneos, caracterizados por fases de propiedades mecánicas distintas y constituidos por mezclas de componentes de diversa naturaleza físico-química. En el campo de la Ingeniería Química aplicada, los procesos de separación y purificación son los más relevantes. Un caso tradicional lo constituye la operación de destilación isobárica (Henley, 1981) de la que es posible obtener productos finales o intermedios de alta pureza para propósitos comerciales. La extracción líquido-líquido es una tecnología de separación alternativa cuando la destilación no es una opción comercial, o técnicamente factible, como es el caso de la purificación de mezclas azeotrópicas, o aquellas que contienen componentes termolábiles (Gaubert *et* al, 2001). En la actualidad, y en forma cada vez más frecuente, las operaciones de separación de alta presión adquieren una creciente importancia. El ejemplo más típico de este tipo de aplicación es la extracción supercrítica desde sólidos y desde mezclas fluidas de baja volatilidad, que contienen componentes termosensibles (McHugh, 1994; Chang *et* al., 2000). Aplicaciones más especializadas del concepto de equilibrio de fases las constituyen la planificación operativa de yacimientos petrolíferos (Firoozabadi, 1999), el tratamiento de residuos peligrosos en ambientes supercríticos que favorecen su oxidación a bajas temperaturas (Savage, 1999), entre otras muchas aplicaciones.

1.2 Aproximación sistemática al problema de equilibrio de fases

En décadas pasadas, gran parte del trabajo realizado en el área de separaciones físicas o químicas provenía del conocimiento empírico. Sin embargo, el desarrollo de modelos físicos, llámese modelos de exceso, ecuaciones de estado (EOS) o el enfoque de dinámica molecular, han permitido conocer el comportamiento de fluidos sencillos en un rango amplio de condiciones. La capacidad predictiva de los modelos disponibles se debilita al

considerar fluidos complejos, entendiendo por ellos a las mezclas de moléculas con propiedades dominadas por geometría molecular e interacciones de fuerza tales como la asociación, polaridad y carga eléctrica. Esta problemática ha llevado a la comunidad científica a realizar numerosos esfuerzos por mejorar la representación que los enfoques mencionados pueden realizar de fluidos complejos. Obviamente, debido a la complejidad física y matemática, no existe una teoría unificada que permita representar todos los fenómenos físicos que, a nivel molecular, originan el comportamiento macroscópico de un fluido puro y sus mezclas.

La fuente convencional de información de equilibrio de fases es la experimentación directa sobre las mezclas a separar, metódica que suele estar caracterizada por un alto costo de infraestructura, además de elevados costos de operación y tiempo.

Un diagrama de equilibrio de una mezcla binaria entrega información limitada, aunque valiosa, para explorar la síntesis y las condiciones de separación de corrientes de interés industrial. Mezclas de más componentes aumentan el tiempo de experimentación y los costos de operación en un factor de potencia del orden del número de componentes. La determinación de sistemas de alta presión, dependiendo del rango de operación, aumenta los costos de experimentación en un factor 2 a 5 (Flores, 2003). Por estas razones, aunque la práctica experimental es ineludible para la generación de información precisa y confiable, el apoyo de modelos empíricos o teóricos permite guiar y sugerir condiciones de experimentación que propenden a:

- optimizar las condiciones termomecánicas de una tecnología de separación, basada en una exploración experimental de costo más razonable.
- explorar con detalle fenómenos singulares de interés teórico, como la evolución de azeótropos, la aparición de rangos de inmiscibilidad, rangos de fenómenos retrógrados, barotropía, entre otros.

Todo modelo útil para el tratamiento del equilibrio de fases de mezclas reales debe cumplir un conjunto mínimo de requisitos, entre los que cabe mencionar: una capacidad de ajuste razonable para interpolar información experimental, un respaldo teórico suficiente para extrapolar cualitativamente información experimental limitada y obtener predicciones confiables, una demanda de

cómputo razonable para aplicaciones prácticas y, finalmente, una generalidad que lo haga aplicable a una amplia variedad de mezclas y condiciones. Una ecuación de estado aplicable a fases fluidas en amplios rangos de densidad es la que mejor califica como potencial descriptor de fases (Anderko, 1990).

1.3 Ecuaciones de estado

Las ecuaciones de estado han asumido un papel cada vez más preponderante en la sistematización del equilibrio de fases, en la predicción de propiedades energéticas y de transporte.

El énfasis de su desarrollo apunta a la posibilidad de aplicarlas al cálculo de las propiedades de mezclas arbitrarias. Para alcanzar este objetivo predominan dos enfoques alternativos.

- un primer enfoque basado en la reestructuración empírica de modelos sencillos (es decir, ecuaciones cúbicas del tipo Van der Waals, con reglas de mezclado mejoradas) (Valderrama, 2003).
- un segundo enfoque, más mecanicista, está basado en un principio de estados correspondientes más amplio, que incluye un conjunto descriptivo de parámetros moleculares representativos de la estructura y fuerza molecular, sobre modelos matemáticos más coherentes de origen mecánico-estadístico. (Flores, 2003)

Las EOS de origen teórico-molecular constituye la vía adecuada para predecir equilibrios de fase en todo el rango de condiciones. La construcción de este tipo de modelos implica un conocimiento avanzado de leyes de fuerza intermolecular, mecánica estadística y cuántica, más el apoyo de la simulación molecular. Para que el modelo sea general, debe incorporar en su estructura numerosas consideraciones físicas tales como la posibilidad de asociación, la longitud y forma de la cadena molecular y los efectos anisotrópicos de las interacciones electroestáticas. Normalmente, el resultado de una ecuación teórico-molecular es una construcción funcional, cuyos parámetros tienen significado físico en la estructura molecular, o pueden ser determinados mediante un *tour- de- force* de experimentos de simulación molecular. También se utilizan, a modo de referencia, resultados analíticos de problemas sencillos,

como el caso de las propiedades de un fluido compuesto por esferas rígidas. Ciertamente, las ecuaciones de origen molecular pueden ser utilizadas para correlacionar datos experimentales, incluso existen casos en que el ajuste es superior al de las cúbicas convencionales. Sin embargo, el verdadero valor de un modelo de inspiración molecular radica en su capacidad de predecir el equilibrio de fases y medir el impacto que sobre él tiene la estructura molecular. Una vez comprendido el impacto específico de la estructura, es posible desarrollar modelos más simples y razonables para propósitos de aplicación en cálculos de ingeniería.

1.4 Fluidos SAFT

Recogiendo toda experiencia previa de modelado e introduciendo la teoría de Wertheim (1984a, 1984b, 1986a, 1986b), Chapman *et* al. (1990) y Huang & Radosz (1990) desarrollaron la teoría estadística de fluido asociado (SAFT), que entrega excelentes resultados para fluidos puros y mezclas que asocian. SAFT es una de las EOS más exitosas y con mejor respaldo teórico (Sadus, 2000). Esto se fundamenta en que no es una EOS específica, pues permite incorporar de manera aditiva, con un sólido respaldo físico y en base a una referencia que puede modificarse, los efectos de asociación, la conformación de cadena molecular, interacciones cuadrupolares y de electrolitos entre otros. El modelo original desarrollado por Chapman (1990), utilizado en esta tesis, considera que la energía de Helmholtz residual corresponde a una suma de términos que incluyen: repulsiones de corto rango, fuerzas dispersivas de largo rango, formación de cadenas químicamente estables y asociación o solvatación entre diferentes moléculas (Flores, 2003).

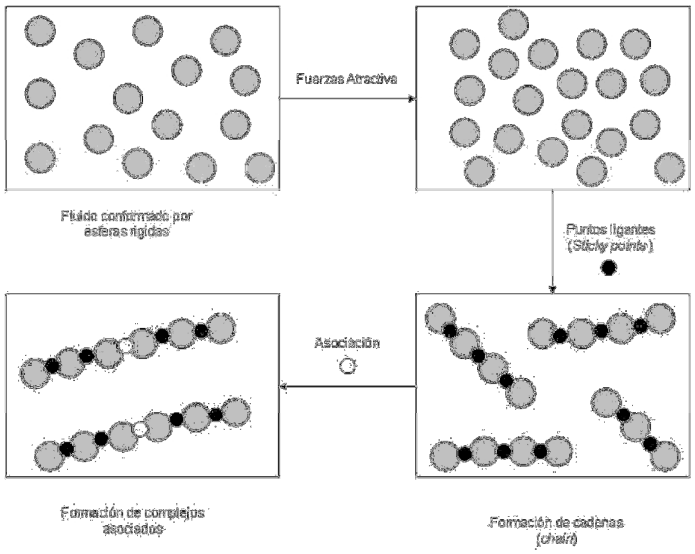

Figura 1.1 Proceso de formación de moléculas de cadena y de asociación de esferas duras en el modelo de SAFT (Prausnitz, 1986).

La flexibilidad de la EOS SAFT ha permitido que se realicen numerosas modificaciones, dirigidas a ampliar su rango de aplicación a fluidos cada vez más complejos, a través de términos con significado físico más que de ajuste experimental. Vega & Blas (1997) propusieron una versión de SAFT mediante la extensión de la teoría de Wertheim de primer orden para fluidos Lennard-Jones, basados en el trabajo de Johnson et al.(1993), tal extensión se conoce como Soft-SAFT y ha sido probada con bastante éxito en sistemas complejos tales como hidrocarburos pesados (2001), homopolímeros (2002) y perfluoralcanos (2004). Por otro lado Jackson et al. (1997) desarrollaron una variación de SAFT que considera un potencial de interacción de rango variable, SAFT-VR. Variaciones muy particulares hacen referencia a la aplicación de SAFT a mesofases en lo que se conoce como SAFT-LC y que fue desarrollada por Thies (2007), combinando el modelo SAFT de Huang y Radoz (1990) con la teoría dispersiva para cristales líquidos de Maier-Saupe (1958, 1959, 1960) y a líquidos iónicos en lo que se conoce como tPC-PSAFT (Peters, 2006, Karakatsani, 2007). Una de las variaciones más populares en la actualidad, corresponde a la desarrollada por Gros & Sadowski (2001) que incorpora un término dispersivo a la formación de cadena, originando PC-SAFT, el cual se muestra a continuación:

$$\frac{A^{disp}}{RT} = \frac{A_1}{RT} + \frac{A_2}{RT} \tag{1.1}$$

$$\frac{A_1}{RT} = -2\pi\rho\frac{\varepsilon}{k_B T} m^2\sigma^3 I_1(\rho, m) \tag{1.2}$$

$$\frac{A_2}{RT} = -\pi\rho m\left[\frac{\partial}{\partial\rho}\rho\left(1 + Z^{hc}\right)\right]^{-1}\left(\frac{\varepsilon}{RT}\right)^2 m^2\sigma^3 I_2(\rho, m) \tag{1.3}$$

$$I_1(\eta, m) = \sum_{i=0}^{6} a_i(m)\eta^i \tag{1.4}$$

$$I_2(\eta, m) = \sum_{i=0}^{6} b_i(m)\eta^i \tag{1.5}$$

donde a_i y b_i dependen sólo de la longitud de cadena, más detalles pueden encontrarse en el texto principal de Gros & Sadowski (2001). Tan buenos resultados ha mostrado, que se ha incorporado en la última versión del simulador de procesos ASPEN. Por la sólida base teórica, buena predicción y ajuste de información experimental fue utilizada en esta tesis, como herramienta para estudiar el equilibrio topológico de fases.

1.5 Concepto de Globalidad Topológica

El concepto de Globalidad Topológica, como sus alcances, son poco conocidos en el ámbito de la Ingeniería Química. La aplicación sistemática de este enfoque, a través de la construcción de un diagrama maestro, conocido como GPD (sus siglas en inglés), introducido en el trabajo seminal de Van Konyneburg & Scott (1980), ha estado orientado principalmente a la investigación topológica del equilibrio de fase, en busca de una mejor comprensión del modelo molecular (EOS) que lo genera, siendo calculado para un número limitado de EOS, relativamente sencillas, tales como Van der Waals (van Konyneburg, 1980), Dieterici (Kolafa, 2004; Segura, 2004), Redlich-Kwong (Boshkov, 1997), Lennard-Jones (Boshkov, 1984), y en condiciones en las que, siendo informativas, difícilmente son aplicables en fluidos reales. Otra dirección menos explorada, es su empleo para la comprensión de un fenómeno particular del equilibrio de fases, que se encuentra localizado en una región específica dentro del GPD, en éste ámbito, Bidart (2007) presentó un profundo

trabajo sobre lagunas de inmiscibilidad con el modelo CSvdW, y Kraska (1999) utilizando una vdW-SAFT[1] realizó algunos estudios preliminares del impacto de la longitud de cadena molecular en la topología global de fases.

La historia moderna del equilibrio de fases comienza con la exploración computacional sistemática que Van Konynenburg & Scott (Van Konynenburg, 1698; Scott, 1970, Van Konynenburg, 1980) llevaron a cabo para los diagramas de fases de sistemas binarios derivados desde la ecuación de Van der Waals, para moléculas de igual tamaño. Establecieron una clasificación *Tipo* de los posibles comportamientos que dicho modelo, aplicado a la descripción de sistemas binarios, podía representar en función del comportamiento de las líneas críticas, existencia y evolución de equilibrios azeotrópicos, heteroazeotrópicos, patrones de inmiscibilidad, condensados en una proyección P-T, y que por lo tanto, permite inferir todos los diagramas de equilibrio de una mezcla con componentes específicos. La clasificación contempla seis *Tipos* que son presentados en la Figura 1.2, todos ellos con respaldo experimental, de los cuales los cinco primeros pueden ser obtenidos a partir del modelo de Van der Waals original (para más detalles, ver Flores, 2003).

[1] Corresponde una cúbica convencional que incorpora el término de longitud de cadena tipo SAFT.

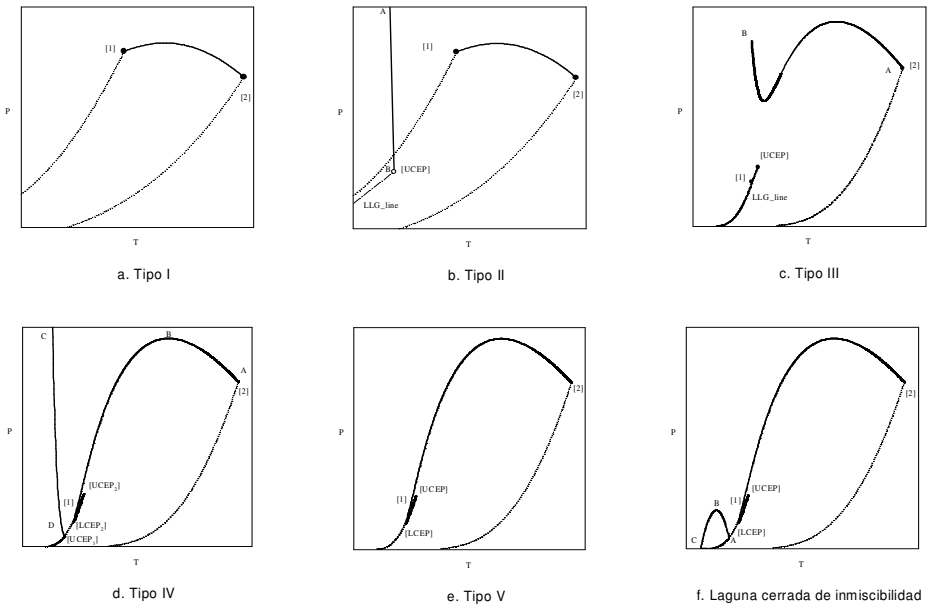

Figura 1.2 *Tipos* Topológicos clásicos predichos por la EOS vdW. (—): línea crítica. (···): presión de vapor. (–·–): línea heteroazeotrópica.

1.5.1 Diagrama Global de Fases

El Diagrama Global de Fases (GPD) constituye la representación más general del equilibrio de fases que un modelo representa para un sistema binario de composición arbitraria e incluye, en forma inequívoca, todos los *Tipos* topológicos que una ecuación de estado dada, puede predecir para mezclas de dos componentes. Desde un punto de vista formal, un GPD es un principio de estados correspondientes de mezclas, donde cada punto corresponde a uno de los *Tipos* mostrados en la Figura 1.2. De esta forma, cuando un GPD de un modelo específico revela la inexistencia de un determinado *Tipo*, el modelo de ecuación de estado en que se basa *no es aplicable* para interpolar o predecir una mezcla experimental que presenta la evidencia de dicho *Tipo*. Como se aprecia en la Figura 1.3, el GPD en su concepción original, es un gráfico plano cuyas coordenadas dependen, en el caso de *EOS de* tipo *Van der Waals*, de los parámetros a_i, b_i (parámetro cohesivo y covolumen del componente puro) y del parámetro de interacción k_{12}, característico de la mezcla.

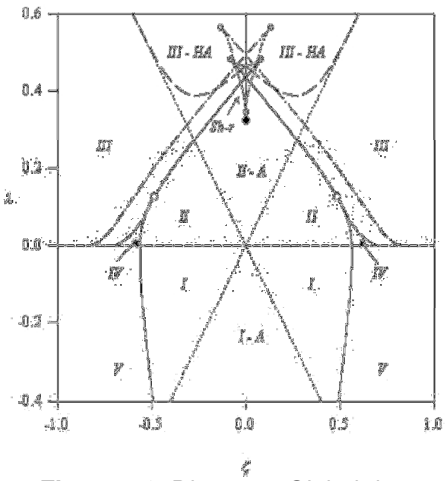

Figura 1.3 Diagrama Global de Fases para el modelo de van der Waals.

Definición de parámetros del GPD de la ecuación de Van der Waals

$$\zeta = \frac{a_2/b_2^2 - a_1/b_1^2}{a_2/b_2^2 + a_1/b_1^2}$$

$$\lambda = \frac{a_2/b_2^2 - 2\sqrt{a_1 a_2}\,(1-k_{12})/(b_1 b_2) + a_1/b_1^2}{a_2/b_2^2 + a_1/b_1^2}$$

$$\xi = \frac{b_1 - b_2}{b_1 + b_2}$$

Como se sigue del modelo de Van der Waals, el parámetro cohesivo y el covolumen de componentes puros se calculan a partir de sus propiedades críticas según las ecuaciones:

$$a_i = \frac{27\,(RT_{c,i})^2}{64\quad P_{c,i}} \qquad ; \qquad b_i = \frac{1\;\;RT_{c,i}}{8\quad P_{c,i}} \tag{1.6}$$

o bien pueden ser relacionados con propiedades de estructura molecular, alcanzando las siguientes definiciones

$$a_i = \frac{2}{3}N_{av}^2\pi\sigma_i^3\varepsilon_i \quad ; \quad b_i = \frac{2}{3}N_{av}\pi\sigma_i^3 \tag{1.7}$$

donde σ corresponde al diámetro molecular de empaque y ε es el pozo del potencial de dispersión. En tal sentido es posible establecer una generalización de las coordenadas de un GPD en función de propiedades moleculares y que permite su implementación en EOS de origen mecanicista-molecular:

$$\xi = \frac{\sigma_2^3 - \sigma_1^3}{\sigma_2^3 + \sigma_1^3} \tag{1.8}$$

$$\zeta = \frac{\frac{\varepsilon_2}{\sigma_2^3} - \frac{\varepsilon_1}{\sigma_1^3}}{\frac{\varepsilon_2}{\sigma_2^3} + \frac{\varepsilon_1}{\sigma_1^3}} \tag{1.9}$$

$$\lambda = \frac{\frac{\varepsilon_2}{\sigma_2^3} - 2\frac{\varepsilon_{12}}{\sigma_{12}^3} + \frac{\varepsilon_1}{\sigma_1^3}}{\frac{\varepsilon_2}{\sigma_2^3} + \frac{\varepsilon_1}{\sigma_1^3}} \tag{1.10}$$

En las definiciones (1.8)-(1.10):

- ξ es una variable representativa de la diferencia de tamaño molecular entre los componentes. Cuando ξ es nulo, las moléculas constituyentes de una mezcla poseen igual volumen de influencia, dando origen a soluciones tipo Porter que están caracterizadas sólo por efectos de fuerza.
- ζ establece la diferencia de densidad de energía de cohesión entre moléculas de distinto tipo que componen una mezcla binaria. Normalmente, el parámetro es creciente con la temperatura crítica de la especie 2 (o en su defecto el pozo potencial). El orden de magnitud del valor absoluto de ζ correlaciona directamente con la diferencia de volatilidad de las especies puras.
- λ contiene información específica acerca de la densidad de energía de cohesión que caracteriza a la interacción molecular entre especies distintas.

Las distintas regiones de un GPD se encuentran delimitadas por *criterios transicionales*, que corresponden a curvas paramétricas que definen áreas de comportamientos específicos de fases o sistemas *Tipo*. En el enfoque de una EOS, las curvas representativas de las transiciones entre *Tipos* dependen directamente de los parámetros del modelo. Es claro que modelos de EOS con una mejor base teórica encuentran una interpretación física de sus parámetros y, en estos casos, los GPD vinculan los eventos de equilibrio de fases con la estructura molecular, interacciones de fuerza y sinergia del mezclado. Por lo tanto, las potencialidades del GPD para establecer una predicción del equilibrio de fases, en un rango de aplicaciones donde es difícil y costoso experimentar, son notables pues, claramente:

- dado un componente de propiedades críticas conocidas, es posible determinar un segundo componente que posea una tipificación deseable de equilibrio de fases, dando origen a un principio de diseño molecular de solvente.
- conocido el comportamiento global de una mezcla, desde un punto de vista experimental, es posible inferir información de estructura molecular o de la capacidad del modelo para predecirlo.
- cada línea paramétrica del diagrama global de fases corresponde a un mecanismo de transición, o principio transicional, que establece continuidad del comportamiento del equilibrio de fases en función de propiedades críticas o estructura molecular. El GPD establece la posibilidad de analizar series homólogas de componentes de mezclas binarias que originan cambios topológicos radicales en el comportamiento de las transiciones de fases.

Son claras las ventajas que entrega el GPD, sin embargo, es importante indicar que esta herramienta no reemplaza la experimentación sino más bien colabora prediciendo patrones y comportamientos del equilibrio de fases que tienen respaldo empírico.

1.6 Motivación y Objetivo

En función de los argumentos presentados, es que esta investigación plantea como objetivo central profundizar en el comportamiento fases de mezclas binarias. En primera instancia, se busca realizar una investigación topológica del comportamiento del equilibrio de fases, mediante la aplicación sistemática de la teoría de GPD a una ecuación teórico-molecular tipo SAFT, permitiendo calificar, clasificar y cuantificar los efectos de la estructura, fuerza y forma molecular. En segunda instancia, se analizará eventos particulares del equilibrio de fases, en función de parámetros moleculares, definiendo si fuese posible, mecanismos transicionales a nivel global y el contraste de la predicción con la información experimental. Por cierto, que esto implica el desarrollo de nuevos elementos metodológicos, que abarcan desde el cálculo numérico

hasta el desarrollo de nuevas representaciones topológicas del comportamiento global del equilibrio de fases.

CAPITULO II

2. TOPOLOGIA GLOBAL DE FASES

Como se indicó en la sección 1.5, los GPDs han sido calculados para un número limitado de modelos de EOS, y aun cuando son informativos, difícilmente son aplicables a fluidos reales. En lo que respecta a SAFT, quizás el esfuerzo más notable hasta la fecha, es el trabajo de Kraska (1999) quien calculó el GPD para vdW-SAFT. El reducido número de ecuaciones con las que se ha trabajado, se debe principalmente al intenso trabajo computacional requerido para la descripción de transiciones de fase de alto orden y cuya dificultad escala fuertemente con el número de componentes. Los aspectos antes mencionados, se vuelven notablemente complejos de desarrollar con las EOS actuales, las que en busca de una mejor representación de los fenómenos físicos observados, aumentan su complejidad estructural, siendo necesario el desarrollo de estrategias computacionales y metódicas de cálculo muy particulares y por tanto poco transferibles a otras ecuaciones de estado.

El paso inicial fue desarrollar una metodología que permitiese abordar de manera clara y expedita el problema de la caracterización topológica, de manera independiente del modelo de EOS utilizado. Para ello se recogió la experiencia de trabajos anteriores desarrollados dentro del Grupo de *Termodinámica de Fases e Interfases* del Depto de Ingeniería Química [2] (Segura, 1999, 2001; Fernández, 2003; Bidart, 2007), además de una extensa revisión bibliográfica (Topliss, 1985; Flores, 2003).

Producto del gran número de modelos de EOSs disponibles en la actualidad, se escogió la EOS SAFT original (Chapman, 1990) para comenzar el estudio

[2] El Dr. Hugo Segura, docente de dicha casa de estudios superiores.

de esta tesis, debido a su gran versatilidad para representar fluidos complejos, y principalmente por su inspiración teórica, la que entregaba la oportunidad única de vincular un evento topológico del equilibrio de fases con un comportamiento molecular particular. Posteriormente, se utilizó PC-SAFT, por los argumentos indicados anteriormente.

2.1 GPD para la EOS SAFT. Moléculas de igual diámetro

En la Figura 2.1 se presenta el GPD de moléculas de igual diámetro (ξ=0) e igual número de segmentos, siendo m_1=m_2=1.

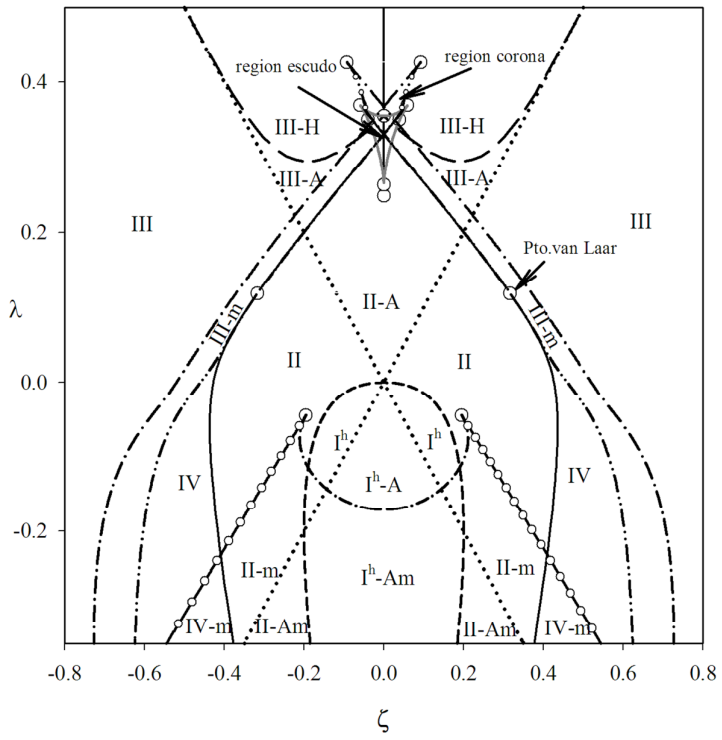

Figura 2.1 GPD para la EOS SAFT $\xi = 0$ y $m_1 = m_2 = 1$. (—): línea tricrítica. (–··–): doble punto crítico terminal (DCEP). (–·–): plato de presión crítico (CPSP). (···): punto azeotrópico crítico terminal (CAzeP). (- -): línea de presión y temperatura cero. (— —): transición azeotrópica-heteroazeotrópica. (—): límites de la región del escudo. (-○-) SCPEP. (○): puntos transicionales terminales restringidos por consideraciones de estabilidad.

Este diagrama es similar a los GPDs obtenidos con otros modelos de EOS tipo PEC-2 en similares condiciones (Konnyneburg, 1980; Boshkov, 1984; Boshkov, 1997; Kraska, 1999). Patrones característicos dentro de la topología de los GPDs tales como; la región del escudo (Griffits, 1978) y punto de van Laar se encuentran en los rangos de parámetros globales ζ, λ esperados.

Los sistemas *Tipo I* y *Tipo II* se distinguen entre sí por la aparición de una línea crítica independiente, representativa del equilibrio líquido-líquido. Esta línea tiene su génesis en la condición hipotética de temperatura cero. Para la EOS del tipo vdW existe la posibilidad de desarrollar el criterio matemático, no así para el caso de ecuaciones con origen teórico-molecular, como por ejemplo SAFT, que indefinen numéricamente en este límite. Esta indefinición numérica del modelo SAFT, le da una característica particular a la transición *Tipo I-Tipo II* haciendo necesario realizar un estudio topológico en busca del mecanismo acorde con tal condición. Se sigue la evolución de un sistema *Tipo II* a lo largo de la coordenada ζ. Las figuras 2.2 a-c muestran el mecanismo de transición. El criterio transicional, considerando la singularidad matemático-numérica del modelo SAFT en el límite de temperatura cero, se ha denominado ZPTL (***Z**ero **P**ressure **T**emperature **L**ine*):

$$\lim_{T\to 0} G_{2x} = 0 \tag{2.1}$$

$$\lim_{T\to 0} G_{3x} = 0 \tag{2.2}$$

$$P = 0 \tag{2.3}$$

Naturalmente siendo consistente con lo mencionado en párrafos anteriores, el cálculo numérico de la línea transicional ZTPL se realizó a la temperatura más baja que permitió la EOS, en este caso 1K.

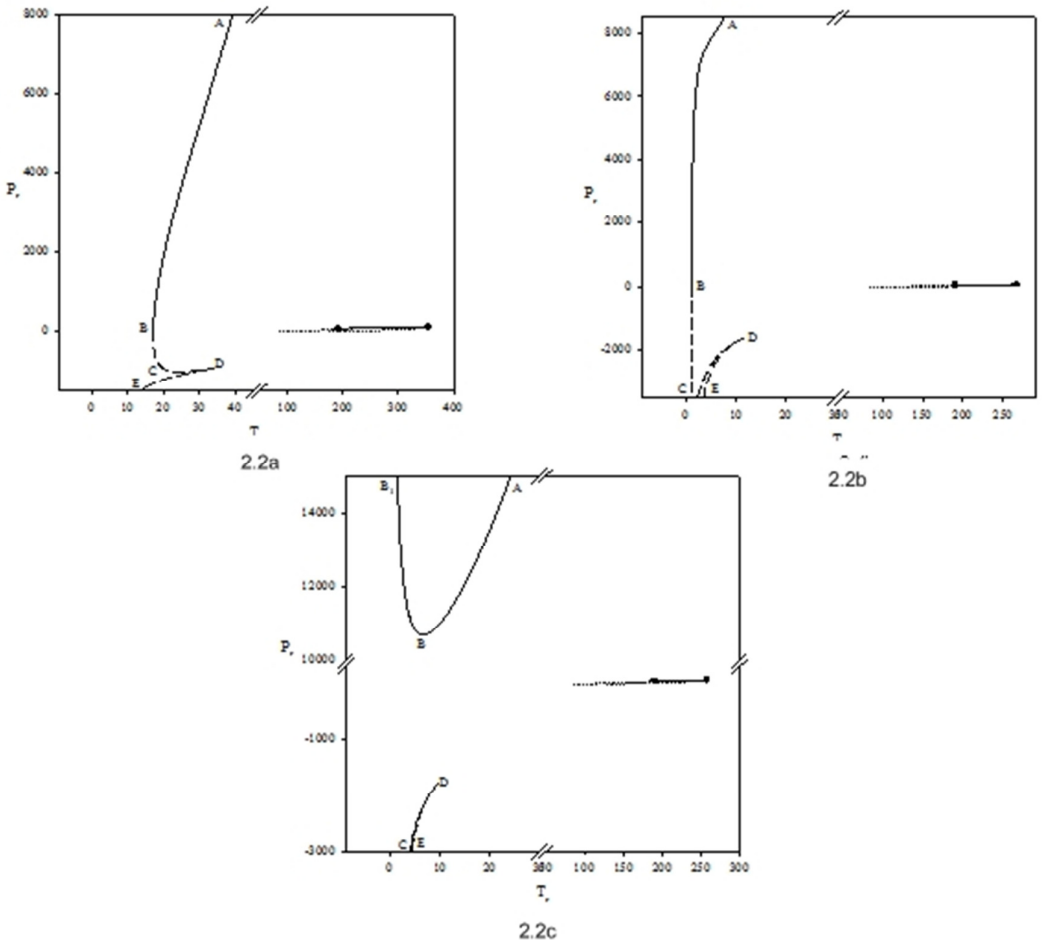

Figura 2.2. Transición Tipo I^h-II. (—): línea crítica. (···): presión de vapor. (- -): línea meta-inestable

El comportamiento inusual de baja temperatura del modelo SAFT, relacionado directamente con la construcción de la línea ZTPL, origina una serie de alteraciones en la topología del GPD y su capacidad para reproducir los Tipos observados experimentalmente, las que se detallan a continuación:

- el modelo SAFT no predice sistemas *Tipo I* sino un híbrido (*Tipo* I^h) que incorpora una región cerrada de inmiscibilidad a alta presión, en contraste con lo obtenido en la mayoría de las EOS cúbicas. Pese a su existencia, al menos por los estudios realizados, las condiciones extremas en las que se hace presente evitan su influencia en el desarrollo del resto de los mecanismos transicionales clásicos, a diferencia de los que sucede en fluidos Dieterici (Segura, 2004).

- la región que abarca la línea transicional ZTPL es bastante reducida y queda acotada por ambas tricríticas. Esto tiene una consecuencia muy importante y es que el modelo no predice, en éstas condiciones de $\xi = 0$, la existencia de sistemas *Tipo V*, ya que el mecanismo ZTPL también es responsable de la transición *Tipo IV-Tipo V*. Esto presenta una discrepancia respecto de un gran número de los modelos de EOS estudiados mediante el enfoque de GPD, los que predicen sistemas Tipo V para moléculas de igual diámetro.
- tanto el mecanismo CPSP como el DCEP se extienden de manera indefinida hacia valores de λ negativos sin alcanzar la línea ZTPL, al menos en rangos de parámetros de interacción con significado físico, a diferencia de lo que ocurre normalmente en las EOS cúbicas (Konynenburg, 1980; Boshkov, 1997).

2.1.1 Región de la Corona

La Figura 2.2 muestra el detalle de una nueva región asociada a la actividad CPSP en las cercanías de la región del escudo. Esta nueva organización de transiciones recibe el nombre de *región de la corona* y fue presentada por primera vez en el trabajo de Segura y Flores (2008), (CAPÍTULO IV). La génesis de esta nueva región está vinculada al límite de existencia de la transición CPSP. Análisis de estabilidad a lo largo del recorrido de la *línea CPSP* indican que esta *cruza la región del escudo*, *hacia valores mayores de λ* en la región del GPD donde aparecen los *sistemas Tipo III-H*.

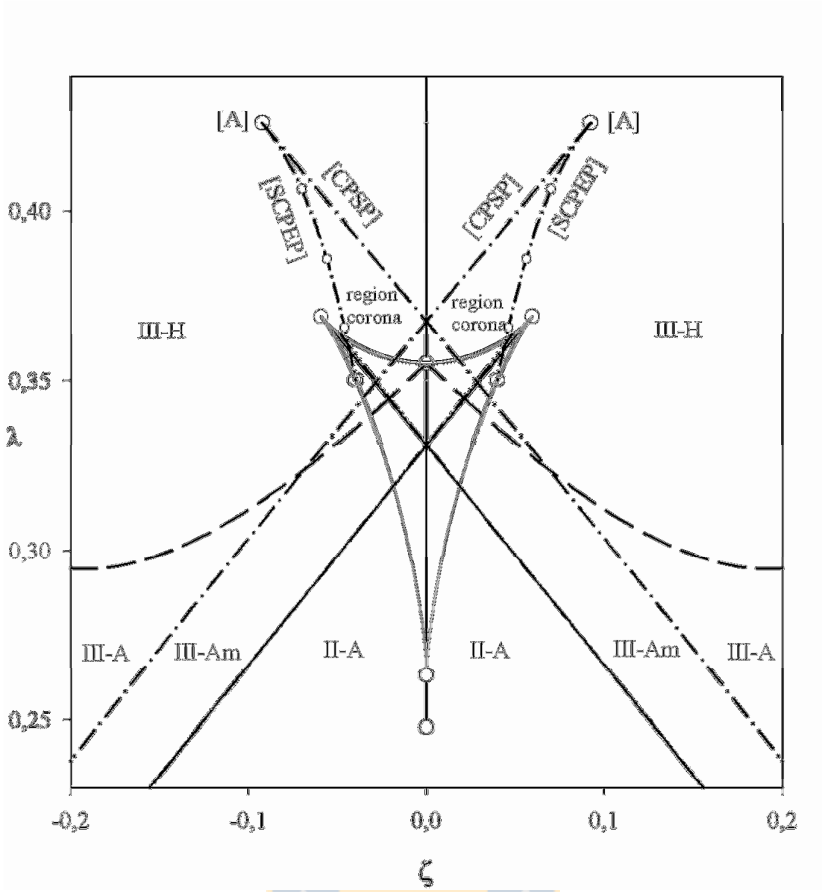

Figura 2.3. Región de la corona para la EOS SAFT $\xi = 0$ y $m_1 = m_2 = 1$. (—): línea tricrítica. (–··–): doble punto crítico terminal (DCEP). (–·–): plato de presión crítico (CPSP). (···): punto azeotrópico crítico terminal (CAzeP). (- -): línea de presión y temperatura cero. (— —): transición azeotrópica-heteroazeotrópica. (—): límites de la región del escudo. (-○-) SCPEP. (○): puntos transicionales terminales restringidos por consideraciones de estabilidad.

Finalmente se ha determinado que la actividad CPSP finaliza cuando una línea trifásica característica de los sistemas *Tipo III-H*, irrumpe sobre la línea crítica líquido-gas afectando su continuidad.

Los contornos laterales de la región de la corona establecen la condición límite para la existencia de múltiples puntos críticos estacionarios en presión (SCPEP). Las ecuaciones y un detalle de los mecanismos involucrados pueden observarse en CAPÍTULO IV.

La actividad CPSP también se manifiesta intensamente en la región inferior del GPD, en particular para valores de λ bajos, usualmente negativos generando también una serie de sistemas no reportados antes en la literatura donde sistemas que presentan una línea crítica ininterrumpida que conecta los puntos

críticos de los componentes puros (típicamente, *Tipo I* de acuerdo con la clasificación de van Konynenburg) presentan un punto de inflexión plana. Tanto en esta región como en la corona se desarrolla una intensa actividad en la curvatura de la línea crítica tal que, en algunos casos se observan sistemas con doble actividad CPSP. Los patrones descritos no son particulares del modelo aquí utilizado, así lo demuestra el trabajo Segura y Flores (CAPÍTULO IV)

2.2 GPD modelo SAFT. Moléculas de distinto diámetro

Se decidió trabajar con una mezcla binaria monómero+n-hexámero (recordar que debido a la naturaleza del modelo es necesario fijar algunos parámetros), la que es atractiva de analizar ya que, dentro de los sistemas que incluye se encuentra la mezcla metano+n-hexano. Desde un punto de vista práctico, este sistema tiene aplicación directa en la industria petroquímica y energética, ya que una corriente de gas natural puede ser caracterizada como un pseudo-binario basado en sus propiedades. Desde un punto de vista teórico constituye una prueba estricta de capacidad predictiva, pues ninguna EOS predice simultáneamente su tipo topológico y su equilibrio de fases en el rango subcrítico. La Figura 2.4 presenta el GPD para moléculas de distinto diámetro.

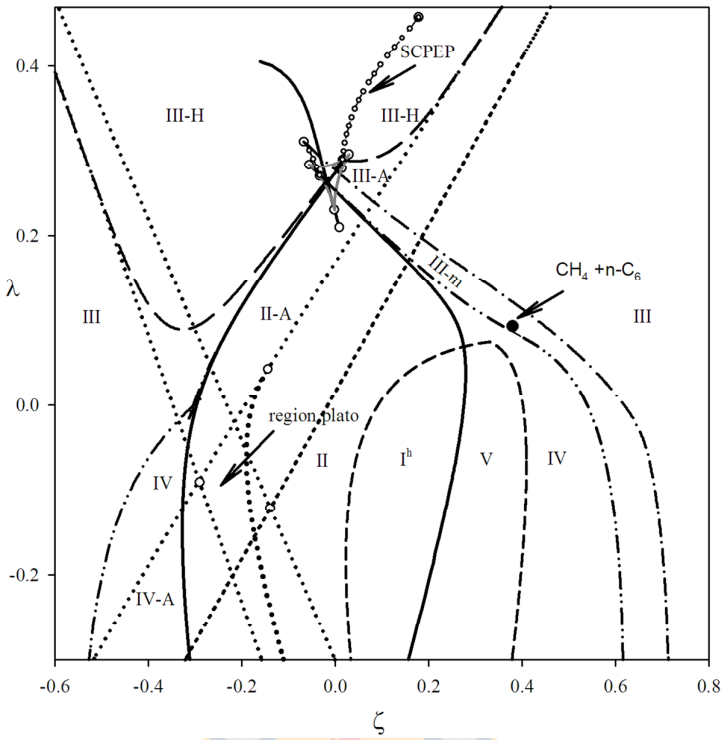

Figura 2.4 GPD moléculas de distinto tamaño y forma molecular para EOS SAFT $m_1 = 1; m_2 = 6$. (—): línea tricrítica. (–···–): doble punto crítico terminal (DCEP). (–·–): plato de presión crítico (CPSP). (···): punto azeotrópico crítico terminal (CAzeP). (- -): línea de presión y temperatura cero. (— —): transición azeotrópica-heteroazeotrópica. (—): límites de la región del escudo. (⊸) SCPEP. (○): puntos transicionales terminales restringidos por consideraciones de estabilidad. (•) Sistema CH_4+n-C_6

Como era de esperar una gran pérdida de la simetría del GPD ha ocurrido por efecto de la diferencia de tamaño molecular y aumento de la longitud de cadena molecular. En particular, la inspección de la Figura 2.4 revela que:

- la distorsión molecular produce varios efectos sobre los límites azeotrópicos. Primero el corrimiento de las líneas CAzeP hacia altos valores negativos de ζ generando una amplia región de sistemas *Tipo IV* con características azeotrópicas. Tiene lugar la aparición de la *región del plato*, que a diferencia de lo observado en otros modelos de EOS (Kolafa, 1999) se desarrolla en una extensa región dentro del GPD. Todos estos aspectos sumados a incursiones adicionales dentro de este GPD, indican que el modelo SAFT predice una rica topología azeotrópica que incluye dobles

azeótropos críticos y sistemas poliazeotrópicos, sólo por efectos de tamaño y forma molecular[3].

- la línea ZTPL presenta un desplazamiento a la derecha a tal punto que parte de ésta atraviesa la tricrítica, a diferencia de lo observado en la Figura 2.1. Esto permite al modelo SAFT predecir *Tipo V* en rangos de parámetros de interacción con significado físico. Por el lado izquierdo del GPD, respecto de $\zeta = 0$, el modelo no predice *Tipo V* ni *Tipo I*^{h}.
- en principio, la mezcla metano+n-hexano no califica con el *Tipo* topológico experimental (*Tipo V*) al usar parámetro de interacción nulo, sin embargo, al considerar valores negativos de dicho parámetro la predicción cualitativa es corregida hacia el Tipo correcto.
- no se observa actividad CPSP en la rama izquierda del GPD, al menos para $\lambda>0$. La región de la corona se destruye parcialmente, a diferencia de la región del escudo que mantiene su conectividad, en tal sentido se puede concluir que la actividad CPSP es más sensible a las diferencias de tamaño y forma molecular que la región predicha por Griffith (1978). Estudios de estabilidad en el SCPEP derecho, demuestran que es estable hasta fracción molar unitaria. El CPSP colapsa en un punto único de fracción molar unitaria por lo que no se predice sistemas *Tipo III-m*, en toda la región izquierda del GPD.

2.3 Efecto de la contribución de longitud de cadena en la topología global

Con la finalidad de analizar el impacto del término SAFT de cadena en la topología global del equilibrio de fases, se realizó una comparación a nivel de GPDs para dos EOS tipo PEC-2, donde el tratamiento de la forma molecular se realiza a través del factor acéntrico, el cual representa la desviación respecto de una forma molecular esférica, sin incluir de manera directa el impacto de la longitud de cadena. Los modelos escogidos son la EOS-vdW y EOS-RK[4], en similares condiciones que el GPD-SAFT de la Figura 2.4

[3] Detalles sobre la región del plato y otros fenómenos azeotrópicos para el modelo SAFT, pueden encontrarse en el trabajo de Flores, 2003

[4] Es necesario mencionar que éstos GPDs tampoco han sido determinados previamente, para la razón de diámetro estudiada.

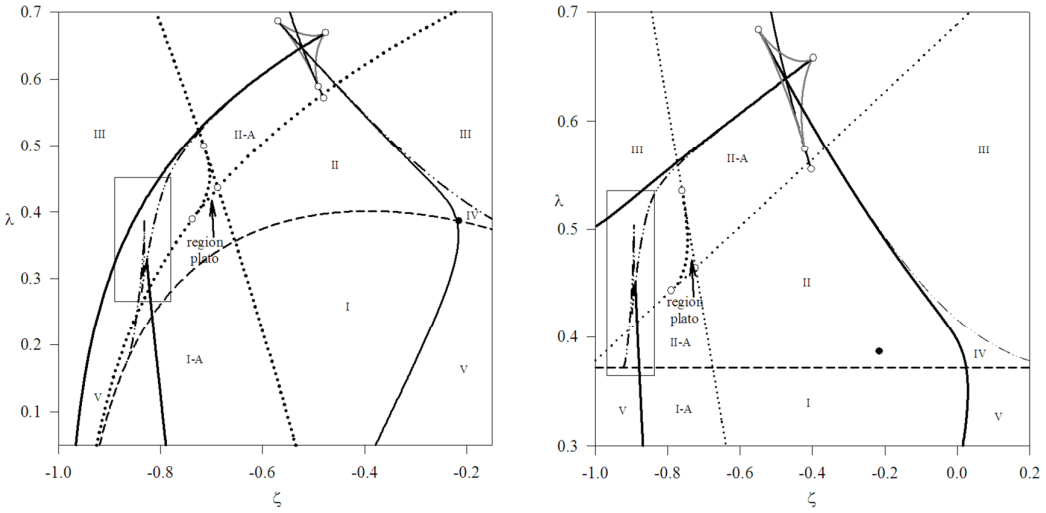

2.5a GPD vdW

2.5b GPD RK

Figura 2.5 GPDs de vdW y RK con igual razón de tamaño molecular que el GPD para modelo SAFT con $m_1 = 1; m_2 = 6$. (—): línea tricrítica. (–··–): doble punto crítico terminal (DCEP). (–·–): plato de presión crítico (CPSP). (···): punto azeotrópico crítico terminal (CAzeP). (- -): línea de presión y temperatura cero. (— —): transición azeotrpica-heteroazeotrópica. (—): límites de la región del escudo. (◦): puntos transicionales terminales restringidos por consideraciones de estabilidad. (•): mezcla metano+hexano con k_{ij}=0

Al revisar los GPDs de vdW (Figura 2.5a) y RK (Figura 2.5b), se observa que éstos predicen un rompimiento de la rama tricrítica izquierda, generando sistemas con patrones de inmiscibilidad compleja, que en general corresponden a variaciones del *Tipo IV*. Tal rompimiento de la línea tricrítica no se observa en el GPD de SAFT (Figura 2.4), por lo que es posible afirmar que *el término cadena estabiliza la transición tricrítica en un rango más amplio de parámetros globales*. Esta condición favorece la existencia de sistemas que no presentan inmiscibilidad en el rango de propiedades de los componentes puros, permitiendo que una línea crítica común, representativa del colapso de fases líquido-gas, los conecte. La idea expuesta es comprensible, pues de acuerdo con la teoría de Flory (Prausnitz, 1986), moléculas de cadena larga, en mezcla generan V^E negativos, originando también G^E negativos, indicando estados miscibles para el sistema.

2.4 Aplicación práctica de la teoría de GPD

Realizar un estudio de la topología global de fases con fines prácticos mediante el concepto de GPD, en modelos complejos que incorporan una gran cantidad de parámetros, es una tarea bastante difícil, incluso en modelos simples se transforma en un ejercicio tedioso. Normalmente es necesario fijar algunos de estos parámetros lo que limita considerablemente el estudio.

2.4.1 spd-GPD

La problemática expuesta ha motivado el desarrollo de un nuevo concepto de representación topológica que sienta sus bases en la teoría de GPD y que se ha denominado spd-GPD (***s**erial **p**redicted **d**omain-**G**lobal **P**hase **D**iagram*). Este nuevo mapa topológico permite analizar un conjunto específico de mezclas binarias formadas por un compuesto base y una serie homóloga, definiendo éstas, una trayectoria específica dentro de un GPD. Dicha trayectoria origina un plano de corte dentro de un GPD que establece los contornos particulares de un spd-GPD, tal como lo muestra la Figura 3.6, en coordenadas ζ, λ, ξ.

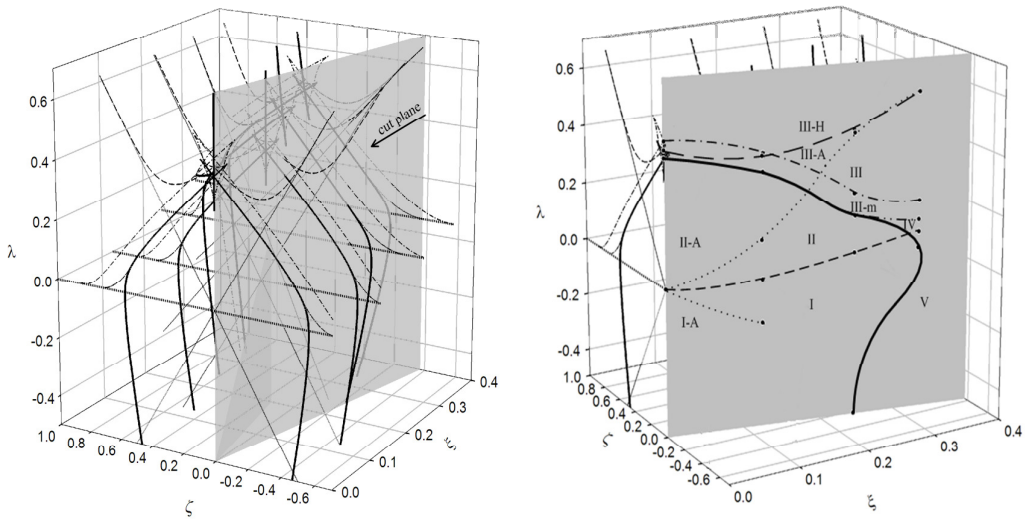

Figura 2.6. Representación esquemática del spd-GPD.

La forma de esta trayectoria está determinada por la relación entre las propiedades moleculares de la serie homóloga que se desea estudiar y que de acuerdo a las ecuaciones (1.8)-(1.10) definen las coordenadas dentro del GPD. Normalmente en un spd-GPD la variable manipulable será aquella que relaciona las propiedades moleculares de una serie homóloga. Así, por ejemplo en la serie de hidrocarburos, las propiedades críticas o moleculares sólo dependen del número de carbonos (Figura 2.7) o en su defecto la masa molecular (M_i), de tal manera que un conjunto de coordenadas lógicas de representación en un spd-GPD podría ser el número de carbonos y/o masa molecular, como variable independiente, y k_{ij} (en su defecto el parámetro λ) como variable dependiente.

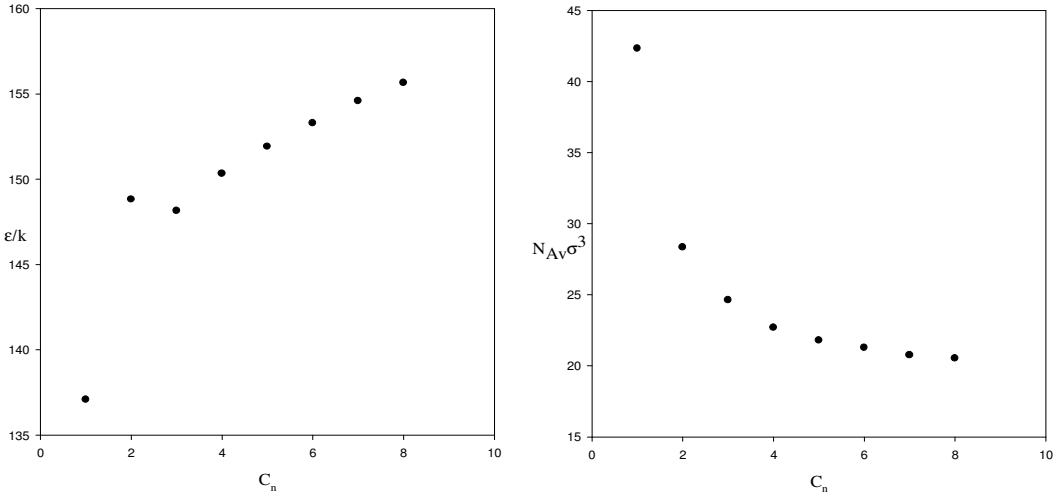

Figura 2.7a N°de carbonos y energía cohesiva **Figura 2.7b** N°de carbonos y diámetro

Figura 2.7 Relación entre propiedades moleculares y número de carbonos para la serie de hidrocarburos

Las ventajas asociadas son numerosas ya que reduce el cómputo de los mecanismos transicionales clásicos al no ser necesario construir un GPD para cada razón de diámetro representativa de cada elemento de la serie homóloga, basta entonces contar con un GPD de razón de diámetro tal, que permita inicializar los principios transicionales más relevantes y entonces seguir la progresión, a partir de éstos, para todos los elementos de la serie. En tal sentido es posible analizar efectos específicos en la topología global de fases

tales como la evolución de una mezcla a medida que aumenta la longitud de cadena de una serie (número de carbonos) y su impacto sobre regímenes de inmiscibilidad, barotropía o en el caso de una serie de alcoholes, donde existe asociación, el impacto coordinado de ésta y la longitud de cadena sobre topologías complejas de azeotropía. Finalmente, al igual que un GPD, se puede utilizar como una herramienta de coherencia termodinámica que permite discriminar de manera inequívoca si el modelo de EOS utilizado es aplicable a una mezcla específica o a una serie homóloga completa.

En función de los antecedentes provistos, en las secciones siguientes se aplica el enfoque spd-GPD para analizar dos casos representativos de uso frecuente en la industria petroquímica, las series CH_4+n-alcanos y CO_2+n-alcanos

2.4.2 spd-GPD CH_4+n-alcanos

Como caso inicial se consideró la caracterización de la serie homóloga de hidrocarburos lineales formando mezclas binarias con metano, a partir del modelo SAFT original (Chapman, 1990). En tal sentido, algunos estudios topológicos se han reportado en la literatura para este tipo de sistemas (Aparicio, 2007), pero solo de manera parcial llegado hasta una caracterización mediante proyecciones críticas, pero en ningún caso a partir del estudio directo de transiciones globales de fases. Por lo mismo, este tipo de sistemas no sólo sirve para ejemplificar la teoría de spd-GPD, sino que es un paso adelante en lo que se refiere a su caracterización con EOS de estado de origen molecular. Desde un punto de vista de implementación es relativamente fácil de trabajar pues basta partir del GPD de moléculas de igual diámetro molecular, representativo de una mezcla binaria hipotética de “metano+metano”.

La Figura 2.8 presenta el spd-GPD para las mezclas binarias de CH_4+n-alcanos hasta el n-octano, sistema hasta donde el modelo SAFT original muestra concordancia con los resultados de dinámica molecular (Chapman, 1988).

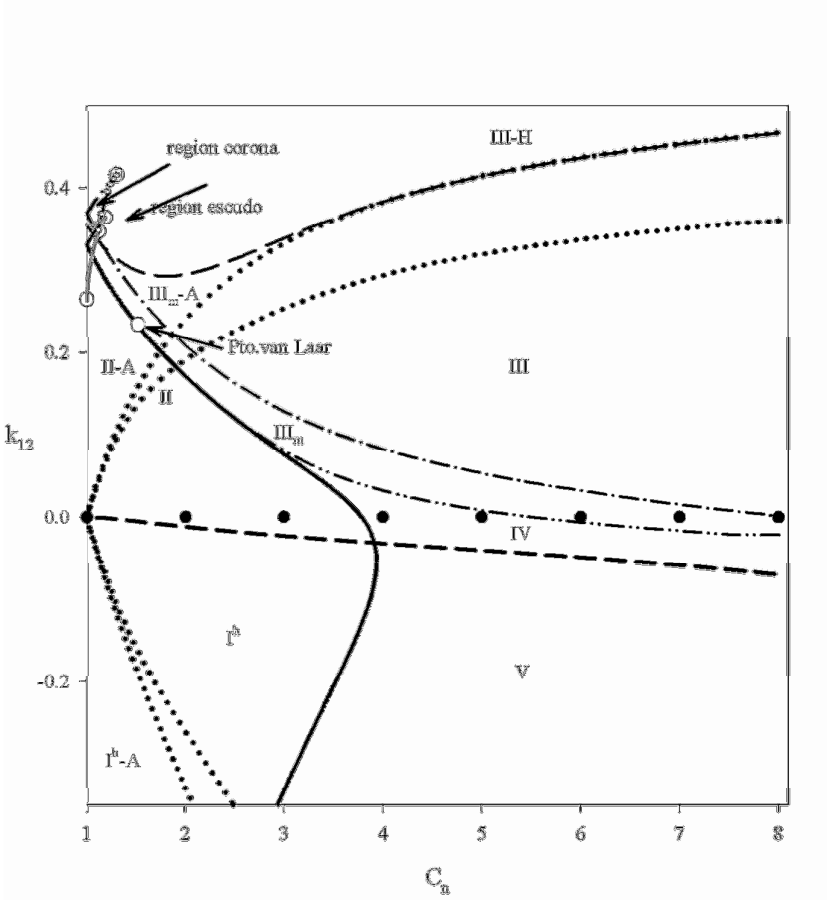

Figura 2.8 spd-GPD modelo SAFT para serie CH_4+n-alcanos. (—): línea tricrítica. (–··–): doble punto crítico terminal (DCEP). (–·–): plato de presión crítico (CPSP). (···): punto azeotrópico crítico terminal (CAzeP). (- -): línea de presión y temperatura cero. (— —): transición azeotrópica-heteroazeotrópica. (—): límites de la región del escudo.(◦) puntos transicionales terminales restringidos por consideraciones de estabilidad. (•): mezcla metano+n-alcano con k_{ij}=0

Un aspecto interesante deviene del análisis de la topología global de la serie con respecto al aumento de la cadena molecular. A medida que la longitud de cadena crece, se produce inicialmente la aparición de inmiscibilidad líquido-líquido de baja temperatura (*Tipo II*), posteriormente esta región de inmiscibilidad avanza hacia altas temperaturas rompiendo los regímenes de miscibilidad, en el rango de propiedades de componentes puros, originando sistemas *Tipo IV* y *Tipo III*. Como es de esperar, el aumento en el número de carbonos genera regiones más amplias de inmiscibilidad en el equilibrio de fases de las distintas mezclas de la serie.

Los puntos negros en la Figura 2.8 indican los Tipos topológicos para las distintas mezclas que el modelo de EOS representa desde un punto de vista

predictivo, considerando para ello el parámetro de interacción como nulo. Es sabido que la SAFT original no presenta un buen ajuste experimental de la información del equilibrio de fases, sin embargo, el interés en este caso es la predicción cualitativa del Tipo topológico, así podemos realizar las siguientes observaciones al respecto:

- la mezcla CH_4+n-etano es predicha como *Tipo I*^{h}, experimentalmente no se ha observado el loop parabólico de alta presión en esta mezcla; sin embargo, en virtud del alto valor en el que se predice su existencia, es posible afirmar que globalmente, *Tipo I*, el resultado obtenido es correcto.
- la predicción del sistema CH_4+n-propano clasifica en el *Tipo II*. En contraste, la experimentación establece que el sistema es *Tipo I*. Sin embargo, la predicción de la línea crítica líquido-líquido, característica del *Tipo II*, aparece en un rango de temperatura inferior al punto de congelación de la mezcla. Por tanto, la predicción globalmente estable del equilibrio fluido es correcta.
- CH_4+n-butano es predicho como *Tipo IV*. La topología experimental, en cambio, corresponde a *Tipo I*. De acuerdo con el trabajo de van der Kooi (1981), CH_4+n-butano es la primera mezcla de la serie de CH_4+hidrocarburos que presenta indicios de inmiscibilidad líquido-líquido en el extremo de metano concentrado. Si bien, esta condición no ha sido corroborada experimentalmente, es posible que la inmiscibilidad exista en un rango de condiciones inaccesible por las técnicas experimentales.
- la predicción del sistema CH_4+n-pentano corresponde a *Tipo IV*. La evidencia experimental establece que el sistema es *Tipo I*. De acuerdo con van der Kooi (1981), y al igual que para CH_4+n-butano, esta mezcla presenta indicios de inmiscibilidad, que probablemente no han sido detectados al momento de determinar experimentalmente su Tipología. De cualquier forma, está bien establecido que la curva de rocío presenta un doble lazo de condensación retrógada, característico de heteroazeótropo cuasi-crítico, en la vecindad de metano puro y post, sobre su temperatura y presión críticas (Rowlinson, 1982).

- CH_4+n-hexano es predicho como *Tipo III*, sin embargo experimentalmente corresponde a *Tipo V*. Como es de esperar el modelo SAFT no es capaz de describir el Tipo experimental sin la incorporación de un parámetro de interacción.
- la predicción de la mezcla CH_4+n-heptano se clasifica como sistema *Tipo III*, en buena concordancia con el comportamiento real.
- para la mezcla CH_4+n-octano, no fue posible ubicar información experimental con que comparar la predicción. Sin embargo, de acuerdo a Kohn y Brandish(1964), el Tipo experimental debería corresponder al predicho por el modelo SAFT, es decir, *Tipo III*.

En la mayoría de las mezclas, el modelo cumple con los Tipos experimentales; aunque en algunos casos como la mezcla CH_4+n-hexano predice *Tipo III*, la modificación del parámetro de interacción permite obtener el *Tipo V* experimental. Una consideración adicional que se desprende del spd-GPD en cuestión, es la imposibilidad, para los elementos de la serie, de presentar conductas azeotrópicas en el rango de parámetros de interacción con respaldo experimental.

2.4.3 spd-GPD CO_2+n-alcanos

Las mezclas binarias de CO_2 son de gran interés tanto desde el punto de vista industrial como del teórico. El CO_2 no tiene momento dipolar permanente, pero si grandes momentos cuadrupolares, que originan complejas interacciones con hidrocarburos, dificultando por tanto su predicción teórica. Presenta patrones complejos de equilibrio de fases como la aparición de azeotropía en mezclas de CO_2+etano y conductas barotrópicas a partir del sistema CO_2+n-tetradecano (Loos, 1989). En efecto, aparecen al menos cuatro de los seis Tipos topológicos de acuerdo con la clasificación de van Konynenburg (1980). En el área industrial este tipo de sistemas es de bastante interés, pues las mezclas de CO_2+hidrocarburos tienen importancia fundamental en la caracterización de pozos petrolíferos (Gardner, 1981), más aún, el CO_2 puede modificar la eficiencia en la recuperación producto de la conducta barotrópica que origina. La naturaleza inocua del CO_2 y sus excelentes características de refrigerante lo

hacen ideal para su uso en sistemas de enfriamiento en cascada en combinación con hidrocarburos de cadena larga como lubricantes (García, 2004). En el sector de energías limpias, las corrientes de biogás se caracterizan por mezclas con altos contenidos de hidrocarburos livianos y CO_2, en tal sentido, las posibilidades tecnológicas de aprovechamiento pasa en parte importante por el conocimiento del comportamiento del equilibrio de fases, a partir del cual se pueden diseñar rutas de separación. Bastantes esfuerzos se han realizado en busca de una caracterización tanto teórica como experimental, respecto de su comportamiento de equilibrio de fases. García et al. (2004) abordó el problema de caracterizar su comportamiento topológico de manera parcial a partir de la construcción de las proyecciones críticas respectivas utilizando el modelo PC-SAFT.

En esta sección el objetivo propuesto es caracterizar el comportamiento topológico para esta serie particular. Una vez identificados los distintos Tipos presentes a partir de la construcción del spd-GPD es posible analizar otros fenómenos topológicos de interés y su vinculación con el comportamiento de fases. A partir de los resultados obtenidos, en el Capítulo III se realizará un análisis de la conducta barotrópica, proponiéndose un mecanismo transicional que indicaría su límite de existencia dentro de un régimen trifásico.

Todos los cálculos que se presentarán a continuación fueron realizados utilizando el modelo de EOS PC-SAFT, la razones de la elección de esta EOS, fueron esgrimidas el Capítulo I. La misma terminología para los parámetros del modelo que en el trabajo de Gross y Sadowski (2001), es usada en este trabajo. Para sistemas no asociantes como los considerados en este trabajo, se requieren tres parámetros de componente puro: m_i (número de segmentos en una cadena del componente i), σ_i (diámetro de segmento) y ε_i (pozo potencial). Los parámetros moleculares para el CO_2 han sido tomados directamente de los datos recomendados por Gross y Sadowski (2001) según se presenta en la Tabla 2.1.

Tabla 2.1. Parámetros moleculares del CO_2 para el modelo PC-SAFT

	CO_2
ε / k (K)	169.21
σ (Á)	2.7852
M	2.0729

En el caso de la serie de hidrocarburos es posible correlacionar las propiedades moleculares del n-alcano con su masa molecular (M_i), pudiendo analizar el comportamiento de fases como función de este parámetro. Las correlaciones utilizadas corresponden a las presentadas por Gross y Sadowski (2001) y se indican a continuación.

$$\sigma_i = q_{01} + \frac{M_i - M_{CH_4}}{M_i} q_{11} + \frac{M_i - M_{CH_4}}{M_i} \frac{M_i - 2M_{CH_4}}{M_i} q_{21} \tag{2.4}$$

$$\left(m_i / M_i\right) = q_{02} + \frac{M_i - M_{CH_4}}{M_i} q_{12} + \frac{M_i - M_{CH_4}}{M_i} \frac{M_i - 2M_{CH_4}}{M_i} q_{22} \tag{2.5}$$

$$\left(\varepsilon_i / k\right) = q_{03} + \frac{M_i - M_{CH_4}}{M_i} q_{13} + \frac{M_i - M_{CH_4}}{M_i} \frac{M_i - 2M_{CH_4}}{M_i} q_{23} \tag{2.6}$$

En las ecuaciones (2.4)-(2.6), M_{CH4}=16.043 es la masa molecular del metano, finalmente, la Tabla 2.2 resume las constantes requeridas.

Tabla 2.2. Parámetros correlación propiedades moleculares de n-alcanos con M, en el modelo PC-SAFT.

J	unidades	0	1	2
q_{j1}	Á	3.7039	-0.3226	.6907
q_{j2}	mol/g	0.06233	-0.02236	-0.01563
q_{j3}	K	150.03	80.68	38.96

La extensión del modelo para mezclas es llevado a cabo a través de las reglas de mezclado de Berthelot-Lorentz para el cálculo de los parámetros cruzados (Aparicio, 2007)

$$\varepsilon_{ij} = \sqrt{\varepsilon_i \varepsilon_j}\left(1 - k_{ij}\right) \tag{2.7}$$

$$\sigma_{ij} = 0.5\left(\sigma_i + \sigma_j\right) \tag{2.8}$$

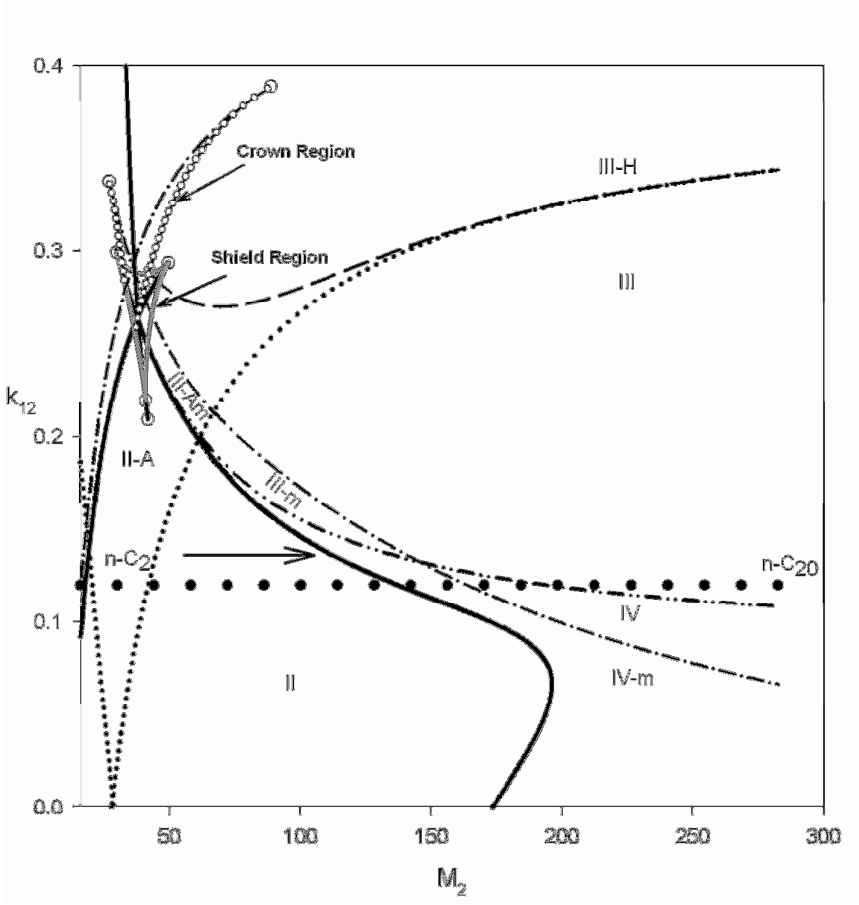

Figura 2.9. spd-GPD modelo PC-SAFT para mezcla CO_2+n-alcanos. (—): línea tricrítica. (–··–): doble punto crítico terminal (DCEP). (–·–): plato de presión crítico (CPSP). (···): punto azeotrópico crítico terminal (CAzeP). (- -): línea de presión y temperatura cero. (— —): transición azeotrópica-heteroazeotrópica. (—): límites de la región del escudo.(◦) puntos transicionales terminales restringidos por consideraciones de estabilidad. (•): Predicción del Tipo para la mezcla binaria CO_2+n-C*.

La Figura 2.9 presenta la predicción de los Tipos para mezclas de CO_2 con n-alcanos, desde C_1 hasta C_{20}, considerando un k_{12}=0.12 constante y representativo para toda la serie, según recomienda García (2004). Hasta el n-hexano experimentalmente las mezclas clasifican *Tipo I*, sin embargo, el modelo de EOS predice *Tipo II*. Un análisis de la región de inmiscibilidad señala que para estos sistemas, ésta tiene lugar en rangos de temperatura bajo el punto de congelación de la mezcla, por tanto desde un punto de vista

de estabilidad se pueden considerar *Tipo I*. Desde n-heptano hasta n-undecano experimentalmente se reporta *Tipo II*. En este punto hay discrepancias por tanto para el n-decano y n-undecano el modelo predice *Tipo IV*.
Desde el n-tridecano en adelante el modelo predice correctamente el comportamiento reportado experimentalmente, observándose principalmente sistemas que clasifican *Tipo III*.

CAPITULO III

3. COMPORTAMIENTO BAROTROPICO EN EL EQULIBRIO TRIFASICO

3.1 Barotropía*: Un gas que se hunde en un líquido*

La barotropía o inversión de densidad másica, corresponde a un fenómeno singular del equilibrio de fases que afecta directamente la posición relativa de fases coexistentes en mezclas heterogéneas cuando son expuestas a campos gravitacionales (ver Figura 3.1).

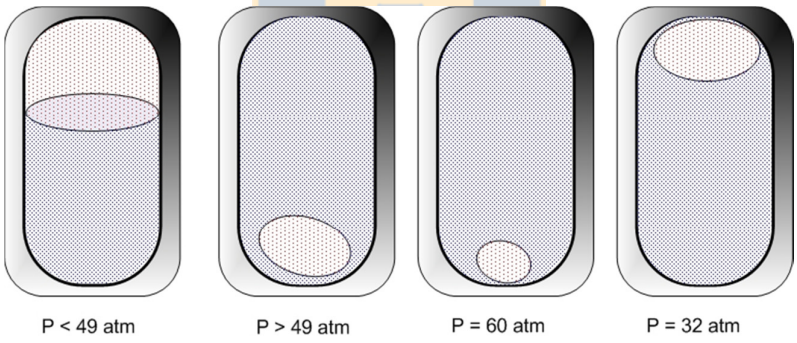

Figura 3.1. Esquema del experimento realizado por Kamerlingh Onnes en el que observó el fenómeno de inversión de densidades (Kamerlingh Onnes, 1906a)

3.2 Aproximación a la descripción de la barotropía.

El fenómeno de inversión de fases, puede tener importante injerencia en el diseño de un proceso productivo y operación del mismo, pues muchos sistemas de interés industrial ligados al sector petroquímico y manufacturero, presentan tal comportamiento, es así que se ha reportado su presencia en sistemas de uso intensivo tales como CO_2+hidrocarburos (Loos, 1989),

agua+hidrocarburos (Brunner,1990), alcoholes+hidrocarburos (Brunner, 1985) y refrigerantes+lubricantes (Hauk, 2000). La barotropía juega un rol fundamental en la recuperación de pozos petrolíferos mediante la inyección de CO_2 y necesariamente debe ser considerada en la planificación de las condiciones de operación del pozo así como de las herramientas de simulación que se utilicen. En el caso de mezclas de refrigerantes+lubricantes, su comportamiento debe ser muy bien determinado considerando para ello una selección apropiada de los químicos a utilizar y el diseño global de los sistemas de enfriamiento. Tal como lo puntualiza Quiñones-Cisneros (2005), una inversión de fases pudiera provocar que la mezcla más rica en el refrigerante, que por lo general tiene menor viscosidad que el lubricante, esté en contacto con las partes mecánicas del compresor, disminuyendo ostensiblemente la duración del equipo.

Quiñones-Cisneros (2004) enfrentó por primera vez la problemática de la inversión de fases bajo un contexto del comportamiento global de fases aplicado a sistemas binarios, considerando como caso de estudio la mezcla de CO_2+n-alcanos y el modelo PC-SAFT como herramienta predictiva. En particular, propuso el estudio de la transición entre sistemas *Tipo II* y *Tipo III*, para determinar su conexión con la barotropía. Siguiendo las ideas de Keesom y Kamerlingh Onnes (1906b, 1906c), desarrolló un análisis matemático a través del cual sugiere la existencia de un límite crítico isopínico (inversión de densidades molares) para la conducta barotrópica. En función de lo anterior, plantea las siguientes hipótesis:

- una transición inestable del tipo MDP (Punto Matemático Doble) es precursora de la presencia de barotropía molar en sistemas *Tipo III*, en función del cambio direccional que implica en la dependencia del volumen molar respecto de la fracción molar a lo largo de la línea crítica.
- establece como condición fundamental para que la barotropía másica se asocie a un Tipo topológico, este debe presentar una desconexión de la línea crítica que conecta los componentes puros.
- en sistemas asimétricos, para que el comportamiento barotrópico másico tenga lugar la inversión de densidades molares debe ocurrir

El artículo seminal de Quiñones-Cisneros, fue pionero en el enfoque utilizado. Trabajos posteriores que han estudiado la serie de CO_2+n-alcanos sólo se han limitado a realizar una reproducción parcial del análisis de Quiñones-Cisneros, sin entregar nuevos elementos y más bien con el objetivo de ejemplificar las capacidades del modelo utilizado para correlacionar información.

Un enfoque alternativo planteó Bidart (2007) en su estudio generalizado del sistema H_2O+n-alcanos, utilizando la EOS CSRK. En particular, evaluó el impacto sobre la condición barotrópica, presente en un equilibrio trifásico, de la longitud de cadena. El artículo sugiere que un posible límite de la conducta barotrópica puede estar asociado a su convergencia a un punto crítico terminal (CEP), guardando cierta semejanza con las ideas planteadas por Quiñones-Cisneros.

A partir de los antecedentes expuestos, se reconoce que la caracterización del fenómeno barotrópico no es un problema resuelto y en este sentido este trabajo pretende aportar nuevos antecedentes, profundizando para ello, en la relación entre la conducta barotrópica y el comportamiento de fases, a través un enfoque de Diagramas Globales de Fases. El estudio focaliza el análisis de series homólogas de mezclas binarias asimétricas, en ausencia de asociación. El uso de series homólogas, bajo el contexto de un GPD, permite analizar de manera continua la relación entre los distintos Tipos topológicos presentes y la barotropía, así como entender el impacto de una variable particular característica de la serie homóloga, como lo pudiera ser la longitud de cadena molecular.

3.3 Aproximación topológica a la barotropía en mezclas binarias asimétricas

Como caso de estudio se ha escogido la serie homóloga de CO_2+n-alcanos, la que ha sido bien caracterizada, tanto en la descripción teórica como experimental de su comportamiento crítico (García, 2004) y la presencia de barotropía (Loos, 1989), facilitando la comparación de resultados obtenidos y mecanismos transicionales propuestos.

Todos los cálculos que se presentarán a continuación fueron realizados utilizando el modelo de EOS PC-SAFT, en el contexto descrito en el Capítulo I. Las Figuras 3.2 a y b ilustra el comportamiento de fase para una mezcla binaria de CO_2+n-C$_*$, con M$_*$ =220, en el que se observa conducta barotrópica

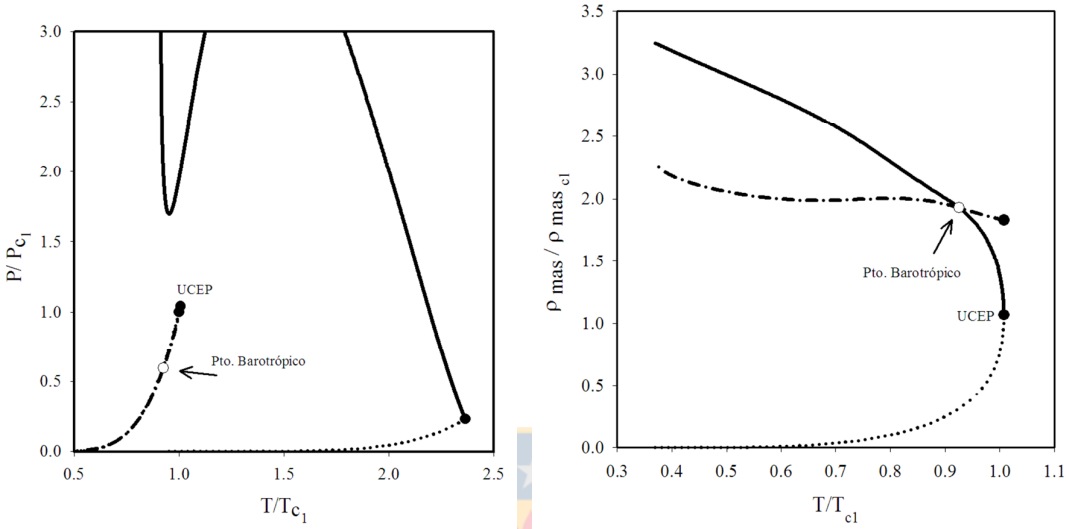

Figura 3.2a Proyección P-T para un el sistema CO_2 + n-C$_*$ con M$_*$=220 y k_{12}=0.12 de conducta barotrópica, (–·–): línea trifásica; (···): presión de vapor; (—): línea crítica,(◦):punto barotrópico (•): punto crítico

Figura 3.2b Proyección T-ρ_{mas} del equilibrio trifásico presente en el sistema CO_2 + n-C$_*$ con M$_*$=220 y k_{12}=0.12, (–·–): Líquido 1, L_1; (···): Vapor, V; (—): Líquido 2, L_2; (◦):punto barotrópico; (•): CEP

Figura 3.2 Comportamiento de equilibrio de fases para CO_2+n-C$_*$

La Figura 3.2a corresponde a un sistema *Tipo III*, de acuerdo a la clasificación de van Konyneburg & Scott. Esta proyección P-T muestra un punto barotrópico en la línea de tres fases. En 3.2b, se ilustra el cruce de densidades másicas entre dos fases tipo líquida (L_1 y L_2) y que se corresponde con la conducta barotrópica observada en 3.2a. Para este sistema la condición UCEP se obtiene entre una fase tipo líquido (L_2) y una fase vapor (V).

Siguiendo la metódica de Bidart (2007), se analiza el efecto de la masa molecular (M) sobre la evolución del punto barotrópico a lo largo de la línea trifásica (CAPÍTULO V).

La disminución de la masa molecular del segundo componente, equivalente a una reducción de la longitud de cadena del n-alcano, produce un desplazamiento relativo del barótropo dentro de la línea trifásica. Una convergencia hacia un punto CEP (punto crítico terminal), en particular un

LCEP (punto crítico terminal inferior), característico de sistemas *Tipo IV* y *Tipo V*.

El patrón de evolución tiene correspondencia con lo observado por Bidart (2007), sin embargo, la organización de las fases que invierten densidad es distinta. En el caso de la serie H_2O+n-C_nH_{2n+2}, la barotropía tiene lugar entre la fase anexa y la crítica, por tanto aun cuando se aproxime al límite CEP, la barotropía puede continuar a posteriori, ligada a un régimen de equilibrio bifásico. A diferencia del tipo de mezclas estudiado en este trabajo, la conducta asociante del agua altera notablemente la situación física por cuanto se tiene una fase condensada en la que el número de moléculas contenidas por unidad de volumen no sólo depende de la forma de la molécula sino también de interacciones de fuerza anisotrópicas. El equilibrio barotrópico del sistema bifásico se supone prolonga hasta alcanzar una línea crítica líquido-vapor o líquido-líquido. Independiente del caso, es claro que la condición límite para la barotropía presente en un sistema, es un punto *barotrópico crítico*, tal como en su momento apuntó Keesom (1906b) y recientemente Quiñones-Cisneros (2004). Aún así, esta suposición debe ser verificada.

El punto barotrópico crítico marca el fin de la inversión de fases en un sistema particular, pero por si sólo no establece un límite transicional dentro de un GPD. Si el límite barotrópico dentro una línea crítica tiene lugar post-CEP, será meta-inestable y el equilibrio barotrópico trifásico no se desarrollará.

Debido a que un punto barotrópico crítico es una solución singular de un punto crítico, una aproximación subcrítica puede ser propuesta como un mecanismo transicional según las siguientes ecuaciones:

$$\mu_1^{\alpha} = \mu_1^{\beta}, \mu_2^{\alpha} = \mu_2^{\beta}, P^{\alpha} = P^{\beta}, \mu_1^{\alpha} = \mu_1^{g}, \mu_2^{\alpha} = \mu_2^{g}, P^{\alpha} = P^{g} \tag{3.1}$$

$$v_{masico}^{\alpha} = v_{masico}^{\beta} \tag{3.2}$$

$$v_{molar}^{\alpha} - v_{molar}^{\beta} = \Delta \tag{3.3}$$

Las ecuaciones (3.1) a (3.3) representan un límite de existencia del comportamiento barotrópico para una mezcla binaria. Estas ecuaciones pueden ser resueltas simultáneamente fijando las propiedades críticas de los componentes puros, como una función de la sinergia de la mezcla (k_{12}).

3.3.1 Límite Barotrópico para una serie homóloga

La Figura 3.3 corresponde al mapa topológico para la serie de estudio en el formato spd-GPD. El diagrama presenta en coordenadas M-k_{12}, los mecanismos transicionales más relevantes, incluyendo el conjunto solución para la transición barotrópica propuesta desde las ecuaciones (3.1)-(3.3). Para una mezcla binaria de propiedades críticas de componente puro fijas y parámetro de interacción mayor que el límite transicional, se observa la existencia de barotropía vinculada a una línea heteroazeotrópica.

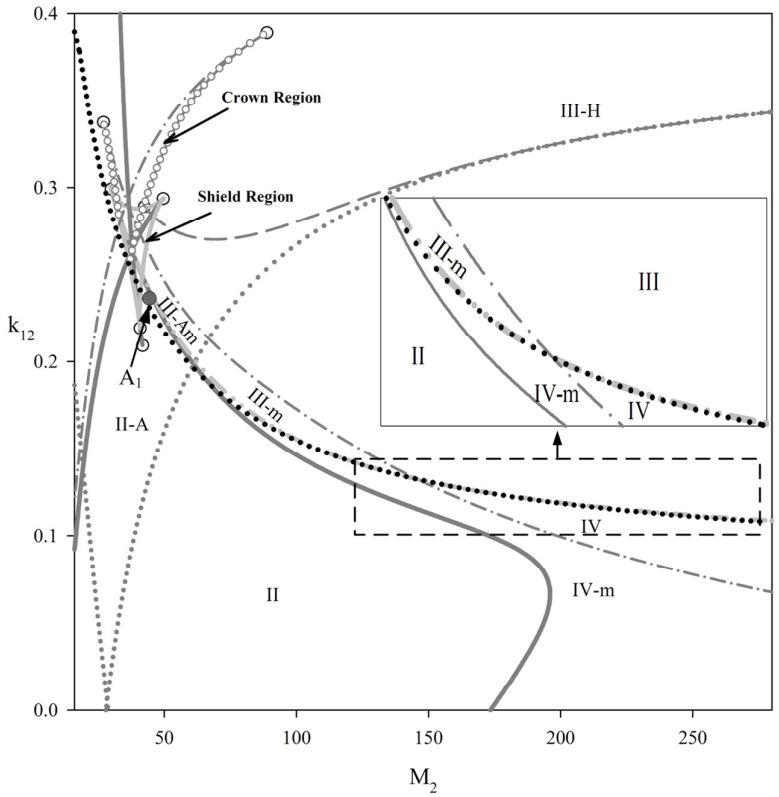

Figura 3.3 spd-GPD para la serie CO_2+n-alcano. (—): línea tricrítica. (—·—): doble punto crítico terminal (DCEP). (— · —): plato de presión crítico (CPSP). (···): punto azeotrópico crítico terminal (CAzeP). (—·—): transición azeotrópica-heteroazeotrópica. (◦) puntos transicionales terminales restringidos por consideraciones de estabilidad. (–○–) SCPEP. (···) CMaDIEP. Límite barotrópico propuesto.

El modelo PC-SAFT, predice barotropía principalmente en sistemas *Tipo III* y *Tipo IV*, acorde con lo observado experimentalmente para la familia de CO_2+n-alcanos (Loos, 1989).

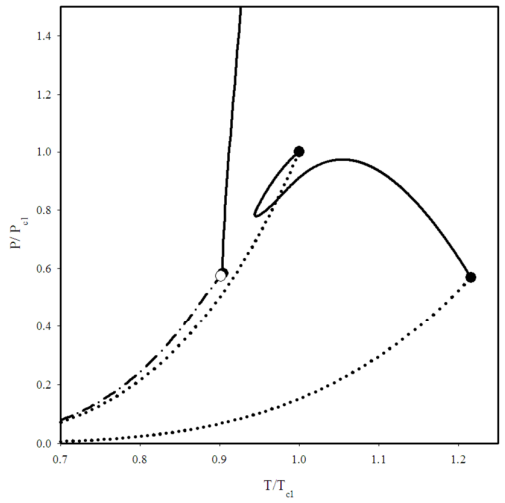

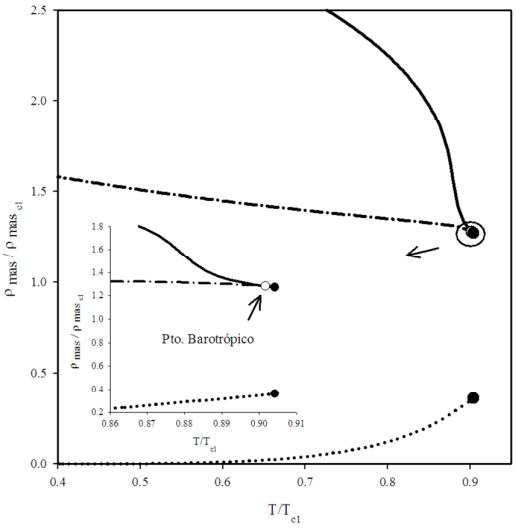

Figura 3.4a Proyección P-T de un sistema Tipo II con presencia de barotropía para la serie CO_2+n-alcano predicho por el modelo PC-SAFT. (–·–): línea trifásica; (···): presión de vapor; (—): línea crítica,(◦):punto barotrópico (•): punto crítico

Figura 3.4b Proyección T-ρ_{mas} del equilibrio trifásico, (–·–): Líquido 1, L_1; (···): Vapor, V; (—): Líquido 2, L_2; (◦):punto barotrópico; (•): CEP

Figura 3.4 Equilibrio de fases representativo de un sistema *Tipo II* con comportamiento barotrópico

Una primera inspección de la Figura 3.3, muestra que el límite barotrópico atraviesa la condición tricrítica y desarrolla una conducta similar al DCEP dentro del spd-GPD.

El sistema A_1 corresponde a *Tipo II* con presencia de barotropía (ver Figura 3.4a). La condición barotrópica tiene lugar muy próxima al UCEP. En 3.4b se puede ver el detalle del cruce de densidades másicas entre el Líquido 1 (L_1) y el Líquido 2 (L_2). Aun cuando no existe evidencia experimental del sistema antes descrito, la evidencia teórica refuta la propuesta de Quiñones-Cisneros, por cuanto la barotropía puede tener lugar en sistemas que presentan una línea crítica continua que conecta a los componentes puros.

El traspaso tricrítico no tiene influencia en la presencia de barotropía (CAPÍTULO V), pero si el DCEP, como se muestra en las figuras siguientes:

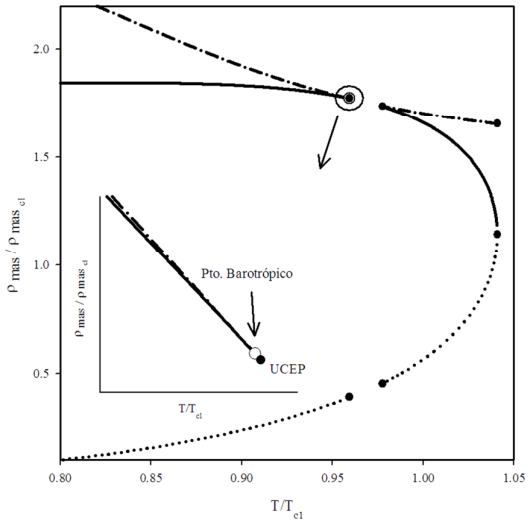

Figura 3.5a Proyección T-ρ_{mas} del equilibrio trifásico para el sistema A_4, (–·–): Líquido 1, L_1; (···): Vapor, V; (—): Líquido 2, L_2; (◦):punto barotrópico; (•): CEP

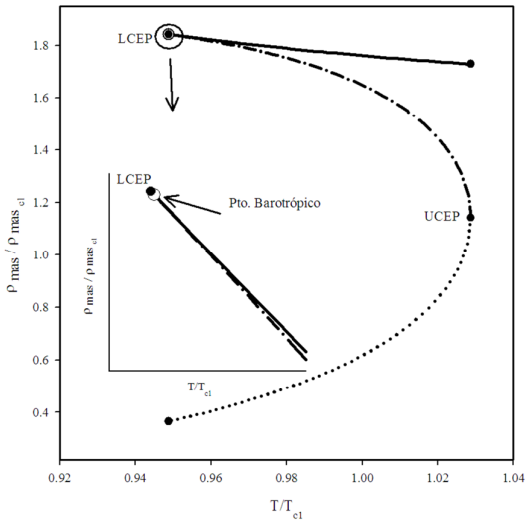

Figura 3.5b Proyección T-ρ_{mas} del equilibrio trifásico para el sistema A_5, (–·–): Líquido 1, L_1; (···): Vapor, V; (—): Líquido 2, L_2; (◦):punto barotrópico; (•): CEP

Figura 3.5 Equilibrio de fases en la vecindad del cruce CMaDIEP y DCEP

La Figura 3.5a corresponde a un sistema *Tipo III* con barotropía en la única región trifásica que tiene (de baja temperatura), la Figura 3.5b es un *Tipo IV* con presencia barotrópica en una región trifásica de alta temperatura (para ver más detalles, revisar CAPÍTULO V), esta variación tiene lugar cuando el nuevo límite transicional, CMaDIEP, cruza la línea DCEP, en dicho cruce la barotropía cambia de ubicación desde una trifásica de alta temperatura a una baja temperatura.

3.3.2 Discusión desde un perspectiva experimental de la serie CO_2+n-C_nH_{2n+2}

A partir del mecanismo transicional propuesto para el límite de la conducta barotrópica, así como el análisis realizado respecto de su vinculación a los distintos Tipos topológicos de la serie CO_2+n-alcanos, resulta conveniente someter el mecanismo planteado a un test adicional y para ello se procede a contrastar con los resultados experimentales disponibles.

Como se mencionó en el Capítulo II, la serie CO_2+n-alcanos ha sido bien caracterizada, tanto desde el punto de vista de su comportamiento crítico (García, 2004), como de la existencia de conducta barotrópica (Loos, 1989).

En particular, se ha reportado que el último sistema de la serie que no presenta barotropía es la mezcla CO_2+n-C_{13}, el que se corresponde a un *Tipo IV* (Enick, 1985) de acuerdo con la clasificación de van Konynenburg & Scott (1980). A partir de n-C_{14}, las mezclas con CO_2 clasifican *Tipo III* (García, 2004), observándose conjuntamente la presencia de barotropía (Loos, 1989).
Las predicciones del modelo PC-SAFT, tanto del Tipo topológico como de la existencia de barotropía para un k_{12} constante y representativo de la serie son consistentes con lo indicado en la literatura, en el CAPITULO V se reporta esto con más detalle.

3.3.3 Análisis Perfluoroalcanos+n-C_nH_{2n+2}

Como se indicó en la sección 3.2, la barotropía puede tener fuerte injerencia en sistemas de refrigeración, en particular asociado a cambios de viscosidad que finalmente se traducen en una reducción de la vida útil de los equipos involucrados, tales como intercambiadores de calor o compresores (Quiñones-Cisneros, 2005). Las mezclas de perfluoro-n-alcanos+$C_{2n}H_{2n+2}$ han recibido especial atención por cuanto, poseen buenas cualidades como refrigerantes y son ambientalmente más amigables con la capa de ozono en comparación con los CFCs. Aún así, su caracterización experimental y teórica respecto del fenómeno barotrópico es limitada (Aparicio, 2008).
A partir de lo anterior, esta sección focaliza el estudio de la serie perfluoro-n-alcanos + $C_{2n}H_{2n+2}$ considerando no sólo hidrocarburos lineales de diferentes longitudes de cadena sino también incluyendo una variación en la estructura del componente base, es decir, el perfluoro-n-alcano. Para ejemplificar lo anterior se ha considerado; CF_4, C_2F_6.
Siguiendo la metodología desarrollada en el CAPÍTULO V para la serie de CO_2+$C_{2n}H_{2n+2}$, se analiza el efecto de la masa molecular (M_i) sobre la evolución del punto barotrópico a lo largo de la línea trifásica, para los casos base CF_4+$C_{2n}H_{2n+2}$ y C_2F_6 +$C_{2n}H_{2n+2}$

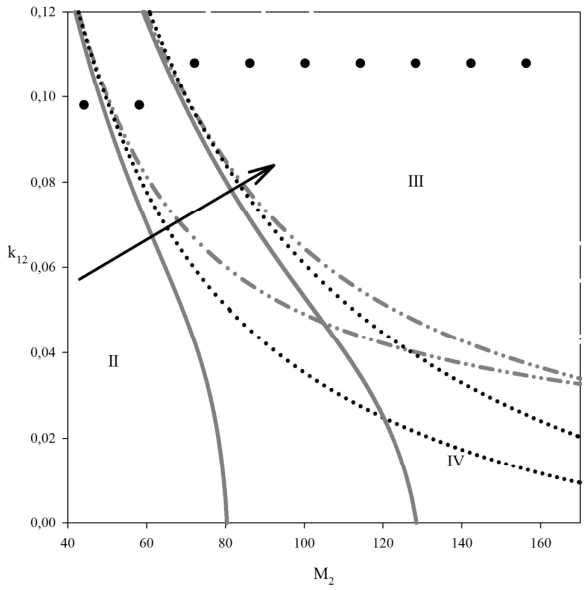

Figura 3.6 spd-GPD para las series CF4 + $C_{2n}H_{2n+2}$ y C_2F_6 +$C_{2n}H_{2n+2}$ (—): línea tricrítica. (—·—): doble punto crítico terminal (DCEP). (···) Límite barotrópico propuesto.

La Figura 3.6, corresponde al spd-GPD para la serie perfluoro-n-alcano. Sólo los marcos referenciales globales, más relevantes para el límite barotrópico son incluidos aquí, en particular las transiciones tricrítica y DCEP. La flecha indica el sentido en el que aumenta el número de carbonos del primer componente (perfluoro-n-alcano). Luego se desprende que:

- como en el caso base analizado en la sección 3.3, para un componente fijo de la mezcla binaria (perfluro-n-alcano), el aumento del número de carbonos del segundo componente incide en una mayor aparición de la conducta barotrópica por cuanto aumenta la asimetría molecular de la mezcla.
- el aumento del número de carbonos del perfluoro-n-alcano, también puede ejercer influencia por cuanto disminuye la asimetría de la mezcla, requiriéndose una longitud de cadena mayor del segundo componente para observar el fenómeno de inversión. Aún cuando el fenómeno es correcto hay otros aspectos que deben considerarse para perfluro-n-alcanos superiores, tales como el aumento del número de átomos de flúor, grupo voluminoso y altamente electronegativo, que reemplaza al hidrógeno en la cadena alquílica.

- se observa una fuerte presencia de sistemas *Tipo IV* de conducta barotrópica a diferencia de lo observado en CO_2+$C_{2n}H_{2n+2}$. Por otro lado, no se observa *Tipo II* con inversión de densidades.
- los resultados predicho por PC-SAFT en cuanto al Tipo topológico y la presencia de barotropía se corresponden con la información experimental disponible

CAPÍTULO IV

4. Condiciones límites para el comportamiento de plato de presión en el Diagrama Global de Fases de mezclas binarias compuestas por moléculas esféricas de igual tamaño

Artículo publicado en The Journal of Supercritical Fluids, 48 (2009) 108-119

El plato de presión (CPSP) tiene directa relación con fenómenos retrógados, pues se vincula con el comportamiento de las líneas críticas que parten de los componentes puros. El mecanismo CPSP implica una inflexión estacionaria en la presión crítica de la mezcla, que puede ser observada en la proyección PT. Por esta razón no es posible detectar el CPSP mediante análisis de estabilidad de fases. La práctica común es utilizar mecanismos límites del comportamiento de fases o singularidades de ciertas propiedades termodinámicas como la entalpía.

Desde un punto de vista del GPD su estudio se ha limitado a definir la transición *Tipo III-m a Tipo III*. En este artículo se presenta un exhaustivo análisis del comportamiento del CPSP, encontrándose su presencia en sistemas que usualmente presentan una línea continua y estable que conecta los puntos críticos de los componentes puros, a diferencia de lo que se observa convencionalmente en el GPD.

Este artículo corresponde a una extensión de lo mostrado en el Capítulo II, obteniéndose dos nuevas regiones paramétricas dentro del GPD, llamadas *región de la corona* y *región de la copa*. La región de la corona se relaciona con actividad CPSP en sistemas *Tipo II* a la altura de la *región del escudo.* En cuanto a la *región de la copa,* ésta establece límites para la presencia de CPSP en sistemas *Tipo I.*

A continuación se incorpora el artículo para más detalles.

J. of Supercritical Fluids 48 (2009) 108–119

Contents lists available at ScienceDirect

The Journal of Supercritical Fluids

journal homepage: www.elsevier.com/locate/supflu

Limiting conditions for the critical pressure step point behavior in the Global Phase Diagram of binary mixtures composed by spherical molecules of equal sizes

Mauricio Flores[a], Hugo Segura[a,*], María José Tardón[a], Jaime Wisniak[b], Ilya Polishuk[c]

[a] Departamento de Ingeniería Química, Universidad de Concepción, POB 160-C, Concepción, Chile
[b] Department of Chemical Engineering, Ben-Gurion University of the Negev, Beer-Sheva 84105, Israel
[c] The Department of Chemical Engineering & Biotechnology, Ariel University Centre, 40700 Ariel, Israel

ARTICLE INFO

Article history:
Received 18 May 2008
Received in revised form 20 August 2008
Accepted 5 October 2008

Keywords:
Critical points
Critical lines
Equations of state
Global Phase Diagram
Fluid phase equilibrium
Retrograde phenomena

ABSTRACT

Although many complex phase diagrams have been clearly systematized by means of the Global Phase Diagram (GPD) approach, no previous analysis has been devoted to establishing the limiting conditions of the critical pressure step point (CPSP) behavior for the case of binary mixtures. The CPSP mechanism implies a stationary inflection in the critical pressure of a mixture which can be observed along the *PT* projection of the gas–liquid critical line, although in ranges where (usually) a single critical phase exists. Due to this latter reason the CPSP cannot be detected using a phase stability analysis approach, which is the common tool used to delimiting mechanisms of phase behavior, but by clear geometric singularities of other key properties of fluid mixtures, such as the enthalpy. The scope of this work is to characterize the influence of the CPSP mechanism on the topology of phase diagrams over the whole range where the quoted mechanism exists and persists, in order to elucidate some gaps that still exist regarding the global phase behavior of binary mixtures. Accordingly, two new parametric regions of the GPD are described in this contribution, namely the *goblet* and the *crown* regions, where the effect of the CPSP on the fluid phase behavior can be clearly observed in systems that exhibit negative deviation from ideal behavior (mainly Type I and V systems) and in mixtures that are in the vicinity of the shield region.

1. Introduction

The Global Phase Diagram (GPD) approach is a powerful thermodynamic tool that was introduced in the seminal work of van Konynenburg and Scott [1,2] with the purpose of systematizing the different classes of phase diagrams predicted by the van der Waals (vdW) equation of state (EOS). Briefly, the GPD is a parametric plot whose coordinates directly depend on the parameters and constants of the EOS model used in its construction. Essentially devoted to fluid–fluid phase transitions, GPDs map entire regions inside of which mixtures, as predicted by the EOS model, exhibit common features of fluid phase behavior [3] (namely: presence or absence of azeotropy, presence or absence of partial miscibility, continuity and intersections of critical lines, etc.) thus yielding a comprehensive classification of phase diagrams in terms of Types [4]. The regions where Types can be predicted are bounded by the so-called transitional mechanisms which, in turn, establish the limiting range of parameters in which the specific phase equilibrium attributes that characterize a Type incipiently appear. At its present status of development, the theoretical basis of the GPD approach – *particularly, the mathematical description of the transitional mechanisms involved in its calculation* – have been generalized further, and the approach has been extended both to empirical and molecular based EOSs. Nowadays, GPDs allow even relating singular phase equilibrium characteristics to physically sound parameters in molecular simulation [5,6] and have been initially applied to the analysis of interfacial behavior [7,8] or to the description of phase equilibrium phenomena characterized by mixtures of three components [9]. However, despite of the fact that many complex patterns of fluid phase behavior have been described in-depth so far, minor attention has been given to the prediction of the critical pressure step point (CPSP) transitional mechanism. Similarly to any other transitional behavior, CPSP states can be experimentally detected in real systems and they can be modeled by equations of state using certain values of the GPD parameters. However, while some models could describe the CPSP mechanism at realistic values of these parameters, others could do it at too high or too low values. Thus, location and shape of the CPSP loci on the GPD present essential

* Corresponding author. Tel.: +56 41 2203662; fax: +56 41 2247491.
E mail address: hsegura@diq.udec.cl (H. Segura).

0896-8446/$ – see front matter © 2008 Elsevier B.V. All rights reserved.
doi:10.1016/j.supflu.2008.10.004

Nomenclature

a	cohesion term
A	Helmholtz energy
b	covolume
G	Gibbs energy
H	enthalpy
n	number of moles
P	pressure
R	universal gas constant
T	temperature
v	volume
x	mole fraction
Z	compressibility factor

Superscripts

a	non-critical or additional phase
c	critical phase
ig	ideal gas
L	liquid
R	residual property
V	vapor

Subscripts

c	critical property
M_{nP}	nth order partial derivative of the property M with respect to pressure
M_{nT}	nth order partial derivative of the property M with respect to temperature
M_{nv}	nth order partial derivative of the property M with respect to volume
r	reduced property

Greek symbols

	GPD parametric coordinate related to differences between pure components
	GPD parametric coordinate related to sinergy
	GPD parametric coordinate related to molecular size ratio
$\Omega_{a,b}$	EOS parameter

Abbreviations

AzEP	critical azeotropic end point
CEP	critical end point
CLI	closed loop of immiscibility
CPSP	critical pressure step point
EOS	equation of state
GPD	Global Phase Diagram
HMDP	hypercritcal mathematical double point
LCPSP	limiting critical pressure step point
LLG	liquid–liquid–gas
LSCPP	limiting stationary critical pressure point
RK	Redlich–Kwong
SCPEP	stationary critical pressure end point
vdW	van der Waals
VLE	vapor–liquid equilibrium

information regarding the suitability of any particular EOS model for the real fluid phase equilibria calculations and development of the pertinent GPD methodology is of significant practical importance.

Fig. 1 depicts the ordinary effect of the CPSP mechanism on the *P–T* projection of a binary mixture (the arrow indicates the direction in which the attraction forces between non-equal molecules become weaker). Calculations were performed with the traditional van der Waals (vdW) equation of state (EOS), considering a mixture with the physical properties indicated in Table 1. Fig. 1 shows that, initially, the critical line that emerges from the heavier component {2} exhibits multiple pressure stationary points of opposite concavities (points A and B in Fig. 1a), which afterwards collapse into a flat point of inflection (CPSP in Fig. 1b). After the CPSP transition, the critical line exhibits monotonous behavior in pressure as shown in Fig. 1c. The CPSP is the transitional mechanism that typically delimits *Type III-m* and *III* behaviors, and this is the ordinary attribute with which it has been recognized in the GPDs that have been calculated so far. It has been also demonstrated that the CPSP transition is related to particularly complex phase behavior that current EOS models are capable to predict. For example, and as Boshkov and Yelash [10] demonstrated and Polishuk et al. [11] confirmed later on for the case of the Redlich–Kwong (RK) equation, the CPSP is a key transitional mechanism that gives place to closed loops of immiscibility (CLI) in the vicinity of the transition from Type *III* to Type *V*. A similar mechanism for predicting *CLIs* has been discovered by Yelash and Kraska [12] and also discussed by Bidart et al. [13] in EOS models that combine the Carnahan–Starling [14] hard sphere repulsion reference with vdW-type attraction terms.

Table 1
Critical properties and interaction parameter for the system in Fig. 1.

A. Critical properties	
T_{c2}/T_{c1}	P_{c2}/P_{c1}
3.00134	3.00134
B. Interaction parameters	
Case	k_{12}
Fig. 1a	0.0299
Fig. 1b	0.0659
Fig. 1c	0.0992

The literature review indicates that although the phase behavior of binary mixtures has been systematized by means of the GPD [3,4] approach, none of the published works have unequivocally established the limiting conditions of the CPSP boundary on the GPD map. This work has been undertaken to characterize the influence of the CPSP on the topology of systems that exhibit negative deviation from ideal behavior (mainly Type *I* and *V* systems) and for systems that are in the vicinity of the so-called shield or Griffiths' Region [15] (where quadruple points of fluid phases can be predicted by EOS models), in order to characterize the phase behavior of fluid mixtures over the whole range where the CPSP activity exists.

2. Theory

2.1. Phase equilibrium topology for mixtures in the vicinity of a CPSP

Although specific details concerning the impact of the CPSP mechanism on fluid mixtures are well-known, its influence and/or possible occurrence on phase diagrams of real mixtures has not yet been described in depth. For this reason, we begin this section introducing some less known geometric features, which are useful for analyzing experimental evidence or theoretical results of mixtures whose phase equilibrium conditions are close to a CPSP. The slope of the critical line of a binary mixture along the *PT* projection

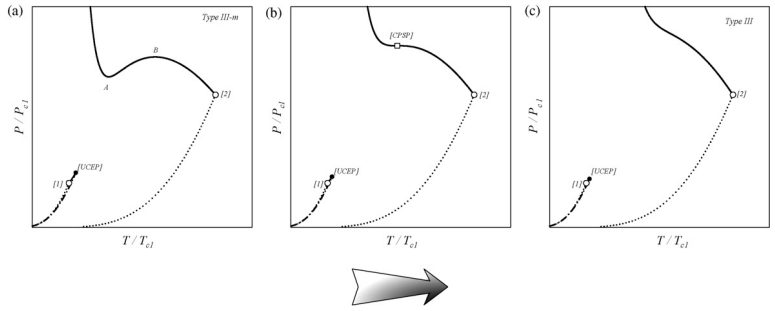

Fig. 1. (a–c) Critical *P–T* projections in the vicinity of a CPSP. (. . .) Pure component vapor pressure line, (▬) critical line, (–~–) three phase line, (○) pure component critical point, (●) critical end points (CEPs).

is given by following relationship [16,17]

$$\left(\frac{\partial P}{\partial T}\right)_c = \frac{1}{T}\frac{H_{2x}}{V_{2x}} = -\frac{G_{2xT}}{G_{2xP}} \tag{1}$$

where P and T is the equilibrium pressure, and temperature, and x, H, V, and G are the mole fraction, molar enthalpy, molar volume, and molar Gibbs energy of the mixture respectively. In the development that follows the notation $M_{nx,mT,kP}$ will indicate the operator $\partial M^{(n+m+k)}/(\partial x^n \partial T^m \partial P^k)$. According to Eq. (1), every pressure stationary point along the *PT* critical projection implies a local inflection of the enthalpy function of a mixture ($H_{2x}=0$) at the same $\{x, T, P\}$ coordinates where the stationary point occurs. The results shown in Fig. 2a clearly confirm the inflection of the enthalpy function for the stationary points observed in Fig. 1a (points A and B, respectively) and for the CPSP observed in Fig. 1b.

An additional consequence of a stationary critical pressure point follows from the analysis of the limiting curvature of the binodal envelope, given by [18]

$$\left(\frac{\partial^2 T}{\partial x_1^2}\right)_c = T\frac{G_{4x}}{H_{2x}} \tag{2}$$

In general, ordinary binodals collapse into a smooth stationary point at the critical temperature of immiscibility (usually known as *consolute temperature*). However, inspection of Eqs. (1) and (2) reveals that the curvature of the binodal at the stationary critical pressure point becomes undefined at the *Tx* projection of a binary mixture. This is so because $H_{2x}=0$ (as required for a stationary critical pressure point), while the diffusional stability constraints satisfy $G_{2x}=G_{3x}=0$ and $G_{4x}>0$ at an ordinary critical point [19]. Consequently, the critical temperature taken from the corresponding stationary critical pressure point implies a *singular critical point* in the *Tx* binodal, as illustrated in Fig. 2b. Singular binodals, like the case in the present example, may be found in *every stationary critical pressure point* along the *PT* projection and, certainly, for the particular case of the stationary inflection of the CPSP.

Retrograde phenomena, which were first experimentally described by Kuenen [20], may be unequivocally analyzed in terms

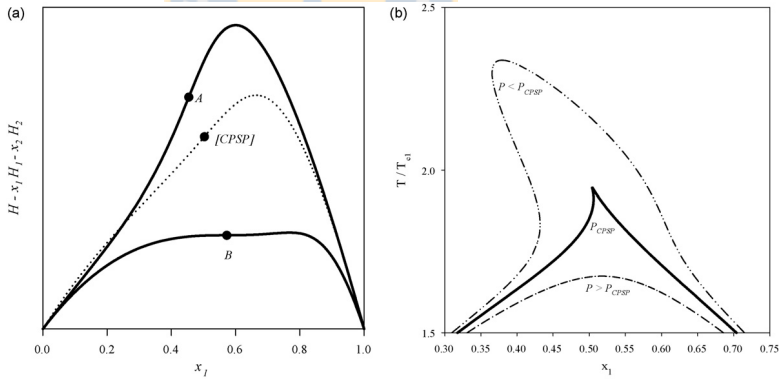

Fig. 2. (a) Mixing enthalpy plot. (▬) Mixture in Fig. 1a at different thermomechanical conditions, (. . .) mixture in Fig. 1b. (●) Stationary critical pressure. (b) *x–T* phase diagram for the mixture shown in Fig. 1b with the mixture properties reported in Table 1. Isobaric binodals taken at (–●–) $P/P_{c1}=4.3000$, (▬) $P/P_{c1}=4.1137$ {*CPSP* isobar}, (–●●–) $P/P_{c1}=4.0000$.

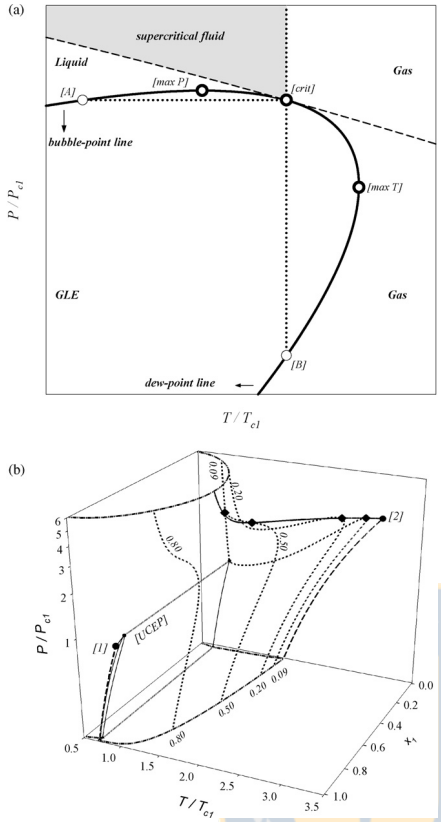

Fig. 3. (a) Schematic isopleth at the *PT* projection. (▬) Isopleth, (– – –) critical line, [*max P*] condenbar point, [*max T*] condenterm point, [*crit*]: critical point. (b) *x*–*T*–*P* VLE diagram for a system at the CPSP. (▬) Critical line, (. . .) isopleths, (– – –) pure component vapor pressure line, (●) pure component critical point, (♦) mixture's critical points.

of the shape and geometry of an *isopleth* (phase equilibrium envelope of constant mole fraction) along the *PT* projection [21–23]. Fig. 3a illustrates how a typical isopleth meets the critical point [*crit*] and also shows the range of temperature and pressure conditions where specific phases appear. In this figure, the branches [*A*]–[*crit*] and [*B*]–[*crit*] correspond to the bubble-point and dew-point lines, respectively. Generally, along an isopleth, retrograde behavior is characterized by the relative position of the critical point with respect to the position of the stationary points in temperature (cricondentherm point, *max T*) and pressure (cricondenbar point, *max P*). A mixture exhibits retrograde condensation (i.e. the gas phase liquefies as pressure decreases) if the dew-line exhibits temperature maxima. In the case shown in Fig. 3a, retrograde condensation can be observed for every isothermal expansion process with final pressure inside the region [*crit*]–[*max T*]–[*B*]. Similarly, a mixture exhibits retrograde evaporation or cavitation (i.e. the liquid phase vaporizes with decreasing temperature), when the bubble-line exhibits a pressure maximum. Retrograde boiling is shown in Fig. 3a for any isobaric cooling process having its final temperature inside the region [*A*]–[*max P*]–[*crit*]. In the PT projection (Fig. 3a) an isopleth becomes tangent to the critical line as it approaches the critical point [24]. Consequently, a limiting local condition for retrograde boiling is for the pressure to become stationary along the critical line. In a similar way, a stationary point in critical temperature constitutes a limiting condition for retrograde condensation. In the case of the CPSP, where a degenerated stationary critical pressure is observed, the critical point of the isopleth coincides with the cricondenbar point.

Fig. 3b depicts the different shapes of isopleths that may be found for a binary mixture at the CPSP transition for a Type *III* system (in this case we consider the phase diagrams predicted for the system shown in Fig. 1b). Fig. 3b shows that depending on the concentration, isopleths (for example $x_1 = 0.09$ and $x_1 = 0.20$) may exhibit single gas–liquid critical points, multiple critical points ($x_1 = 0.50$) or no critical points at all ($x_1 = 0.80$). The latter behavior is found in a binary mixture where none-to-many critical points interact with stationary points along isopleths, indicating that systems in the vicinity of a CPSP present multiple patterns of retrograde activity. Wisniak et al. [24] have established that in a two-phase system there is a clear relation between the geometry of an isopleth and the trend of the solubility. From their analysis it follows that every stationary point along an isopleth implies also a stationary point for the solubility. Particularly interesting is the fact that a negative slope of the bubble branch of an isopleth implies *increasing solubility of the volatile component in the liquid phase as the temperature increases*. As shown in Fig. 3b, isopleths with negative pressure slope for the liquid phase appear frequently in mixtures whose thermomechanic conditions are in the vicinity of the CPSP transition.

Summarizing, the CPSP transition exhibits many equilibrium features in fluid phase behavior that include singular critical points for phase diagrams, anomalous solubility patterns, dominant retrograde activity, and inflecting behavior for mixing functions (particularly enthalpy). In addition, Wisniak et al. [25] have pointed out that Type *III* behavior is of particular interest since mixtures belonging to this classification are potential candidates for application of supercritical extraction technology. In general, Type *III* mixtures are characterized by a large difference of the critical properties of the constituents, as occurs with mixtures of light gases dissolved in heavy liquids. The CPSP implies that the mixing enthalpy of the mixture inflects at the critical point, yielding thus a rich variety of solubility patterns in quasi-critical conditions. Therefore, to establish whether a mixture is in the vicinity of a CPSP transition (or, conversely, to establish if the mixture is Type *III*-m or *III*) it is important to predict the behavior of the solubility in sub-critical and/or quasi-critical conditions.

2.2. Global phase diagram calculations. A systematic approach based on van der Waals binary mixtures

The purpose of this section is to characterize the complete range of activity for the CPSP transition and, additionally, to establish its limiting conditions in terms of the molecular nature of the mixture. For the purpose of illustrating typical phase diagrams of binary mixtures, we will consider the detailed GPD predicted by the original vdW-EOS model

$$P = \frac{RT}{V - b} - \frac{a}{V^2} \tag{3}$$

which, as shown by van Konynenburg and Scott [1,2], embodies almost every type of phase behavior, except those exhibiting closed loops of immiscibility. In Eq. (3) *a* and *b* are the cohesion parameter and the covolume, respectively, which can be calculated from pure component parameters according to the following quadratic mixing rules

$$a = \sum_{i,j} x_i x_j a_{ij}; \qquad b = \sum_{i,j} x_i x_j b_{ij} \tag{4}$$

where

$$a_i = \frac{27}{64}\frac{(RT_{ci})^2}{P_{ci}}; \qquad b_i = \frac{1}{8}\frac{RT_{ci}}{P_{ci}} \tag{5}$$

in addition, the cross terms required for mixing rules in Eq. (4) are given by

$$a_{ij} = \sqrt{a_i a_j}(1 - k_{ij}); \qquad b_{ij} = \frac{b_i + b_j}{2} \tag{6}$$

In Eq. (6), k_{ij} is a parameter that accounts for interactions between molecules of different type ($k_{ij} = 0$ if $i = j$). The mathematical conditions for the CPSP transition have been well established in previous works [26] and are applicable to every EOS model. In terms of the Gibbs energy of binary mixtures, and following the bifurcation analysis suggested by Boshkov [26], it satisfies the following set of equations

$$G_{2x} = G_{3x} = G_{2xT} = 0 \tag{7.a}$$

$$G_{4x}G_{2x2T} - G_{3xT}^2 = 0 \tag{7.b}$$

Eq. (7.a) imply the condition of a critical point with stationary pressure along the *PT* projection (see Eq. (1)). Eq. (7.b), in turn, implies a singular solution of Eq. (7.a), where two critical points of stationary pressure and opposite concavities collapse in a single flat inflection. It is important to establish that Eq. (7.b) alone *does not imply an inflection point of pressure* along the *PT* projection and that it should be necessarily be solved together with Eq. (7.a), in order to obtain a physically meaningful geometry in a phase diagram. In general, the conditions indicated by Eqs. (7.a) and (7.b) yield cumbersome analytical relations, even for very simple EOS models like vdW EOS. Consequently, the CPSP transition has been computed according to the following methods

- by performing direct calculations of critical *PT* projections and then bounding the range of the mixture parameters where stationary inflections are observed (see, for example, the approach considered by van Konynenburg and Scott).
- by minimizing the numerical approximation of the derivatives in Eqs. (7.a) and (7.b) in terms of the parameters of the mixture.

Anyone of these alternatives may hide some of the solutions because of the number of critical projections that are required for a precise mapping of the CPSP, or due to numerical errors involved in performing numerical differentiation. According to our experience, the CPSP calculation is an extremely ill-conditioned numerical problem in certain ranges of the mixture properties. Therefore, although cumbersome, the best numerical alternative for obtaining solutions over the whole range where CPSP transitions may occur is to consider analytical relations for Eqs. (7.a) and (7.b), whenever possible. For this latter purpose, the derivatives required in Eqs. (7.a) and (7.b) may be conveniently expressed in terms of the Helmholtz energy function (*A*) using Legendre transformations [27] (the pertinent relationships, *applicable to every EOS model*, may be found in Appendix A).

The theoretical basis of a GPD and its basic calculation details have already been described in the literature [28,29]. Briefly, a GPD

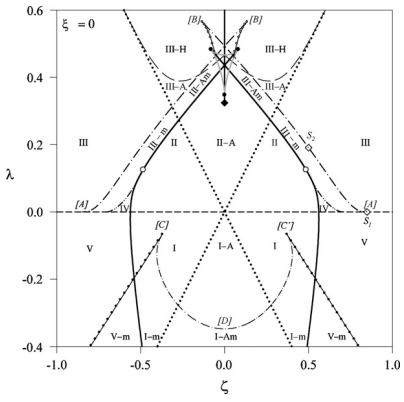

Fig. 4. Global Phase Diagram for vdW mixtures with molecules of equal size ($\zeta = 0$). (▬) Tricritical line, (– – –) zero temperature line, (. . .) line of critical azeotropy, (–·–) CPSP line, (–··–) DCEP line, (——) III–A–H transition line, (▭) shield region boundary, (–◌–) stationary critical pressure end point (SCPEP), (–●–) limiting stationary critical pressure point (LSCPP), (◌) van Laar points, (●) tricritical end points for the shield region, (⧫) low pressure tricritical endpoint.

is a parametric plot whose coordinates depend on the parameters of the EOS model used in its construction. It maps entire regions inside of which mixtures, as predicted by the EOS model, exhibit qualitative similarity in phase behavior (for example, presence or absence of azeotropy, presence or absence of partial miscibility, etc.). For the purpose of this work the coordinates of the GPD are given by the following definitions

$$\zeta = \frac{b_2 - b_1}{b_2 + b_1}$$

$$\xi = \frac{a_2/b_2^2 - a_1/b_1^2}{a_2/b_2^2 + a_1/b_1^2} \tag{8}$$

$$\lambda = \frac{a_2/b_2^2 - 2a_{12}/(b_1 b_2) + a_1/b_1^2}{a_2/b_2^2 + a_1/b_1^2}$$

where ζ accounts for size differences of the molecules of a mixture, ξ establishes the relation between the critical properties of the components and λ is a measure of the synergy between non-equal molecules. Consequently, a specific mixture corresponds to a single point of the GPD map, from which the equilibrium topology (or Type) is completely deduced. Each line of the GPD implies a transitional mechanism by means of which the characteristics of a specific Type may be obtained. In this work, we constraint our discussions to the lines related to the CPSP transition.

Fig. 4 depicts the GPD of the vdW-EOS for binary mixtures composed by molecules of equal sizes ($b_1 = b_2$) showing the range of global parameters $\{\xi, \zeta, \lambda = 0\}$ where the main Types of behavior can be predicted, including the pertinent boundary (or transitional) lines. As indicated by van Konynenburg and Scott [2], and as shown in Fig. 4, the GPD of molecules of equal sizes ($\zeta = 0$) is a symmetric plot about the $\xi = 0$ coordinate. This latter condition implies that the phase diagram of a mixture with global parameters taken from the right hand side of the GPD is equivalent to the behavior shown by a mixture located on the left hand side (after exchanging the labeling of components).

Consider now the CPSP line shown in Fig. 4. It is seen that CPSP activity appears in two sections of the GPD and has the following characteristics:

- an upper branch stems from positive ζ values above the shield region (point A) and meets the zero temperature line at point B for ζ = 0. Global stability analysis [30,31] reveals that for ζ > ζB, the behavior of CPSP is metastable. No previous work has established the upper limit for the CPSP transition, which was believed to end inside the shield region. However, as shown by Fig. 4, this is not the case: the CPSP boundary line *crosses the shield region and then it evolves to higher ζ values*, in the parametric domain of the GPD map where Type *III–H* systems appear. In addition, Fig. 4 shows that the upper branch of the CPSP mainly appears in a range of global parameters outside the area delimited by tricritical lines (a topologic region where, to a great extent, Type *II* systems appear). Consequently, the mechanism of the upper branch of the CPSP mainly affects mixtures for which the continuity of the gas–liquid critical is interrupted by the immiscibility of the liquid phase (as usually occurs in Type *III* systems).
- an additional branch of the CPSP activity (line C–D–C′) appears in the range of low (negative) ζ values where, usually, negative deviations from ideal behavior may be observed. However, in contrast to the upper branch, the lower branch is *completely contained inside the range delimited by tricritical lines*. Consequently, this latter CPSP activity mainly affects systems for which an uninterrupted gas–liquid critical line joins the critical points of pure components (typically, Type *I* systems in the classification of van Konynenburg and Scott). For molecules of equal sizes, the lower branch starts at points C and C′ where the CPSP appears at the critical point of a pure component and ends in point D in a critical azeotropic end point. To the best of our knowledge, no previous work has established the existence of this lower CPSP branch, which accounts for the possibility of multiple pressure stationary points along the critical line of miscible systems.

In the following section, we discuss specific characteristics and the phase diagrams related to the upper and lower branches of the CPSP.

3. Results and discussions

3.1. Details of the upper branch of the CPSP: the crown region

Fig. 5 shows details of the CPSP transition in the vicinity of the shield region, where the *stationary critical pressure end point* (SCPEP) boundary has been included as a limiting condition for the case of multiple stationary pressures. The effect of a SCPEP on a *P–T* projection is schematically shown in Fig. 6: as a result of the quoted mechanism, a three-phase line (*a.k.a.* heteroazeotropic or LLG line) meets the critical end point (CEP) in a pressure minimum. In addition to this latter pressure stationary point, the stable branch of the critical line exhibits a pressure maximum and an inflection point, thus retaining the characteristics of a degenerate pressure stationary point. The basic relations defining the SCPEP mechanism are

$$G_{2x}(T, V^c, x^c) = G_{3x}(T, V^c, x^c) = G_{2xT}(T, V^c, x^c) = 0 \quad (9.a)$$

$$\zeta_i(T, V^c, x^c) = \zeta_i(T, V^a, x^a) \quad (9.b)$$

$$A_V(T, V^c, x^c) = A_V(T, V^a, x^a) \quad (9.c)$$

where Eq. (9.a) establish a stationary critical pressure condition while Eqs. (9.b–9.c) imply a phase equilibrium condition of the critical phase "*c*" with and a non-critical phase "*a*" (in order to fix ideas, it is useful to recall that $P = -A_V$)

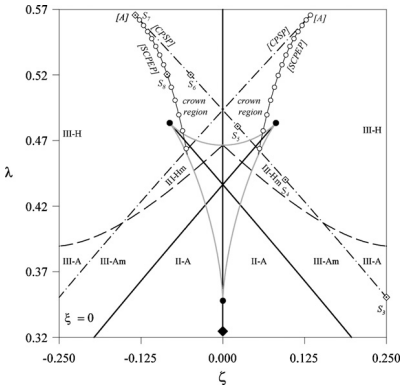

Fig. 5. Details of Fig. 4 in the vicinity of the shield region. Captions as in Fig. 4.

Below the vertex of the cone generated by the intersection of the CPSP and SCPEP lines (point A in Fig. 5) a new region of the GPD is developed and which we call the "*crown region*". Inside the boundaries of this new region, the *PT* projections belong to a subclass of Type *III–H* behavior and are characterized by one or even two stable branches of critical lines exhibiting two critical points of stationary pressure and opposite concavities.

Fig. 7 depict the different critical *PT* projections that may be drawn from the upper branch of the CPSP of the vdW-EOS. In particular, Fig. 7a illustrates a mixture with the parameters shown in point S_i in Fig. 4, which corresponds to the lowest limiting ζ value of the upper branch of the CPSP. According to Fig. 7a, the CPSP appears at zero temperature condition, in a finite pressure value,

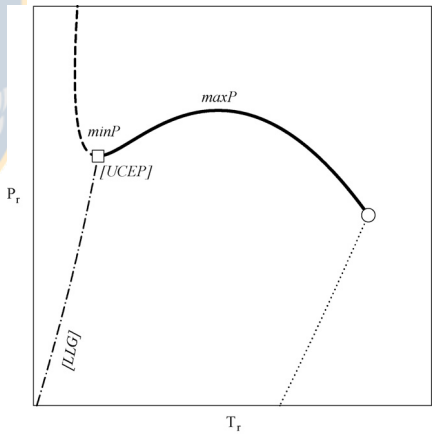

Fig. 6. Schematic *P–T* projection at the SCPEP transitional mechanism. (▬) Stable critical line, (– – –) metaestable critical line, (. . .) pure component vapor pressure line, (–·–) three phase line, (○) pure component critical point, (□) critical end point (CEP).

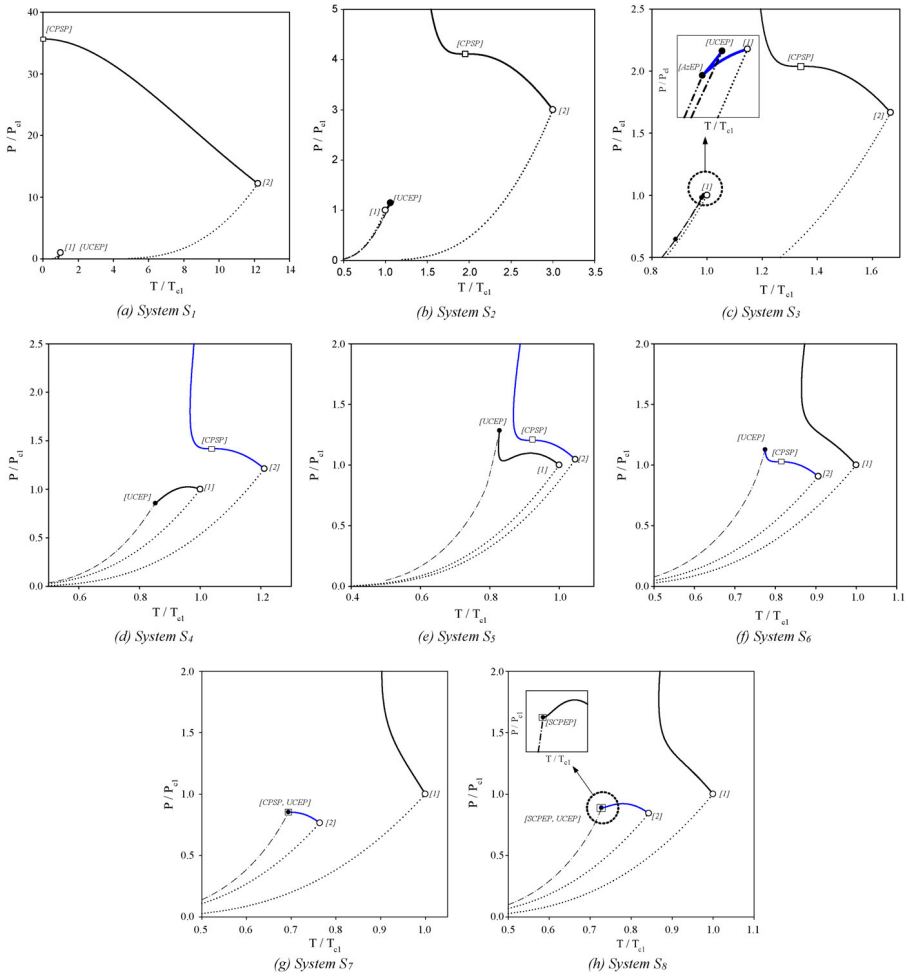

Fig. 7. Schematic *P–T* projections predicted for the binary systems indicated in the GPDs in Figs. 4 and 5. (▬) Stable critical line, (. . .) pure component vapor pressure line, (–·–) three phase line, (○) pure component critical point, (□) CPSP, (●) critical end point (CEP).

along the branch of the critical line that connects component {2}. Fig. 7b corresponds to the critical projection related to point S_2 in Fig. 4. Here the CPSP also appears along the critical branch that starts from component {2}, however, at non-zero temperature. In addition, the branch of the critical line containing the CPSP goes to infinite pressure as the temperature decreases. The example shown in Fig. 7b classifies as an ordinary Type *III* system.

Fig. 7c shows the critical projection drawn from point S_3 in Fig. 5. Point S_3 appears above the critical azeotropic end point line. In this case, a Type *III* system is obtained and the critical branch containing the CPSP activity is similar to the case shown in Fig. 7b. In addition, the system in consideration exhibits azeotropic behavior ending at the critical branch that emerges from component {1} in point [AzEP].

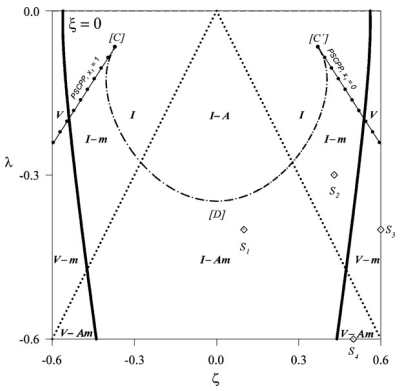

Fig. 8. Details of Fig. 4 in the vicinity of the goblet region. Captions as in Fig. 4.

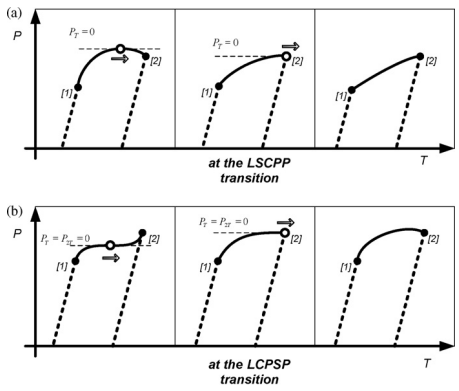

Fig. 9. Schematic mechanisms that delimit the goblet region. (▬) Stable critical line, (. . .) pure component vapor pressure line, (–●–) three phase line, (●) pure component critical point, (○) stationary critical pressure point.

Fig. 7d shows the critical projection obtained from point S_4 in Fig. 5, located above the *III–A–H* transition line. This latter transitional mechanism bounds stable azeotropy in the range of large ⍰ values. Consequently, the system shown in Fig. 7d does not exhibit stable azeotropy ending at the critical gas–liquid line. Inspection of Fig. 7b and d reveals that the critical temperature of the three-phase line is lower than the critical temperature of component {1}, thus giving place to Type *III*–H behavior.

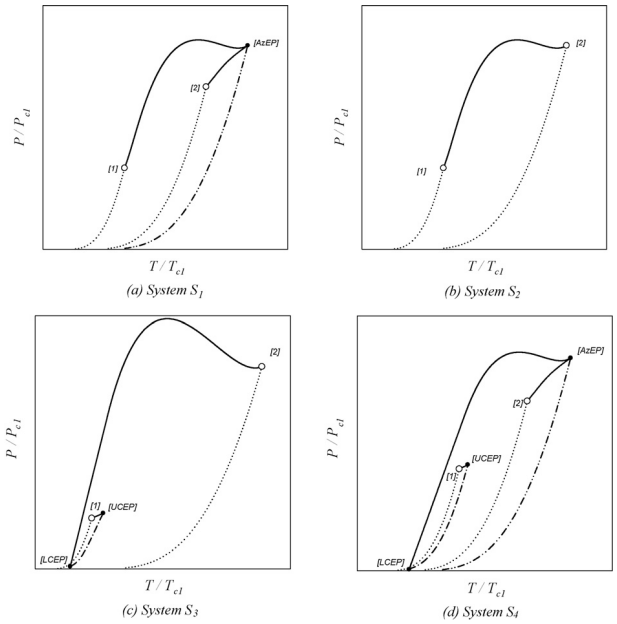

Fig. 10. Schematic *P–T* projections predicted for the binary systems indicated in the GPD in Fig. 8. (▬) Stable critical line, (. . .) pure component vapor pressure line, (–●–) three phase line, (–●●–) azeotropic line, (○) pure component critical point, (●) azeotropic end point.

Fig. 7e shows the critical projection corresponding to point S_5 in Fig. 5, which is above the *shield region* and inside the intersection of the left and right hand side cones of the *crown region*. Here we observe multiple pressure stationary points for the critical lines that start from both components. As shown in Fig. 7e, the CPSP is still present along the critical branch connecting component {2}, while the other branch exhibits two critical pressure stationary points of opposite concavity.

Fig. 7f shows the critical projection corresponding to point S_6 in Fig. 5, which is at the border of the region delimited by left hand side cone of the crown region, at a negative value. In this case, the upper CPSP line has crossed the line of symmetry of the GPD (=0) and, for this reason, component {2} has lower critical temperature than component [1]. As before, it is possible to observe that the CPSP appears along the critical branch that connects component {2}, while no stationary pressure point is observed along the critical branch that connects the other component. In addition, the branch of the critical line exhibiting CPSP activity is interrupted by an heteroazeotropic line instead of diverging to high pressure, as shown in Fig. 7a–e. In addition, it is extremely interesting to note that the shape of the *PT* projections presented in Fig. 7e–f exhibit close similarity to the schematic phase diagrams presented by Brunner [32] for interpreting the experimental data of the phase equilibrium of water + *n*-alkane systems.

Fig. 7g shows the critical projection corresponding to point S_7 in Fig. 5 (the upper limiting vertex in point A for the CPSP activity). In this case the heteroazeotropic line ends exactly at the CPSP.

Finally, Fig. 7h shows the critical projection corresponding to point S_8 in Fig. 5. This point occurs below the CPSP line, along the CSPEP line. It is also seen that the critical branch connecting component {2} exhibits two stationary critical pressure points. However, the heteroazeotropic line intersects now the critical pressure minimum thus limiting the min–max activity of the critical line.

3.2. Details of the lower branch of the CPSP: the goblet region

To the best of our knowledge, no previous work has described the evolution of multiple critical pressure stationary points for the case of mixtures characterized by negative values. The main attributes that distinguish this latter type of activity may be found inside the new parametric domain (here called the *goblet region*) shown in detail in Fig. 8. As seen, the goblet region appears below an ordinary CPSP transition line (the C–D–C′ curve, which exactly satisfies Eqs. (7.a) and (7.b)). In addition, it is also observed that the goblet region is bounded by the transitional mechanism LSCPP (limiting–stationary–critical–pressure–point), where the stationary pressure point of a critical line appears at the critical point of the pure component, as schematically shown in Fig. 9a. Particularly interesting in Fig. 8 is the topology of points C and C′ where, for the first time, we can observe that the CPSP of the critical line appears at the critical point of the pure component (LCPSP: limiting–CPSP), as schematically shown in Fig. 9b. Inside of the goblet region, and for the case of vdW mixtures composed by equally sized molecules, the activity of multiple critical pressure stationary points mainly affects both zeotropic and azeotropic binary systems classifying as Type *I* and *V* mixtures.

Although algebraic expressions have been reported for determining the slope of critical lines of binary mixtures [16,33], no systematic study has been undertaken to describe analytically the limiting geometry of the critical lines (slope and curvature) as they evolve from the critical points of the pure constituents at the *P*–*T* projection. Since these relationships are needed for establishing the key transitional mechanisms of the goblet region (namely, the LSCPP and LCPSP mechanisms) in this section we briefly discuss the theoretical framework required to provide the basis of their mathematical derivation. Following ideas from Prigogine and Defay [16], Eq. (1) may be expanded as a total differential equation in the canonical variables {*x*, *T*, *P*} of the mixture's Gibbs energy function *G*, yielding the following relationship for the curvature of the critical line

$$\frac{d^2P}{dT^2} = \frac{(G_{2xI}G_{3xP} - G_{2xP}G_{3xI})^2 - G_{4x}(G_{2x2P}G_{2xT}^2 + G_{2xP}(G_{2x2I}G_{2xP} - 2G_{2xI}G_{2xIP}))}{G_{2xP}^3 G_{4x}} \tag{10}$$

Eq. (10) unequivocally describes the curvature of the critical line at the *P*–*T* projection and, in the case of a critical pressure stationary point (where $G_{2xT}=0$), it simplifies to the following expression

$$\left(\frac{d^2P}{dT^2}\right)_{c,G_{2x2T}=0} = \frac{G_{3xT}^2 - G_{4x}G_{2x2T}}{G_{2xP}G_{4x}} \tag{11}$$

Certainly, Eqs. (11) and (7.b) may exhibit equivalent numerical roots of the state variables at a stationary critical pressure point, thus predicting the same thermomechanical equilibrium conditions for the CPSP. However, detailed inspection of Eqs. (10) and (11) allows deducing that Eq. (7.b) is not useful for *determining the value or the sign of the local curvature of a critical curve*, even for the simplest case of a pressure stationary point. After rigorous algebra, including Legendre transformations of the Gibbs energy function, application of Eqs. (1) and (10) to the pure components ($x_1=0$ or $x_1=1$), yields the following analytical relationships for the limiting slope and curvature of the critical lines

$$\left(\frac{dP}{dT}\right)_{c,x_1=0} = -\lim_{x_1\to 0}\left[A_{vT} + \frac{RTA_{2vT}A_{xv}}{A_{xv}^2 - RTA_{x2v}}\right] \tag{12.a}$$

$$\left(\frac{d^2P}{dT^2}\right)_{c,x_1=0} = -\lim_{x_1\to 0}\left[\frac{(A_{xv}^2 - A_{x2v}RT)^2 h_6 + (A_{xv}^2 - A_{x2v}RT)(h_1-h_2) - A_{2vT}^2(h_3+h_4)}{A_{4v}RT(A_{xv}^2 - A_{x2v}RT)^3}\right] \tag{12.b}$$

$$\left(\frac{dP}{dT}\right)_{c,x_1=1} = -\lim_{x_1\to 1}\left[A_{vT} - \frac{RTA_{2vT}A_{xv}}{A_{xv}^2 + RTA_{x2v}}\right] \tag{12.c}$$

$$\left(\frac{d^2P}{dT^2}\right)_{c,x_1=1} = -\lim_{x_1\to 1}\left[\frac{(A_{xv}^2 + A_{x2v}RT)^2 h_7 - (A_{xv}^2 + A_{x2v}RT)(h_1+h_2) + A_{2vT}^2(h_3+h_5)}{A_{4v}RT(A_{xv}^2 + A_{x2v}RT)^3}\right] \tag{12.d}$$

where the coefficients h_i of Eqs. (12.a)–(12.d) are defined as

$$h_1 = 2A_{2vT}RT(A_{3vT}A_{xv}^4 + R^2T^2\{A_{3vT}A_{x3v}A_{xv} + A_{4v}A_{x2v}A_{xvT} - A_{4v}A_{x2vT}A_{xv}\})$$

$$h_2 = 2A_{2vT}A_{xv}^2R^2T(3TA_{3vT}A_{x2v} + A_{4v}\{A_{xv} - TA_{xvT}\})$$

$$h_3 = A_{xv}^7 + A_{xv}^3(-2A_{4v}A_{2x}^R + 9A_{x2v}^2 + 2A_{x3v}A_{xv})R^2T^2 + (A_{2xv}A_{4v}A_{x2v} + \{A_{x3v}^2 - A_{2x2v}A_{4v}\}A_{xv})R^4T^4 \quad (13)$$

$$h_4 = -6A_{x2v}A_{xv}^5RT - A_{xv}^2(6A_{x2v}A_{x3v} + 2A_{xv}A_{4v} - 3A_{2xv}A_{4v})R^3T^3$$

$$h_5 = 6A_{x2v}A_{xv}^5RT - A_{xv}^2(3A_{2xv}A_{4v} - 6A_{x2v}A_{x3v} + 2A_{xv}A_{4v})R^3T^3$$

$$h_6 = RT(A_{4v}A_{v2T}A_{xv}^2 - \{A_{4v}A_{v2T}A_{x2v} + A_{3vT}^2A_{xv} - A_{2v2T}A_{4v}A_{xv}\}RT)$$

$$h_7 = RT(A_{4v}A_{v2T}A_{xv}^2 + \{A_{4v}A_{v2T}A_{x2v} + A_{3vT}^2A_{xv} - A_{2v2T}A_{4v}A_{xv}\}RT)$$

and A_{2x}^R stands for the residual Helmholtz energy that may be calculated as

$$A_{2x}^R = A_{2x} - \frac{RT}{x_1x_2} \quad (14)$$

Equating Eqs. (12.a) and (12.c) to zero allows calculating the right and the left branches of the LSCPP transitional lines, respectively. In addition, the simultaneous annulation of Eqs. (12.a–12.b) (or, equivalently, Eqs. (12.c–12.d) yields the LCPSP in point C (or, equivalently, in point C′). It is interesting to note that Eqs. (12.a)–(12.d) are applicable *to every EOS model* thus allowing the derivation of useful quadratic approximations for predicting the geometry of the critical line in the vicinity of pure components.

Fig. 10 depict the critical *PT* projections of the different subclasses that may be drawn from the goblet region predicted by the vdW-EOS. In particular, Fig. 10a corresponds to the *P–T* projection of a binary mixture with the parameters indicated by point S_i in Fig. 8. In this case it can be observed that the global coordinates of the mixture are between azeotropic transitional lines and below the CPSP transition limit (curve CDC′). As expected from a Type I–A mixture, system S_i exhibits a critical azeotropic end point. In addition, the CPSP activity is clearly reflected by multiple pressure

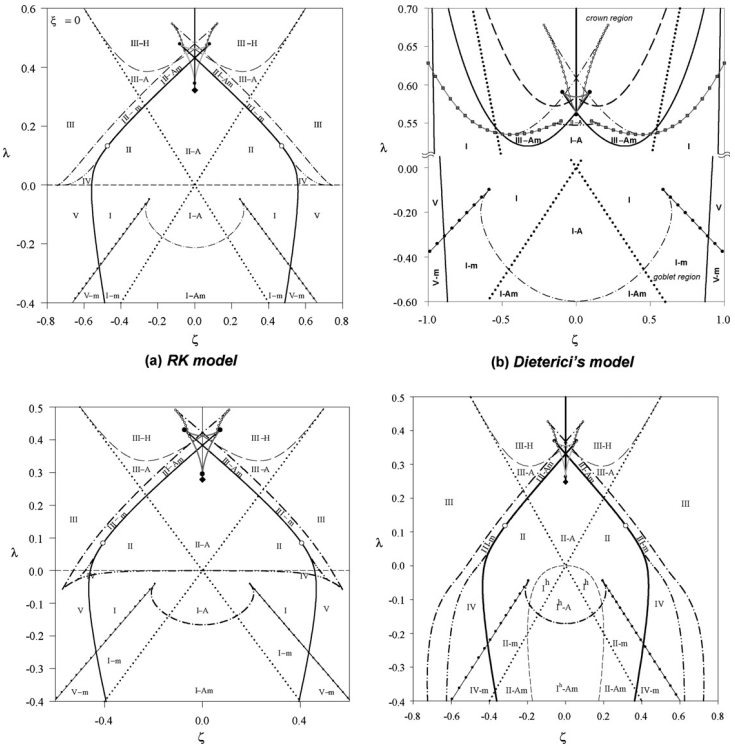

Fig. 11. Global Phase Diagram for mixtures with molecules of equal size ($\Re = 0$). (▬) Tricritical line, (– – –) zero temperature line, (. . .) line of critical azeotropy, (–·–) CPSP line, (–··–) DCEP line, (——) III–A–H transition line, (▒) shield region boundary, (–○–) stationary critical pressure end point (SCPEP), (–●–) limiting stationary critical pressure point (LSCPP), (○) van Laar points, (●) tricritical end points for the shield region, (♦) low pressure tricritical endpoint, (▩) hypercritical mathematical double point (HMDP) for the Dieterici model.

stationary points along the critical line. Fig. 10b corresponds to the phase diagram of the binary mixture having the parameters taken from point S_2 in Fig. 8, which also classifies as a Type I system. The mixture shown in Fig. 10b exhibits CPSP activity along the critical branch that connects the critical points of the pure components; however, in this case, no azeotrope is present. Fig. 10c depicts the *P*–*T* projection of the binary mixture with the parameters taken from point S_3 in Fig. 8, where immiscibility corresponding to Type-*V* activity appears due to the tricritical transition. Mixture S_3 exhibits CPSP activity along the critical branch that emerges from {2} and no azeotrope is present.

Finally, Fig. 10d shows the *P*–*T* projection of the mixture with the parameters taken from point S_4 in Fig. 8. Similarly to systems S_3, systems S_4 exhibit CPSP behavior along the critical branch that emerges from component {2} and, since its global coordinates are between azeotropic lines, an azeotropic end point is also observed along the critical branch.

3.3. CPSP activity in cubic models of the van der Waals type and in theoretical EOS models

So far we have illustrated the main features of the CPSP activity for the case of vdW binary mixtures. However, as pointed out before, the transitional mechanisms that delimit the crown and goblet regions are valid for every EOS model. Consequently, these mechanisms may be applied to other EOSs to analyze whether these predicted regions are particular for the vdW fluids or are a general prediction of EOSs models.

Fig. 11 depict the complete versions of the GPDs for molecules of equal size, as predicted by cubic-type and molecular based EOS models. Particularly, Fig. 11a presents the GPD of the Redlich–Kwong model, which corresponds to a reference improvement of the vdW model. Fig. 11b shows the GPD for Dieterici fluids, illustrating a situation in which hybrid rather than conventional types of behavior may be observed due to the prediction of a hypercritical mathematical double point (HMDP) mechanism. As discussed in [34,35], the HMDP of the Dieterici's model produces stable closed loops of immiscibility for every combination of the global parameters. Fig. 11c illustrates the GPD predicted by the Carnahan–Starling–Redlich–Kwong (CSRK) model, whose main characteristics have been explained by Kraska and Deiters and Bidart et al. Finally, Fig. 11d shows the GPD of the original SAFT model [36], as predicted for binary mixtures constituted by spherical monomers of equal diameter.

From Fig. 11 we can deduce that although the types of behavior predicted by other EOSs do not directly correspond to those observed for van der Waals binary fluids (excepting the cases of the RK and CSRK models) the main characteristics, shapes and relative global coordinates of the crown and goblet regions are preserved in the GPD of substantially different EOS models.

4. Concluding remarks

In this work we have presented a detailed description of the CPSP activity, considering the full range of mixture properties over which it can be observed for the case of molecules of equal sizes. The results clearly demonstrate the existence of two new well-defined regions of the GPD, namely the crown and the goblet region, where the impact of the CPSP is clearly observed on the geometry of phase diagrams predicted by EOS models based on different theoretical basis. According to the results, the crown region is related to systems that exhibit strong positive deviations from ideal behavior, typically Type III–H mixtures, where immiscibility interrupts the critical gas–liquid line. The goblet region, in turn, is mainly related to Type I and V systems, where mixtures essentially show negative deviation from ideal behavior.

Acknowledgements

This work has been partially financed by *FONDECYT*, Chile (Project 1080596) and by the *ACS Petroleum Research Fund* grant No. PRF#47338-B6. M. Flores acknowledges a doctoral grant from the *Comisión Nacional de Ciencia y Tecnología, Conicyt*, Chile. M.J. Tardón acknowledges a doctoral scholarship from the *Dirección de Postgrado, Universidad de Concepción*.

Appendix A. Legendre transformations for Eqs. (7.a) and (7.b)

$$v_x = -\frac{A_{xv}}{A_{2v}}$$

$$G_{2x} = A_{2x} + A_{xv}v_x$$

$$G_{3x} = A_{3x} + 3A_{2xv}v_x + 3A_{x2v}v_x^2 + A_{3v}v_x^3$$

$$G_{4x} = A_{4x} + 4A_{3xv}v_x + 6A_{2x2v}v_x^2 + 4A_{x3v}v_x^3 + A_{4v}v_x^4 - \frac{3}{A_{2v}}[A_{2xv} + 2A_{x2v}v_x + A_{3v}v_x^2]^2$$

$$G_{2xT} = A_{2xT} + \frac{v_x}{A_{xv}}[A_{2xv}A_{vT} + 2A_{xv}A_{xvT} + v_x(2A_{vT}A_{x2v} + A_{2vT}A_{xv} + v_xA_{3v}A_{vT})]$$

$$G_{3xT} = A_{3xT} + \frac{V_x}{A_{xv}^2}\left\{\begin{array}{r} A_{3xv}A_{vT}A_{xv} + 3A_{xv}(A_{2xvT}A_{xv} + A_{2xv}A_{xvT}) + 3A_{3v}^2A_{vT}v_x^4 \\ +3v_x(A_{2xv}A_{vT}A_{x2v} + A_{2vT}A_{2xv}A_{xv} + A_{2x2v}A_{vt}A_{xv} + A_{x2vT}A_{xv}^2 + 2A_{x2v}A_{xv}A_{xvT}) \\ +v_x^2(3A_{2xv}A_{3v}A_{vT} + 6A_{vT}A_{x2v}^2 + 6A_{2vT}A_{x2v}A_{xv} + 3A_{vT}A_{x3v}A_{xv} + A_{3vT}A_{xv}^2 + 3A_{3v}A_{xv}A_{xvT}) \\ +v_x^3(9A_{3v}A_{vT}A_{x2v} + 3A_{2vT}A_{3v}A_{xv} + A_{4v}A_{vT}A_{xv}) \end{array}\right\}$$

$$G_{2x2T} = \frac{1}{A_{xv}^3}\left[\begin{array}{r} A_{2x2T}A_{xv}^3 + A_{xv}^2v_x[A_{2xv}A_{v2T} + 2\{A_{2xvT}A_{vT} + A_{xv}A_{xv2T} + A_{xvT}^2\}] \\ +A_{xv}v_x^2(A_{2x2v}A_{vT}^2 + A_{xv}\{2A_{v2T}A_{x2v} + 4A_{vT}A_{x2vT} + A_{2v2T}A_{xv}\} + 4A_{vT}A_{x2v}A_{xvT} + 2A_{2vT}\{A_{2xv}A_{vT} + 2A_{xv}A_{xvT}\}) \\ +v_x^3(A_{2xv}A_{3v}A_{vT}^2 + A_{xv}^2\{2A_{2vT}^2 + A_{2v}A_{v2T}\} + 2A_{vT}^2\{A_{x2v}^2 + A_{x3v}A_{xv}\} + 2A_{vT}A_{xv}\{4A_{2vT}A_{x2v} + A_{3vT}A_{xv} + 2A_{3v}A_{xvT}\}) \\ +A_{vT}v_x^4(A_{4v}A_{vT}A_{xv} + 6A_{3v}\{A_{vT}A_{x2v} + A_{2vT}A_{vx}\} + 3A_{3v}^2A_{vT}^2v_x^5) \end{array}\right]$$

References

[1] P.H. van Konynenburg, Critical Lines and Phase Equilibria in Binary Mixtures, Ph.D. Thesis, University of California, Los Angeles, 1968.
[2] P.H. van Konynenburg, R.L. Scott, Critical Lines and Phase Equilibria in Binary van der Waals Mixtures, vol. 298 A, Phil. Trans. Royal Society, London, 1980, pp. 495–539.
[3] G.M. Schneider, The continuity and family concepts: useful tools in fluid phase science, Phys. Chem. Chem. Phys. 6 (2004) 2285–2290.
[4] A. Bolz, U.K. Deiters, C.J. Peters, T.W. De Loos, Nomenclature for phase diagrams with particular reference to vapour–liquid and liquid–liquid equilibria, Pure Appl. Chem. 70 (1998) 2233–2257.

[5] J.N. Canongia–Lopes, Phase equilibria in binary–Lennard–Jones mixtures: phase diagram simulation, Mol. Phys. 96 (1999) 1649–1658.
[6] A. Mejía, J. Pamiés, D. Duque, H. Segura, L.F. Vega, Phase and interface behaviors in Type–I and Type–V Lennard–Jones mixtures: theory and simulations, J. Chem. Phys. 123 (2005) 1–10, 034505.
[7] A. Mejía, H. Segura, Interfacial behavior in Type IV systems, Int. J. Thermophys. 25 (2004) 1395–1414.
[8] A. Mejía, H. Segura, On the interfacial behavior about the shield region, Int. J. Thermophys. 26 (2005) 13–29.
[9] K. Gauter, C.J. Peters, A.L. Scheidgen, Cosolvency effects, miscibility windows and two-phase LG holes in three-phase LLG surfaces in ternary systems: a status report, Fluid Phase Equilib. 171 (2000) 127–149.
[10] L.Z. Boshkov, L.V. Yelash, Closed loops of liquid–liquid immiscibility in binary mixtures predicted from the Redlich–Kwong equation of state, Fluid Phase Equilib. 141 (1997) 105–112.
[11] I. Polishuk, J. Wisniak, H. Segura, Transitional behavior of phase diagrams predicted by the Redlich–Kwong EOS and classical mixing rules, Phys. Chem. Chem. Phys. 1 (1999) 4245–4250.
[12] L.V. Yelash, T. Kraska, Investigation of a generalized attraction term of an equation of state and its influence on the phase behavior, Fluid Phase Equilib. 162 (1999) 115–130.
[13] C. Bidart, H. Segura, J. Wisniak, Phase equilibrium in water (1) + *n*-alkane (2) mixtures, Ind. Eng. Chem. Res. 46 (2007) 947–954.
[14] N.F. Carnahan, K.E. Starling, Equation of state for nonattracting rigid spheres, J. Chem. Phys. 51 (1969) 635–636.
[15] D. Furman, R.B. Griffiths, Global Phase Diagram for a van der Waals model of a binary mixture, Phys. Rev. A 17 (1978) 1139–1148.
[16] I. Prigogine, R. Defay, Chemical Thermodynamics, Longmans, Green and Co. Ltd., London, 1954.
[17] H. Segura, J. Wisniak, Influence of excess properties on binary liquid–liquid equilibrium, Chem. Eng. Sci. 52 (1997) 597–610.
[18] J.P. Novák, J. Matous, J. Pick, Liquid–liquid Equilibria, Elsevier, Amsterdam, 1987.
[19] J.S. Rowlinson, F.L. Swinton, Liquids and Liquid Mixtures, 3th ed., Butterworth Scientific, London, 1982.
[20] J.P. Kuenen, Measurements concerning the surface of van der Waals for mixtures of carbonic acid and methyl chloride, Comm Leiden 4 (1892) 422–424.
[21] Ø. Mørch, Kh. Nasrifar, O. Bolland, E. Solbraa, A.O. Fredheim, L.H. Gjertsen, Measurement and modeling of hydrocarbon dew points for five synthetic natural gas mixtures, Fluid Phase Equilib. 239 (2006) 138–145.
[22] F.A. Escobedo, Molecular and macroscopic modeling of phase separation, AIChE J. 46 (2000) 2086–2096.
[23] P.T. Eubank, M.A. Barrufet, General conditions of colinearity at the phase boundaries of fluid mixtures, AIChE J. 33 (1987) 1882–1887.
[24] J. Wisniak, A. Apelblat, H. Segura, The solubility of gases in liquids, Phys. Chem. Liq. 34 (1997) 125–153.
[25] J. Wisniak, A. Apelblat, H. Segura, Prediction of gas–solid equilibrium using equations of state, Fluid Phase Equilib. 147 (1998) 45–64.
[26] L.Z. Boshkov, Bifurcations—a possibility to generalize the thermodynamic description of phase diagrams of two component fluid, Ber. Bunsenges Phys. Chem. 96 (1992) 940–943.
[27] J.W. Tester, M. Modell, Thermodynamics and its Applications, Prentice Hall, New Jersey, 1996.
[28] T. Kraska, U.K. Deiters, Systematic investigation of phase behavior in binary fluid mixtures. II. Calculations based on the Carnahan–Starling–Redlich–Kwong equation of state, J. Chem. Phys. 96 (1992) 539–547.
[29] U.K. Deiters, I.L. Pegg, Systematic investigation of the phase behavior in binary fluid mixtures. I. Calculations based on the Redlich–Kwong equation of state, J. Chem. Phys. 90 (1989) 6632–6641.
[30] M.L. Michelsen, The isothermal flash problem. Part I. Stability, Fluid Phase Equilib. 9 (1982) 1–19.
[31] H. Segura, I. Polishuk, J. Wisniak, Phase stability analysis in binary systems, Phys. Chem. Liq. 38 (2000) 277–331.
[32] E. Brunner, Fluid mixtures at high pressures. IX. Phase separation and critical phenomena in 23 (*n*-alkane + water) mixtures, J. Chem. Thermodyn. 22 (1990) 335–353.
[33] J. Jiang, J.M. Prausnitz, Critical temperatures and pressures for hydrocarbon mixtures from an equation of state with renormalization group-theory corrections, Fluid Phase Equilib. 169 (2000) 127–147.
[34] I. Polishuk, R. Gonzálex, J.H. Vera, H. Segura, Global Phase Diagram analysis of the Dieterici equation of state, Phys. Chem. Chem. Phys. 22 (2004) 5189–5194.
[35] I. Polishuk, J.H. Vera, H. Segura, Azeotropic behavior in Dieterici binary fluis, Fluid Phase Equilib. 257 (2007) 18–26.
[36] W.G. Chapman, K.E. Gubbins, G. Jackson, M. Radosz, New reference equation of state for associating liquids, Ind. Eng. Chem. Res. 29 (1990) 1709–1721.

CAPÍTULO V

5. Aproximación topológica del fenómeno barotrópico másico en mezclas asimétricas

Artículo publicado en Fluid Phase Equilibria, 313 (2012) 171-181

La inversión de densidad másica, conocida como barotropía másica, es un fenómeno muy particular del equilibrio de fases y tiene directa injerencia en la posición relativa de las fases cuando son expuestas a campos gravitacionales. A pesar de ser un fenómeno bastante conocido, se han realizado pocos esfuerzos para explicar su presencia desde un punto de vista teórico.

En este artículo, extensión del CAPÍTULO III, se ahonda en la descripción del fenómeno barotrópico másico distinguiéndolo claramente de la conducta isopínica (inversión de densidades molares). Se desarrolla una metodología de estudio que permite obtener un conjunto de ecuaciones que se corresponden a un mecanismo transicional global para el fenómeno barotrópico heteroazeotrópico en mezclas asimétricas. Los resultados obtenidos, utilizando PC-SAFT y spd-GPD, son contrastados con lo observado experimentalmente para la serie de CO_2+n-alcano, encontrándose buena concordancia. Se encontró barotropía principalmente ligada a *Tipo III* y *Tipo IV*, pero en el artículo se indica al menos teóricamente, presencia en *Tipo II*. Por ello se descarta que el "Punto Matemático Doble (MDP) ", sea responsable de la conducta barotrópica en mezclas donde no exista asociación.

Para más detalles ver el artículo que se adjunta a continuación:

Fluid Phase Equilibria 313 (2012) 171–181

Contents lists available at SciVerse ScienceDirect

Fluid Phase Equilibria

journal homepage: www.elsevier.com/locate/fluid

A topological approach to mass barotropic phenomena in asymmetric mixtures

Mauricio E. Flores[a,1], María José Tardón[a], Christian Bidart[b], Andrés Mejía[a], Hugo Segura[a,*]

[a] Department of Chemical Engineering, Universidad de Concepción, 4070386 Concepción, Chile
[b] Karlsruher Institut für Technologie (KIT), Institut für Industriebetriebslehre und Industrielle Produktion (IIP), Hertzstrasse 16, 76187 Karlsruhe, Germany

ARTICLE INFO

Article history:
Received 21 July 2011
Received in revised form
27 September 2011
Accepted 29 September 2011
Available online 14 October 2011

Keywords:
Barotropic phenomena
Equations of state
Phase equilibrium
Global phase diagram
PC-SAFT

ABSTRACT

Mass density inversion, a phenomenon also known as mass barotropy, corresponds to a singular behavior that directly affects the relative position of phases in heterogeneous mixtures when exposed to gravitational fields. In this contribution we introduce a topological description of the mass density inversions observed in asymmetric binary mixtures, a case that is appropriately exemplified by the evolution of the barotropy experimentally observed in carbon dioxide + hydrocarbon mixtures. From this basic example, necessary and sufficient conditions are deduced for exhibiting mass density inversions in direct relation with the global phase behavior of the mixture. Finally, the global phase diagram (GPD) predicted by the PC-SAFT equation is used for describing barotropic ranges in mixtures composed by carbon dioxide and hydrocarbons of increasing chain length, together with the specific effects that transitional mechanisms induce on the phenomenon.

In excellent agreement with the available experimental data, results show that mass barotropy is present over ranges essentially involving Type III and IV systems. In addition, since the phenomenon is shown to appear also in Type II systems, it is concluded that mathematical double point (MDP) transitions do not necessarily control barotropic behavior. Finally, the occurrence of double critical end points satisfying the conditions of mass barotropy unequivocally explains the shift of barotropic points along the branch(es) of the liquid–liquid–gas line, as the alkane's chain length increases.

1. Introduction

The phase behavior of asymmetric mixtures exhibits complex and singular patterns, such as closed and open immiscibility gaps, homogeneous and heterogeneous azeotropy, closed loops of immiscibility, miscibility holes in ternary mixtures and barotropy (or density inversion); among others [1]. Each one of these patterns has distinctive attributes that may be conveniently exploited for the design and operation of separation and/or mixing processes, rationalization whose effectivity depends on a deep understanding of the specific phenomena that mixtures exhibit, as well as on the availability of experimental and/or theoretical information concerning their physico-chemical properties.

Practice has shown us that experimental efforts for determining detailed phase equilibrium information are prohibitive for several practical cases, in both time and cost. Consequently, reliable theoretical approaches for predicting equilibrium behaviors in ranges not covered by experimentation are extremely valuable for practical purposes. The Master or global phase diagram (GPD) of an accurate equation of state (EOS), a powerful tool that was introduced in the seminal work of van Konynenburg and Scott [2], provides one of the most fruitful of these theoretical approaches. Briefly, a GPD allows detailed classification of mixtures predicted by equations of state (EOS) according to the main attributes that characterize their phase equilibrium topology, namely: presence or absence of azeotropy, total or partial miscibility between the coexisting phases, continuity or discontinuity of critical lines, etc. A GPD plot maps regions of clearly defined EOS's parameters inside of which binary systems exhibit comparable equilibrium patterns. These regions, which are precisely bounded by well-defined transitional mechanisms (or transitional lines), give place to the modern classification of phase behaviors in Types [3]. Nowadays, general purpose van der Waals (vdW) cubics and more theoretically inspired EOSs are able to display GPDs showing the six main Types of behavior depicted in Fig. 1, which are in excellent agreement with the general trends observed in experimental results for real mixtures. Certainly, the GPD approach provides a useful link between the physical properties and affinity of the constituents of mixtures and the specific features that characterize their phase behaviors. Moreover, the continuous development of theoretically based EOSs under the guidance molecular simulations, has allowed the

* Corresponding author. Fax: +56 41 2247491.
E-mail address: hsegura@udec.cl (H. Segura).
[1] Present address: Centro Científico y Tecnológico de Excelencia Unidad de Desarrollo Tecnológico (CCTE-UDT)-Universidad de Concepción, Post Code 4191996, Casilla N° 4051, Correo 3, Concepción, Chile.

0378-3812/$ – see front matter © 2011 Elsevier B.V. All rights reserved.
doi:10.1016/j.fluid.2011.09.030

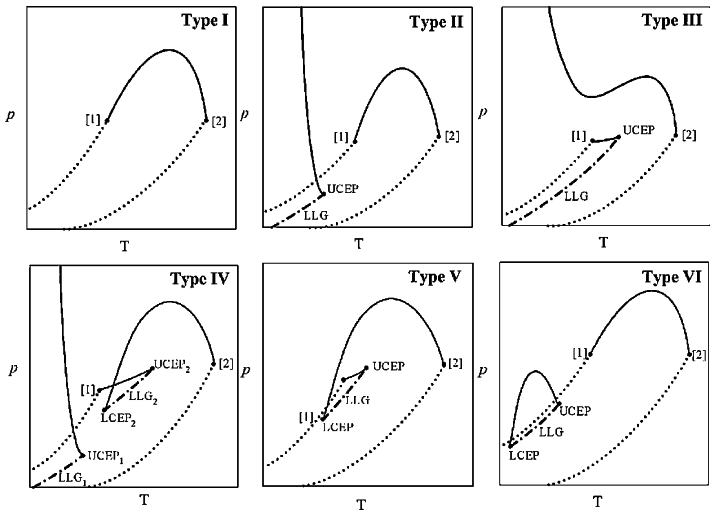

Fig. 1. Critical phase behaviors according to the classification of van Konynenburg and Scott [2]. (▬) Critical line, (···) vapor pressure line, and (–·–) three phase line.

development of GPDs that provide a deeper understanding of the impact of specific molecular effects on the macroscopic behavior of fluid mixtures.

This work aims to describe the phenomenon of mass barotropy or mass density inversion (MaDI) in direct relation to the phase equilibrium topology that characterizes the subset of binary mixtures exhibiting such a behavior. Particularly, (mass) barotropy – a term early coined by Kamerlingh Onnes [4] – corresponds to a singular equilibrium state of heterogeneous fluid mixtures in which – at least – two phases of a heterogeneous mixture have equivalent mass density, thus inverting their relative position in a gravitational field. This abnormal mass density inversion of immiscible phases was experimentally observed for the first time by Kamerlingh Onnes at the Leiden Physics Laboratory in 1906, when liquefying the helium + hydrogen mixture at 20 K and circa 50 atm [4]. Since then, barotropic inversion has also been experimentally detected in CO_2 + n-C_nH_{2n+2} [1], H_2O + n-C_nH_{2n+2} [5], R-OH + n-C_nH_{2n+2} [6] and CO_2 + alkyl benzenes [7], which constitute relevant examples of mixtures involved in key technological processes.

Closely related to mass barotropic inversion, molar barotropic behavior (or molar density inversion, MoDI) corresponds to a case in which the molar density values of – at least – two phases of a heterogeneous mixture invert. In this latter case, and depending on the molecular weight of the involved phases, gravitational fields do not necessarily affect the behavior of the mixture. Consequently, and in contrast to mass barotropic behavior, MoDIs are not directly observable in phase equilibrium experiments, but they must be detected either by directly measuring molar densities or by applying accurate EOSs to predicting the molar density of the coexisting phases [8]. It should be noted that mass and molar barotropic behavior become equivalent in the less probable case in which the constituents of the mixture have equivalent molecular weight.

The discussion about how density inversions may be affected by the Type of behavior – clearly establishing the limiting conditions of existence and considering the contribution of the molecular properties of the constituents – is not clear cut so far. Only recently, Quiñones-Cisneros [8,9] described MoDIs at the light of global pressure–temperature (P–T) projections of CO_2 + n-C_nH_{2n+2} mixtures, as predicted from the Perturbed Chain-Statistical Associated Fluid Theory (PC-SAFT) model [10]. The results obtained by Quiñones-Cisneros allow concluding that the global phase behavior of CO_2 + hydrocarbon mixtures may be unequivocally rationalized in terms of a II–IV–III transition which, as the molecular chain length of the hydrocarbon increases, is controlled by an appropriate coordination of tricritical (TC) and double critical end point (DCEP) mechanisms. Combining intuitive ideas from Keesom and Kamerlingh Onnes [4], Quiñones-Cisneros described the singular geometry of the tie lines in a (molar) *v*–*x* projection for phases characterized by MoDI. The mathematical consequences of these geometric observations were then analyzed at the critical range, from which Quiñones-Cisneros was able to demonstrate that the critical eigenvector of the Hessian matrix of the Helmholtz function is characterized by a nil component for the volume direction at a critical barotropic point. Such a mathematical framework allowed also concluding the following observations for the MoDIs observed in carbon dioxide + hydrocarbon mixtures:

I. A transitional high order double spinodal (formally, a mathematical double point or MDP [11]) is responsible that in asymmetric systems, molar barotropic phenomenon is strongly linked to Type III.
II. In asymmetry induced barotropic behavior, for mass density inversion to occur, molar density inversion is a necessary condition.
III. For strong barotropic behavior to develop it is required that the critical curves originating at the pure component critical points be disjoined.

In a complementary investigation, Bidart et al. [12] described the MaDIs observed in H_2O + n-C_nH_{2n+2} mixtures, as predicted by the Carnahan–Starling–Redlich–Kwong (CSRK) EOS. In their approach, Bidart et al. evaluated how the chain length of the

Table 1
Pure component properties and interaction parameter of a van der Waals binary mixture that exhibits molar density inversion.

T_{c2}/T_{c1}	P_{c2}/P_{c1}	k_{12}
3.667	1.222	0.095

accompanying n-alkane affected the mass barotropy and phase behavior of the involved mixtures. According to results, and in contrast to the case of CO_2 + hydrocarbons, water + hydrocarbon mixtures exhibited Type III behavior only (in direct coherence with experimental results [5]), and appeared in a parametrical range of a GPD which is immediately located above the shield region. The phase behavior of these aqueous–organic mixtures is characterized by an interchange of the critical branches that connect the pure components and, once again, the evolution of their phase diagrams on the molecular weight of the hydrocarbon was explained in terms of the coordination of tricritical and DCEP mechanisms.

Accordingly, the theoretical and experimental evidence accumulated so far allows one to reasonably conclude that barotropy may be a consequence of an appropriate coordination of tricritical and DCEP mechanisms. Particularly, the ordinary MDP mechanism occurs between tricritical and DCEP mechanisms, precisely the parametrical range of the GPD where Quiñones-Cisneros [9] detected a sign of change for critical volume component of the eigenvector of the critical Helmholtz Hessian matrix. However, although unstable MDPs were identified in the vicinity of the barotropic inversions predicted for water + hydrocarbon mixtures, it was demonstrated that critical mechanisms do not necessarily constraint mass barotropy because the phenomenon clearly involved volumes of non-critical phases at its limiting point.

Consequently, it seems that MaDIs and MoDIs may display different behavior between comparable transition limits, thus suggesting the need of a specific analysis in order to unequivocally determine the impact of critical transitions on the limiting conditions for each case. In order to do so, let us consider a simple example that clearly illustrates some basic differences between MaDIs and MoDIs. In Table 1 we report the critical properties of the constituents of a typical van der Waals binary mixture composed by spherical molecules of different diameter ($\varepsilon_2^3/\varepsilon_1^3 = 3$). As shown in Fig. 2, the quoted mixture is clearly characterized by a MoDI locus which begins in a three phase line at the sub-critical point A and ends in a critical point in B. Depending on the molecular weight ratio between components ($q = M_{w2}/M_{w1}$), we can observe that the mixture may present a MaDI locus. Particularly, Fig. 2 depicts the case for which $q = 1.5$, where it can be observed that – as the MoDI line – the MaDI locus begins in a three phase line at the sub-critical point C and ends at the critical point D. However, these latter results also demonstrate that MoDIs and MaDIs are not directly comparable since, although they may present similar limiting conditions, they are indeed characterized by completely different thermo-mechanical conditions. Consequently, considering that MoDIs and MaDIs present different critical coordinates, it is neither clear whether they may be affected by equivalent transitional mechanisms nor how the presence of one effect may induce the presence of the other. In fact, for the case shown in Fig. 2, MaDIs can be observed over a limited q range ($3 > q > 0$) only, thus indicating that MoDIs do not necessarily induce MaDIs.

It is quite clear then that the characterization of mass barotropic phenomena is not a solved problem yet, since the specific effects of their limiting mechanisms should be taken into account in a mass density basis for the purpose of unequivocally describing their existence and persistence. Consequently, this research aims to characterize the global phase behavior of asymmetric mixtures characterized by mass barotropy, in order to contribute to a better understanding of how MaDIs and the corresponding phase behavior are linked.

2. Theory and methods

Due to their significant industrial relevance and unequivocal evidence of mass barotropic behavior, binary systems containing CO_2 + n-C_nH_{2n+2} have been considered as reference asymmetric mixtures. The phase behavior of the quoted mixtures has been satisfactorily predicted from the PC-SAFT EOS, whose flexibility for representing both quantitatively and qualitatively the experimental behavior of common industrial systems is well-known.

The theoretical basis together with an authoritative description of the PC-SAFT model can be found in the literature [9,10,13]. Briefly, the model is a perturbation theory that considers molecules to be chains of spherical segments interacting by means of the square-well potential. A hard chain reference is assumed and a specific term related to dispersion forces between chains is added. For non-associative molecules of similar type, three pure component parameters are required: m_i (segments number in chain of component i), ε_i (segment diameter) and $\mathbb{I}_i$ (potential depth). The molecular parameters for CO_2 have been directly taken from Gross and Sadowski [10], and are presented in Table 2. In the case of

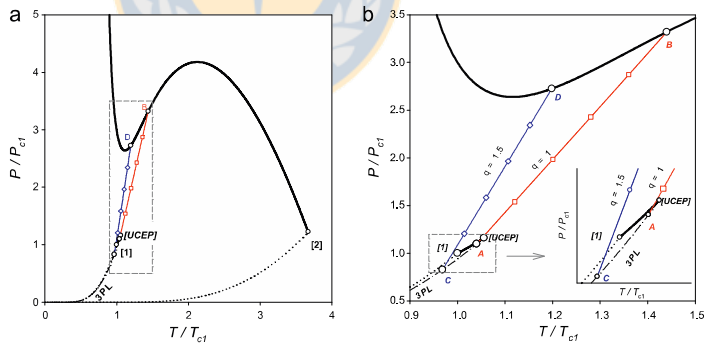

Fig. 2. (a) Critical P–T projections for the van der Waals mixture indicated in Table 2. (▬) Critical line, (···) vapor pressure line, (– · –) three phase line 3PL, (▬□▬) MoDI line, and (▬◇▬) MaDI line. (b) Details of (a) about the barotropic geometrical loci. Captions as in (a).

Table 2
PC-SAFT pure-component parameters for CO_2.

εk^{-1} (K)	σ (Å)	m
169.21	2.7852	2.0729

the hydrocarbons series, the molecular parameters of the n-alkane have been correlated with molecular weight (M_{wi}) according to the following relationships [10]:

$$\sigma_i = q_{01} + \frac{M_{wi} - M_{w,CH_4}}{M_{wi}}\left(q_{11} + \frac{M_{wi} - 2M_{w,CH_4}}{M_{wi}}q_{21}\right) \quad (1)$$

$$\frac{m_i}{M_{wi}} = q_{02} + \frac{M_{wi} - M_{w,CH_4}}{M_{wi}}\left(q_{12} + \frac{M_{wi} - 2M_{w,CH_4}}{M_{wi}}q_{22}\right) \quad (2)$$

$$\frac{\varepsilon_i}{k} = q_{03} + \frac{M_{wi} - M_{w,CH_4}}{M_{wi}}\left(q_{13} + \frac{M_{wi} - 2M_{w,CH_4}}{M_{wi}}q_{23}\right) \quad (3)$$

In Eqs. (1)–(3), M_{w,CH_4} (=16.0428) corresponds to the molar mass of methane and Table 3 reports the set of constants required for evaluating the molecular parameters. It should be pointed out that the parameters of the pure components considered in this work have not been rescaled [14] and, therefore, the predicted critical points of the pure constituents do not numerically correspond to the experimental values.

The extension of the EOS model to mixtures is carried out by means of traditional Berthelot–Lorentz quadratic mixing rules, according to which the cross parameters [15] are given as follows.

$$\varepsilon_{ij} = \sqrt{\varepsilon_i\varepsilon_j}(1 - k_{ij}) \quad (4)$$

$$\sigma_{ij} = \frac{1}{2}(\sigma_i + \sigma_j) \quad (5)$$

Constant binary interaction parameters k_{12} have been considered for the purpose of phase equilibrium calculations.

The coordinates of the GPD directly depend on the parameters of the EOS model used in its construction. Accordingly, for the purpose of this work, the coordinates of the GPD are given by the following definitions

$$\zeta = \frac{\sigma_2^3 - \sigma_1^3}{\sigma_2^3 + \sigma_1^3} \quad (6)$$

$$\lambda = \frac{(\varepsilon_2/\sigma_2^3) - (\varepsilon_1/\sigma_1^3)}{(\varepsilon_2/\sigma_2^3) + (\varepsilon_1/\sigma_1^3)} \quad (7)$$

$$\delta = \frac{(\varepsilon_2/\sigma_2^3) - 2((\varepsilon_{12}/\sigma_{12}^3) + (\varepsilon_1/\sigma_1^3))}{(\varepsilon_2/\sigma_2^3) + (\varepsilon_1/\sigma_1^3)} \quad (8)$$

As follows from Eqs. (6) to (8), GPD coordinates are directly linked to structural and molecular forces of the constituents of a binary mixture. In particular, ζ and λ parameters account for size and cohesion energy differences between mixture's constituents, respectively, while δ is a measure of the synergy between non-equal molecules. According to what can be observed in conventional GPDs

Table 3
PC-SAFT pure-component parameters: correlation constants for linear hydrocarbons in Eqs. (1)–(3).

j	Units	0	1	2
q_{j1}	Å	3.70390	−0.32260	0.69070
q_{j2}	mol g^{-1}	0.06233	−0.02236	−0.01563
q_{j3}	K	150.030	80.6800	38.9600

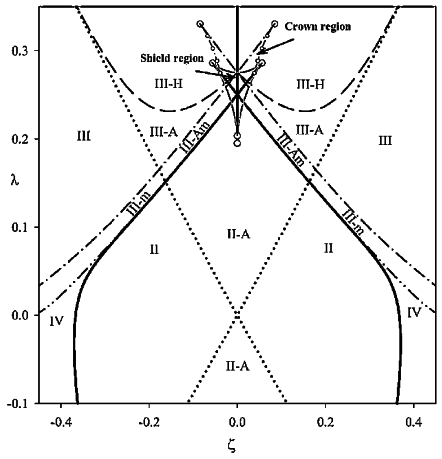

Fig. 3. GPD of a PC-SAFT binary fluid composed by chain like molecules of equal number of segments (m = 2.0729). (▬) TC, (– – –) DCEP, (– · –) CPSP, (· · ·) CAzeP, (– · –) III-A to III-H boundary, (') transitional end points constrained by stability considerations, and (▬O▬) stationary critical pressure end point (SCPEP).

- molecules of the same type characterized by null synergy correspond to the (0, 0, 0) coordinate, i.e. the origin of a GPD, and may be regarded as quasi-ideal systems,
- molecules of similar size and critical properties tend to originate Type I–Type II phase behaviors, and
- larger differences in molecular properties tend to originate high temperature liquid phase immiscibility, thus giving place to Type III, IV and V phase behaviors.

In addition, the phase behavior of a binary mixture with fixed critical properties (case in which ζ constant) depends on the mixing synergy which, in turn, is directly reflected by the sign of k_{12} or, equivalently, by the sign of ζ. Consequently, when $\zeta < 0$, attraction forces dominate and, depending on the molecular differences, total miscibility of components is promoted in the dense phase. In the opposite case ($\zeta > 0$), repulsion forces characterize the interactions between unlike molecules and liquid phase immiscibility is observed at high temperature, thus yielding discontinuity of the gas–liquid critical line that joins the critical points of pure components, even for mixtures composed by similar species.

Fig. 3 depicts the GPD of PC-SAFT binary fluids composed by chain-like molecules of equivalent number of segments (m = 2.0729), where the quoted segments correspond to bonded spheres of equivalent diameter. The parametrical lines related to the main transitional mechanisms such as the tricritical point (TC), double critical end point (DCEP), critical pressure step point (CPSP), and critical azeotropic end point (CAzEP), have been calculated according to the procedures suggested by Boshkov [16], Kraska [17,18], Deiters [11] and Segura [19]. Characteristic regions of more complex phase behavior such as shield [20] and crown [21] regions are also observed. However, in contrast to the vdW equation [2] and related models [22], no zero temperature transitions are predicted for PC-SAFT fluids.

The GPD reported in Fig. 3, which has been calculated for the first time for PC-SAFT fluids in this work, is useful for unequivocally establishing the Types predicted by the model and, additionally, for

comparing its prediction capability with other EOS models. In the quoted GPD it is possible to observe the set of transitional lines typically displayed by every physically coherent EOS model. This latter result is important for validating the physical reliability of the phase behavior predicted by PC-SAFT since, as pointed out by Segura et al. [23], Yelash et al. [24], Yelash et al. [25] and Privat et al. [26]; SAFT type EOSs may exhibit abnormal mechanical critical points, thus affecting the prediction of thermo-physical properties and phase equilibria of pure fluids and mixtures. Accordingly, appropriate precautions were taken in this work for predicting phase equilibrium, barotropic states and transitional lines inside the physical ranges of fluid densities and temperatures, in order to avoid the influence of unphysical critical points on results. The usefulness of Fig. 3 for performing a transitional analysis of homologous series of asymmetric mixtures like CO_2 + n-C_nH_{2n+2} is limited since the effect of the number of segments m has not been taken into account yet in the definitions given in Eqs. (6)–(8). Consequently, it is expedient to use an alternative GPD representation like the serial prediction domain-GPD (spd-GPD) introduced by Bidart et al. [12]. Analyzing the degrees of freedom of Eqs. (1)–(8) allows one to conclude that the global coordinates for the CO_2 + n-C_nH_{2n+2} series depend on the molar mass, M_w, and on the interaction parameter, k_{12}. The spd-GPD for the quoted series is presented and discussed in-depth in the section that follows.

3. Density inversions and their limiting conditions in asymmetric binary systems

In this section we describe how density inversions are affected and constrained by specific features related to the phase equilibrium behavior of asymmetric mixtures. For that purpose, we will first consider the global phase behavior that the PC-SAFT model predicts for the CO_2 (1) + n-$C_{16}H_{34}$ (2) mixture, case in which mass barotropic inversion has been experimentally detected and confirmed [27]. In addition, the constituents of the quoted system present a significant difference between the values of their molecular weights (M_{w1} = 44.01, M_{w2} = 226.45), thus constituting an appropriate example of asymmetric mixture. The specific features observed in this base case will be then extended to the set of members of the CO_2 + n-C_nH_{2n+2} series which – reportedly – are close to the transition from non-barotropic to barotropic behavior. Following recommendations of García et al. [28], k_{12} has been set to 0.12 for the purpose of predicting the phase behavior of CO_2 + hydrocarbon mixtures.

Fig. 4a depicts the P–T projection of the system CO_2 (1) + n-$C_{16}H_{34}$ (2), where we can observe the characteristic behavior of a Type III-m mixture. Particularly, the mixture exhibits a liquid–liquid–gas (LLG) immiscibility line which begins at low temperature and then evolves up to a intersection point with the branch of the critical line connecting the lighter component 1 (CO_2) in an upper critical end point (UCEP). As temperature decreases, the critical branch connecting the heavier component 2 (n-$C_{16}H_{34}$) develops two pressure stationary points and, then, it diverges to the high pressure range. In Fig. 4a, mass isopycnicity between fluid phases is observed along the MaDI line A–B, whose coordinates have been calculated according to the following relationships:

$$\mu_i^{\alpha}(x_1^{\alpha}, \tilde{v}^{\alpha}, T) = \mu_i^{\beta}(x_1^{\beta}, \tilde{v}^{\beta}, T) \tag{9}$$

$$A_v^{\alpha}(x_1^{\alpha}, \tilde{v}^{\alpha}, T) = A_v^{\beta}(x_1^{\beta}, \tilde{v}^{\beta}, T) \tag{10}$$

$$\frac{\tilde{v}^{\alpha}}{\tilde{v}^{\beta}} = \frac{M_w^{\alpha}}{M_w^{\beta}} = \frac{x_1^{\alpha}(M_{w1} - M_{w2}) + M_{w2}}{x_1^{\beta}(M_{w1} - M_{w2}) + M_{w2}} \tag{11}$$

In Eqs. (9)–(11) μ is the chemical potential, x the mole fraction, $\tilde{v}$ the molar volume while A corresponds to the Helmholtz energy function of the coexisting α and β phases. Fig. 4a also shows the P–T coordinates of molar isopycnicity along the MoDI line C–D, which has been calculated from the following relationships

$$\mu_i^{\alpha}(x_1^{\alpha}, \tilde{v}^{\alpha}, T) = \mu_i^{\beta}(x_1^{\beta}, \tilde{v}^{\beta}, T) \tag{12}$$

$$A_v^{\alpha}(x_1^{\alpha}, \tilde{v}^{\alpha}, T) = A_v^{\beta}(x_1^{\beta}, \tilde{v}^{\beta}, T) \tag{13}$$

$$\tilde{v}^{\alpha} = \tilde{v}^{\beta} \tag{14}$$

In the pressure–density projections presented in Fig. 4b and c we can see in detail how MaDI and MoDI lines, respectively, meet the mixture's critical line (indicated by points B and D in Fig. 4a–c). From these figures we deduce that mass and molar density inversions occur between two coexisting fluid phases which become indistinguishable as the critical point is approached. It is interesting to note that critical mass and molar density inversion points (here called CMaDIP and CMoDIP, respectively), present different thermo-mechanical coordinates. Particularly, the CMaDIP (shown by point B in Fig. 4a and b) occurs in the vicinity of the critical temperature of CO_2, and its state may be numerically approximated by simultaneously solving Eqs. (9)–(11) up to the critical collapse. The CMoDIP (shown by point D in Fig. 4a and c) occurs at larger temperature and pressure and, as established by Quiñones-Cisneros, it can be directly tracked along the critical line by analyzing the eigenvector's components associated to the nil eigenvalue of the Helmholtz energy matrix.

Finally, the details of connectivity of the LLG line with the MaDI and MoDI lines are shown in Fig. 4d and e. Particularly, Fig. 4d depicts the detail of Fig. 4a in the vicinity of the LLG line at the P–T projection. Fig. 4e, in turn, shows the evolution of mass and molar densities for the phases that coexist along the LLG line. From Fig. 4d we can conclude that, because of the promotion of a gas phase, density inversions between dense fluid phases are interrupted by global stability in the low pressure range. In fact, as it can be seen in Fig. 4e, two immiscible liquid phases (L_1 and L_2) having equivalent mass density equilibrate a third gas phase G, thus constraining the global stability of the MaDI line at a sub-critical mass density inversion end point (MaDIEP). Molar density inversions at the LLG line presents a similar pattern, although (in this particular case) the sub-critical molar density inversion end point (MoDIEP) appears at higher temperature, in the immediate proximity of the UCEP. MaDIEPs (or MoDIEPs) can be calculated by simultaneously solving Eqs. (9)–(11) (or Eqs. (12)–(14)) together with the equations that define phase equilibrium with a third phase:

$$\mu_i^{\alpha}(x_1^{\alpha}, \tilde{v}^{\alpha}, T) = \mu_i^{G}(x_1^{G}, \tilde{v}^{G}, T) \tag{15}$$

$$A_v^{\alpha}(x_1^{\alpha}, \tilde{v}^{\alpha}, T) = A_v^{G}(x_1^{G}, \tilde{v}^{G}, T) \tag{16}$$

Inspection of Fig. 4 allows one to conclude that, as pressure and temperature increase, the states where density inversions occur for the system CO_2 + $C_{16}H_{34}$ are clearly constrained by three phase lines and critical states.

However, considering that the PC-SAFT model overpredicts the critical pressure and temperature of pure species [14], we can expect an inaccurate prediction of the coordinates of the critical line and, therefore, of the related quasi-critical phase equilibrium states. Consequently, at this point it is interesting to test how model accuracy may affect the reliability of the density inversions predicted from the PC-SAFT model in quasi-critical conditions. For this latter purpose, we have considered the accurate RK-PR model [29] with parameters specifically specialized for correlating CO_2 + nC_nH_{2n+2} mixtures, starting with tetradecane. Fig. 4f depicts the prediction of the RK-PR model for the CO_2 + n$C_{16}H_{34}$, which fairly agrees with the results of PC-SAFT for the same mixture (previously shown in Fig. 4a), particularly:

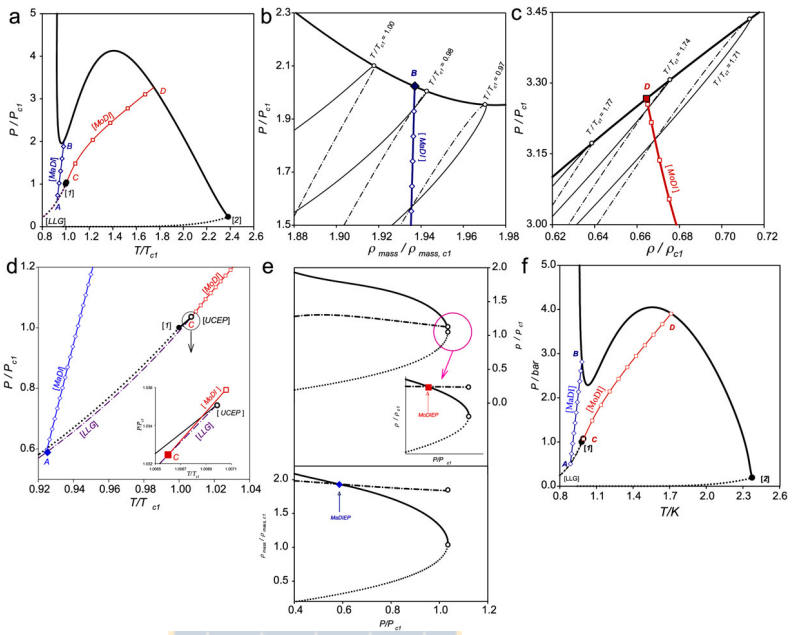

Fig. 4. (a) P–T projection for the binary system of $CO_2 + C_{16}H_{34}$ ($M_{w2} = 226.45$, $k_{12} = 0.12$). (●) Pure component critical point, (— ● —) three phase (or LLG) line, (···) pure component vapor pressure line, (▬) critical line, (—◇—) MaDI line, and (—□—) MoDI line. (b). P–ρ_{mass} envelopes in the vicinity of the MaDI line for the $CO_2 + C_{16}H_{34}$ system. (— ● —) Gas phase G, (—) liquid phase L, (▬) critical line, (—◇—) MaDI line, (◯) critical point, and (◆) critical mass density inversion point CMaDIP. (c) P–ρ envelopes in the vicinity of the MoDI line for the $CO_2 + C_{16}H_{34}$ system. (–·–) Liquid phase L, (—) gas phase G, (▬) critical line, (—□—) MoDI line, (◯) critical point, and (■) critical molar density inversion point CMoDIP. (d) Details of a showing barotropic activity in the vicinity of the LLG line. (●) Pure component critical point, (–·–) LLG line, (···) pure component vapor pressure line, (▬) critical line, (—◇—) MaDI line, (—□—) MoDI line, (◆) mass density inversion end point MaDIEP, and (■) molar density inversion end point MoDIEP. (e) P–ρ and P–ρ_{mass} projections for the phases present along the LLG line of $CO_2 + C_{16}H_{34}$. (▬) Liquid phase L_1, rich in CO_2, (–·–) liquid phase L_2, rich in hydrocarbon, (···) gas phase G, (◆) MaDIEP, and (■) MoDIEP. (f) P–T projection for the binary system of $CO_2 + C_{16}H_{34}$ as predicted from a specialized RK-PR [29] model. Captions as in (a).

- the MaDI line is constrained by a MaDIEP (point A) and a CMaDIP (point B), thus confirming the basic mechanisms that constraint a mass density inversion condition and
- at the right hand side of the MaDI line, the MoDI line begins at a MoDIEP (point C) and ends in a CMoDIP (point D) thus confirming also the basic mechanisms that define molar isopycnicity.

In general, from the point of view of the phase behavior, Fig. 4a and f are characterized by the same geometric features that give place to Type III-m behavior, although exhibiting slightly different thermo-mechanical coordinates. This latter qualitative agreement between PC-SAFT and RK-PR, from both the point of view of barotropy and phase equilibrium behavior, has been confirmed for $CO_2 + nC_nH_{2n+2}$ mixtures over the range $14 \le n \le 22$.

Finally, from Fig. 4 we can observe that the P–T coordinates of mass and molar density inversions are different, thus confirming the hypothesis claimed in Section 1 concerning the independence of mass and molar density inversions for the present series and, additionally, suggesting also a specific analysis of the constraining conditions for each case of inversion. In order to do so, and starting from the behavior of the CO_2 (1) + n-$C_{16}H_{34}$ (2) mixture as a base case, let us consider the effect of the alkane's chain length on the barotropic behavior of the complete CO_2 + n-C_nH_{2n+2} series (once again predicted by the PC-SAFT model with $k_{12} = 0.12$, as before). Fig. 5a shows how the temperature ranges of (mass and molar) density inversions are affected by the global phase behavior induced by the alkane's molecular weight M_{w2}. The figure also illustrates the barotropic behavior of the mixture CO_2 (1) + n-$C_{16}H_{34}$ (2), whose MaDI line develops between a MaDIEP and a CMaDIP (at points A and B, respectively) while its MoDI line begins at a MoDIEP in point C and ends in a CMoDIP (not shown in the scale of the figure).

The M_{w2} values for which TC, MDP and DCEP boundaries occur have been clearly identified along the II–IV–III transition observed in Fig. 5a. Particularly, TC transitions affect the continuity of the liquid–gas critical line that connects the critical points of the pure constituents, thus originating the characteristic Type II behavior for $M_{w2} < M_{w2,TC}$. Two stable LLG branches can be observed for mixtures with molecular weight inside the range $M_{w2,DCEP} > M_{w2} > M_{w2,TC}$: the first one appearing in low-temperature range, while the second one meets the high-temperature range at the liquid–gas critical line, as typically observed in Type IV mixtures. For the case in which $M_{w2} > M_{w2,DCEP}$ Type III behavior develops and a single LLG line is observed.

Detailed inspection of Fig. 5a reveals that, as M_{w2} decreases (or, equivalently, as the molecular chain length of the alkane reduces),

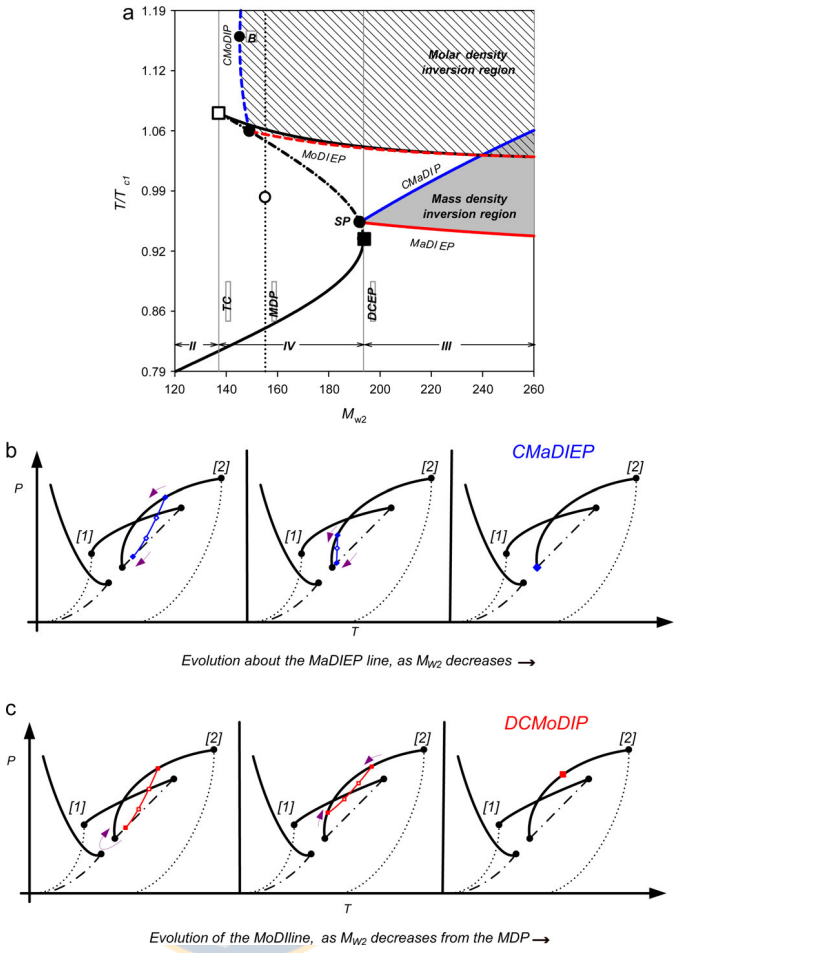

Fig. 5. (a) MaDI and MoDI temperature ranges for different M_{w2} values. Global phase behavior as predicted from PC-SAFT for the CO_2 + n-alkane series with k_{12} = 0.12. (▬) UCEP locus, (– · –) LCEP locus, (□) tricritical point TC, (■) double critical end point DCEP, and (○) mathematical double point MDP. (b) Schematic mechanism showing the evolution of the MaDI line in Type IV systems as M_{w2} decreases along the MaDIEP line in (a). (c) Schematic mechanism showing the evolution of the MoDI line in Type IV systems as M_{w2} decreases from the MDP in (a).

the temperature ranges where both mass and molar barotropy occur become narrower, until they virtually disappear in points where the pertinent density inversion lines shrink to the zero length. In fact, in the figure we can observe that:

- the MaDI line disappears in point SP at the LCEP of a Type IV system, where it is observed that the MaDIEP and CMaDIP intersect. Accordingly, point SP corresponds to a condition where a critical phase characterized by mass barotropy meets equilibrium with an additional sub-critical phase. In this work, such a limiting behavior for mass barotropy has been termed as CMaDIEP (critical mass density inversion end point) and the pertinent mechanism is schematically shown in Fig. 5b and
- the MoDI line disappears in point B along the critical branch of a Type IV system where, contrary to the case of MaDIs, no connectivity of the inversion point to a LLG equilibrium state can be observed. In this work, such a limiting behavior for molar barotropy has been termed as DCMoDIP (double critical molar density inversion point) and the pertinent mechanism is schematically shown in Fig. 5c.

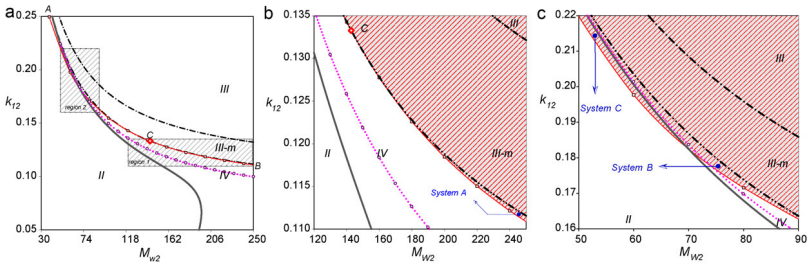

Fig. 6. (a) spd-GPD for the CO_2 + n-alkane series. (▬) TC line, (– ·· –) DCEP line, (●–●) CMaDIEP line, (– · –) CPSP line, and (●●●○●●●) MDP line. (b) Details of region 1 in (a). (c) Details of region 2 in (a).

All the evidence showed so far points to the fact that the persistence of mass and molar density inversions may be governed by different and independent physical conditions. Certainly, the present analysis sheds insight about how barotropic behavior may be controlled by the n-alkane chain in asymmetric mixtures. Quiñones-Cisneros [9] argues that, under high pressure, it is possible to find a dense phase (such as L_1 in Fig. 4e) which, being composed by lower weight and higher symmetry molecules, allows a larger number of molecules per unit volume than a dense phase L_2 rich in heavier asymmetric molecules. Consequently, and as it has been observed in the series under consideration, the molar mass of asymmetric molecules seems to have a dominant impact in the relative position of the phases.

The overall trend of the barotropic behavior shown in Fig. 5a is similar to that reported by Bidart et al. [12] for the alternative series of water + hydrocarbon mixtures. However, the barotropic phases that characterize this latter series are organized in a different way, thus suggesting some degree of sensitivity to the chemical nature of the solvents. In fact, for the case of H_2O + n-C_nH_{2n+2} series, mass barotropy is constrained by an equilibrium state where critical and non-critical phases coexist with equal mass densities (no limiting CMaDIP is observed in that case). Therefore, reducing chain length is not the most important variable for avoiding density inversions since, in the case quoted by Bidart et al., the interaction induced by association may change the molecular configuration. Thus, the number of molecules per volume not only depends on asymmetry, but also may be affected by anisotropic forces.

Constraining now our attention to the mass barotropy observed in CO_2 + n-C_nH_{2n+2}, we have clearly demonstrated that the CMaDIEP is a reasonable mechanism for delimiting mass density inversions of asymmetric mixtures. From a numerical viewpoint, the quoted mechanism may be approximated by solving the following set of equations

$$\phi_i(x_1', V', T) = \phi_i(x_1'', V'', T) = \phi_i^G(x_1^G, V^G, T) \quad (17a)$$

$$A_V(x_1', V', T) = A_V(x_1'', V'', T) = A_V^G(x_1^G, V^G, T) \quad (17b)$$

$$\frac{V'}{V''} = \frac{M_w'}{M_w''} = \frac{x_1'(M_{w1} - M_{w2}) + M_{w2}}{x_1''(M_{w1} - M_{w2}) + M_{w2}} \quad (17c)$$

$$|V' - V''| = \varepsilon \approx 0 \quad (17d)$$

Eqs. (17a) and (17b) establish the necessary conditions for finding three phases in equilibrium at isothermal conditions. The addition of Eq. (17c) implies a mass density inversion point for two of the three phases (normally, ′ and ″ liquid phases) that coexist along a three-phase line. Finally, Eq. (17d) expresses a numerical approximation of a critical point where ε is small distance that may be given by a fixed difference (ε = 0.1 cm^3 mol^{-1} for the purpose of this work).

From the viewpoint of the Gibbs' phase rule (and as it is shown by point A in Fig. 4d), Eqs. (17a)–(17c) define a unique point along the LLG line in the P–T projection of a given binary system (the so called MaDIEP). In addition, from Eqs. (1) to (3) it follows that the selection of CO_2 as component [1] together with the specification of the molecular weight M_{w2} of component [2] may be considered for the purpose of finding an interaction parameter k_{12} able to solve Eq. (17d). In this way, we can obtain a kind of GPD map showing the limiting conditions for mass barotropy in direct relation with the global phase behavior. Such a parametric map, also known as spd-GPD projection [12], is shown in Fig. 6 for the case of CO_2 + n-C_nH_{2n+2} series.

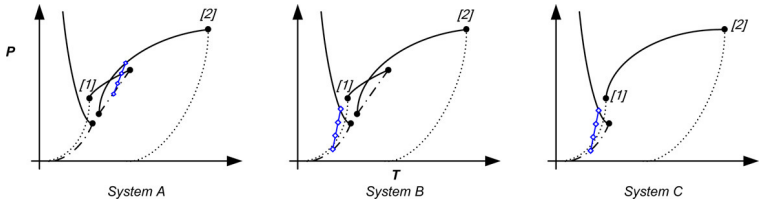

Fig. 7. Schematic P–T projections for the set of system indicated in Fig. 6b and c. (···) Pure component vapor pressure line, (– · –) LLG line, (▬) critical line, and (–◇–) MaDI line.

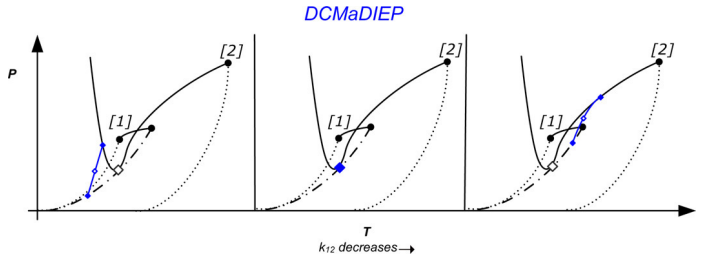

Fig. 8. Schematic P–T projections showing the evolution of the MaDI line about the vicinity of the DCMaDIEP. (···) Pure component vapor pressure line, (–·–) LLG line, (▬) critical line, (–◇–) MaDI line, (♦) DCEP, and (◆) DCMaDIEP.

Conveniently expressed in M_{w2}–k_{12} coordinates, Fig. 6a depicts the Types of behavior delimited by the most relevant global transitional mechanisms, as predicted by the PC-SAFT model. According to the results presented there, a mixture exhibits stable mass barotropy for every mixture with properties above line AB (the CMaDIEP line), which is almost indistinguishable from the DCEP line for low k_{12} values. In order to get a deeper insight of the phase behaviors predicted in microscopic regions of

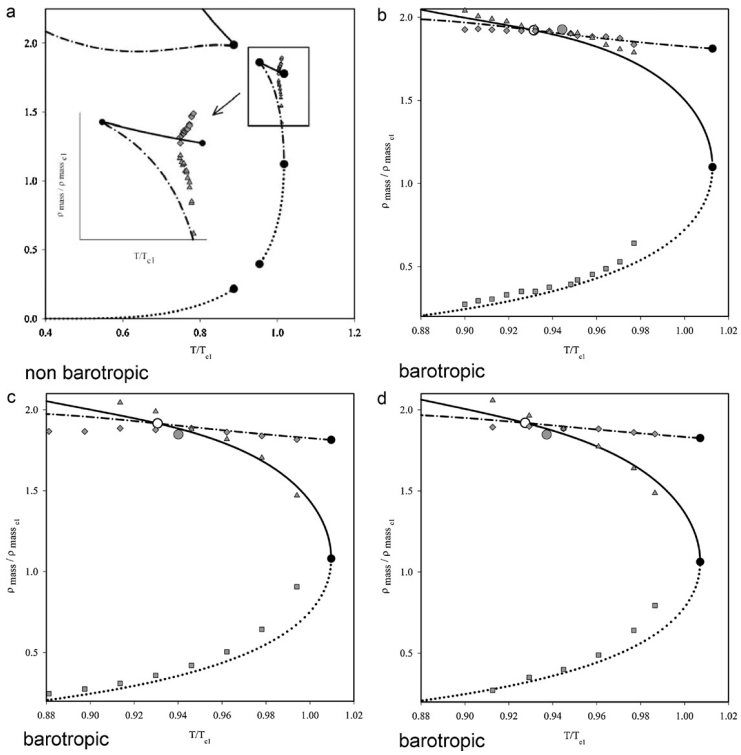

Fig. 9. T–$\mathbb{Z}_{mass}$ projections for the LLG line of the CO_2 + n-C_nH_{2n+2} series predicted by PC-SAFT with k_{12} = 0.12. (a) n = 13, (b) n = 14, (c) n = 15, and (d) n = 16. (▬) Liquid phase L_1, rich in CO_2, (–·–) liquid phase L_2, rich in hydrocarbon, (···) gas phase, G, (○) predicted barotropic point, (●) predicted CEP, (⬤) experimental barotropic point, (▲) experimental mass density for L_1, (♦) experimental mass density for L_2. (□) Experimental density for the gas phase. Experimental data taken from [27,33,34].

Fig. 6a–c present a detailed view of the dashed regions 1 and 2, respectively.

Particularly, in Fig. 6b and c, mass barotropy is present for every system with global coordinates picked from the dashed/shaded regions. As shown in Fig. 6a, PC-SAFT predicts mass barotropy mainly for Type III and IV systems, a result that is in excellent agreement with the experimental facts reported for CO_2 + n-C_nH_{2n+2} mixtures [25]. In addition, and as it is clearly shown in Fig. 6c for a microscopic range of the spd-GPD, mass barotropy also affects Type II systems, a result that – to best of our knowledge – had not been previously reported in the literature. The barotropic behavior that affects Type II systems seems to be mainly governed by the synergy observed between unlike molecules, as it can be deduced from the magnitude of k_{12}.

Since the TC, MDP and DCEP boundaries affect the topology of LLG lines, it is interesting to analyze how these transitional mechanisms might be reflected by specific patterns of the mass barotropy observed in the involved mixtures. For that purpose, Fig. 7 depicts the schematic *P*–*T* projections that can be drawn for the systems A, B and C indicated in Fig. 6b and c. From Fig. 7, the main characteristics of the systems exhibiting incipient mass barotropic behavior may be summarized as follows:

- system A classifies as a Type IV system, as expected from being drawn from a region bounded by the TC and DCEP transitions (see Fig. 6a). In addition, the quoted system shows a MaDI line that connects the upper branch of the LLG line with the gas-liquid critical line,
- system B, also taken from a region bounded by the TC and DCEP transitions (see Fig. 6b), corresponds to a Type IV system. However, in this case we can see that the MaDI line connects the lower branch of the LLG line with the gas–liquid critical line,
- system C has been taken from region that is below the TC line, thus confirming the existence Type II barotropic systems showing a sharp MaDI line connecting the LLG line with the gas–liquid critical line, and
- from Fig. 7, particularly from the results obtained for systems A and B, it is interesting to note that the MaDIEP of Type IV systems may appear either at the lower or the upper branches of the LLG line. A detailed inspection of Fig. 6b and c reveals that the CMaDIEP line is always below the DCEP line, exception being point C where the lines representing both mechanisms become tangent. In this latter case we can observe that there is a particular DCEP behavior where the critical phases are characterized by mass barotropy. Such a mechanism, which is schematically shown in Fig. 8, clearly explains the shift of the CMaDIEP between the LLG branches of Type IV systems by means of a double critical mass density inversion end point (DCMaDIEP).

Finally, in Fig. 6c, we can observe that mass barotropy may appear at both sides of the MDP line. Consequently, and in contrast to the claim of Quiñones-Cisneros, we can deduce that MDP transitions do not seem to have a relevant role on mass barotropy.

Due to their industrial relevance, the phase and mass barotropic behaviors of CO_2 + n-C_nH_{2n+2} mixtures have been detailedly characterized [27,28,30–34] by means of phase equilibrium measurements. According to this available experimental evidence, the CO_2 + n-C_nH_{2n+2} series exhibit Type III behavior and mass barotropy is present for $n \geq 14$. These experimental facts are in excellent agreement with the results predicted by the PC-SAFT EOS in this work. Particularly, Fig. 6a demonstrates the ability of PC-SAFT for predicting both Type of phase behavior and mass barotropy over the range $13 \leq n \leq 16$. Fig. 9, in turn, shows the quantitative and qualitative performance of the model over the subcritical range. Despite of the fact that a constant $k_{12} = 0.12$ values has been used, a reliable characterization of the experimental phase equilibrium is clearly observed.

4. Concluding remarks

The impact of the molecular properties of mixture's constituents on barotropic phenomena has been explained in terms of a spd-GPD approach, as reliably predicted by the PC-SAFT model for the CO_2 + n-C_nH_{2n+2} series. A clear distinction has been made between mass and molar density inversions, from which we can conclude that the persistence of both phenomena is governed by different physical mechanisms and appear in different thermo-physical ranges. Accordingly, a limiting mechanism that constraints the stability of mass barotropic behavior (the so called CMaDIEP) has been developed and depicted together with conventional transitional mechanisms that appear in the quoted spd-GPD. The so developed limiting mechanism corresponds to a mass barotropic CEP which, on the one hand, explains the mechanism of the mass barotropy that affects the behavior of CO_2 + n-C_nH_{2n+2} mixtures and, on the other hand, allows defining ranges of molecular parameters and Types of behavior where mass barotropy unequivocally occurs. Results show that:

- an increase in molecular asymmetry promotes mass barotropy in real mixtures,
- in excellent agreement with experimentation for CO_2 + hydrocarbon mixtures, it has been demonstrated that mass barotropy is likely to occur mainly in Type III and IV systems,
- although discontinuous liquid–gas critical lines between pure components are usually observed in conventional systems exhibiting barotropy, the evidence presented in this work clearly shows that Type II systems may also exhibit density inversions, and
- Type II barotropic systems are observed under conditions in which the most important effect is a positive synergy of the mixing rather than molecular asymmetry.

Thus, besides the molecular asymmetry between constituents, strong repulsion forces between similar molecules may also give place to barotropic behavior. Finally, we can conclude that the DCEP mechanism combined with the barotropic limiting mechanism allows defining clear regions within the spd-GPD, where it is possible to find Type IV systems exhibiting barotropic points at different LLG branches.

List of symbols

A	Helmholtz energy
G	gas phase
k	Boltzmann constant, J/K
k_{ij}	interaction parameter
L	liquid phase
M_w	molar mass
m	segment number
n	carbon number
P	pressure
q	molecular weight ratio for the components of a binary mixture, $q = M_{w2}/M_{w1}$
T	temperature
v	volume

Greek

ε, ,	global phase diagram coordinates, defined in Eqs. (6)–(8)
	depth of pair potential
	segment diameter

	chemical potential
	molar volume difference, in this work = 0.1 $cm^3\ mol^{-1}$
	density

Subscripts

c	critical property
i,j	component index
mass	mass property
molar	molar property

Superscripts

α,β,G	phase index

Abbreviations

CAzEP	critical azeotropic end point
CEP	critical end point
CMaDIEP	critical mass density inversion end point
CMoDIEP	critical molar density inversion end point
CMaDIP	critical mass density inversion point
CMoDIP	critical molar density inversion point
CPSP	critical pressure step point
CSRK	Carnahan–Starling–Redlich–Kwong
DCMaDIEP	double critical mass density inversion end point
DCMoDIP	double critical molar density inversion point
DCEP	double critical end point
EOS	equation of state
GPD	global phase diagram
LCEP	lower critical end point
LLG	liquid–liquid–gas
MaDI	mass density inversion, or mass barotropic point, or mass isopycnicity
MDP	mathematical double point
MoDI	molar density inversion, or molar barotropic point, or molar isopycnicity
MaDIEP	mass density inversion end point
MoDIEP	molar density inversion end point
PC-SAFT	Perturbed Chain-Statistical Associated Fluid Theory
spd-GPD	serial prediction domain global phase diagram
TC	tricritical point
UCEP	upper critical end point
vdW	van der Waals

Acknowledgements

This work has been financed by Fondecyt Project No 1100938. M. Flores and C. Bidart acknowledge financial aid from Fondef (Project D07I1109) and CCTE-UDT, Chile. H. Segura expresses his gratitude to Prof Sergio Quiñones-Cisneros and to anonymous reviewer 2 for enlightening discussions and suggestions that, significantly, improved the technical quality of this contribution.

References

[1] G.M. Schneider, A.L. Scheidgen, D. Klante, Ind. Eng. Chem. Res. 39 (2000) 4476–4480.
[2] P.H. van Konynenburg, R.L. Scott, Philos. Trans. R. Soc. London, Ser. A 298 (1980) 495–540.
[3] A.A. Bolz, U.K. Deiters, C.J. Peters, T.W. De Loos, Pure Appl. Chem. 11 (1998) 2233–2257.
[4] J.A. Levelt Sengers, J. Phys.: Condens. Matter 21 (2009) 164222.
[5] E. Brunner, J. Chem. Thermodyn. 22 (1990) 335–353.
[6] E. Brunner, J. Chem. Thermodyn. 17 (1985) 871–885.
[7] S.E. Quiñones-Cisneros, J. García, Int. J. Refrig. 28 (2005) 714–724.
[8] S.E. Quiñones-Cisneros, Fluid Phase Equilibr. 134 (1997) 103–112.
[9] S.E. Quiñones-Cisneros, Phys. Chem. Chem. Phys. 6 (2004) 2307–2313.
[10] J. Gross, G. Sadowski, Ind. Eng. Chem. Res. 40 (2001) 1244–1260.
[11] U.K. Deiters, I.L. Pegg, J. Chem. Phys. 90 (1989) 6632–6641.
[12] C. Bidart, H. Segura, J. Wisniak, Ind. Eng. Chem. Res. 46 (2007) 947–954.
[13] S.J. Aparicio, Supercrit. Fluids 46 (2008) 10–20.
[14] M.E. Cismondi, A. Brignole, J. Mollerup, Fluid Phase Equilibr. 234 (2005) 108–121.
[15] C.P. Hicks, C.L. Young, Chem. Rev. 75 (1976) 119–173.
[16] L.Z. Boshkov, Ber. Bunsen-Ges. Phys. Chem. 96 (1992) 940–943.
[17] T. Kraska, U.K. Deiters, J. Chem. Phys. 96 (1992) 539–547.
[18] T. Kraska, Ber. Bunsen-Ges. Phys. Chem. 100 (1996) 1318–1327.
[19] H. Segura, J. Wisniak, P.G. Toledo, A. Mejía, Fluid Phase Equilibr. 166 (1999) 141–162.
[20] D. Furman, R.B. Griffiths, Phys. Rev. A 17 (1978) 1139–1148.
[21] M. Flores, H. Segura, M.J. Tardón, J. Wisniak, I. Polishuk, J. Supercrit. Fluids 48 (2009) 108–119.
[22] I. Polishuk, R. González, J.H. Vera, H. Segura, Phys. Chem. Chem. Phys. 6 (2004) 5189–5194.
[23] H. Segura, T. Kraska, A. Mejía, J. Wisniak, I. Polishuk, Ind. Eng. Chem. Res. 42 (2003) 5662–5673.
[24] L. Yelash, M. Müller, W. Paul, K. Binder, J. Chem. Phys. 123 (2005), 14908/1–14908/15.
[25] L. Yelash, M. Müller, W. Paul, K. Binder, Phys. Chem. Chem. Phys. 7 (2005) 3728–3732.
[26] R. Privat, R. Gani, J.-N. Jaubert, Fluid Phase Equilibr. 295 (2010) 76–92.
[27] J. van der Steen, Th. W. de Loos, J. de Swan Aarons, Fluid Phase Equilibr. 51 (1989) 353–367.
[28] J. García, L. Lugo, J. Fernández, Ind. Eng. Chem. Res. 43 (2004) 8345–8353.
[29] M. Cismondi, J.M. Mollerup, M.S. Zabaloy, J. Supercrit. Fluids 55 (2010) 671–681.
[30] G.M. Schneider, in: M.L. McGlashan (Ed.), Chemical Thermodynamics, Spec. Per. Rep., vol. 2, The Chemical Society, London, 1979.
[31] G.M. Schneider, in: E. Kiran, J.M.H. Levelt Sengers (Eds.), Supercritical Fluids—Fundamentals for Application, NATO ASI Series E: Applied Sciences, vol. 273, Kluwer Academic Publishers, Dordrecht, 1994, pp. 91–115.
[32] G.M. Schneider, C.B. Kautz, D. Tuma, in: E. Kiran, P.G. Debenedetti, C.J. Peters (Eds.), Supercritical Fluids—Fundamentals and Applications, NATO Science Series E: Applied Sciences, vol. 366, Kluwer Academic Publishers, Dordrecht, 2000, pp. 31–68.
[33] R. Enick, G.D. Holder, B.I. Morsi, Fluid Phase Equilibr. 22 (1985) 209–224.
[34] D.J. Fall, K.D. Luks, J. Chem. Eng. Data 30 (1985) 276–279.

CONCLUSIONES

- el modelo SAFT no predice sistemas *Tipo I* sino un híbrido (*Tipo I*^{h}) -a través del mecanismo ZPTL creado en esta tesis- que incorpora una región cerrada de inmiscibilidad a alta presión, en contraste con lo obtenido en la mayoría de las EOS cúbicas
- la región que abarca la línea transicional ZTPL es bastante reducida y queda acotada por ambas tricríticas. El modelo no predice, en éstas condiciones de $\xi = 0$, la existencia de sistemas *Tipo V*.
- tanto el mecanismo CPSP como el DCEP se extienden de manera indefinida hacia valores de λ negativos sin alcanzar la línea ZTPL, al menos en rangos de parámetros de interacción con significado físico
- dos nuevas regiones, bien definidas, asociadas a la actividad CPSP. Estas nuevas organizaciones de transiciones reciben el nombre de *región de la corona* y *región del cáliz*. De acuerdo a los resultados, la *región de la corona* está relacionada a sistemas con altas desviaciones positivas del comportamiento ideal, típicamente mezclas *Tipo III-H*. En cambio, la región del cáliz, está principalmente relacionada a *Tipo I* y *Tipo V*, en su defecto *Tipo I*^{h}, donde las mezclas muestran esencialmente desviaciones negativas del comportamiento ideal
- como era de esperar, para moléculas de distinto diámetro, una gran pérdida de la simetría del GPD ha ocurrido por efecto de la diferencia de tamaño molecular y aumento de la longitud de cadena molecular
- el corrimiento de las líneas CAzeP hacia altos valores negativos de ζgenera una amplia región de sistemas *Tipo IV* con características azeotrópicas. Todos estos aspectos sumados a incursiones adicionales dentro de este GPD, indican que el modelo SAFT predice una rica topología azeotrópica que incluye dobles azeótropos críticos y sistemas poliazeotrópicos, sólo por efectos de tamaño y forma molecular
- no se observa actividad CPSP en la rama izquierda del GPD, al menos para λ>0. La región de la corona se destruye parcialmente, a diferencia de la región del escudo que mantiene su conectividad, en tal sentido se puede

concluir que la actividad CPSP es más sensible a las diferencias de tamaño y forma molecular que la región predicha por Griffith (1978).

- el término cadena, presente en SAFT, estabiliza la transición tricrítica en un rango más amplio de parámetros globales. Esta condición favorece la existencia de sistemas que no presentan inmiscibilidad en el rango de propiedades de los componentes puros, permitiendo que una línea crítica común
- al incrementar la longitud de cadena del segundo componente, en un *spd-GPD*, aparece inmiscibilidad líquido-líquido de baja temperatura (*Tipo II*), para posteriormente avanzar a regiones de altas temperaturas, rompiendo los regímenes de miscibilidad, en el rango de propiedades de componentes puros, originando sistemas *Tipo IV* y *Tipo III*.
- estudiadas las mezclas binarias de hidrocarburos (CH_4+n-alcanos, hasta n-octano), desde un punto netamente predictivo, el modelo cumple con los Tipos experimentales. Una consideración adicional que se desprende del spd-GPD en cuestión, es la imposibilidad, para los elementos de la serie, de presentar conductas azeotrópicas en el rango de parámetros de interacción con respaldo experimental.
- estudiadas las mezclas binarias de dióxido de carbono con hidrocarburos (CO_2+n-alcanos, hasta n-eicosano), desde un punto predictivo, el modelo cumple con la mayoría de los Tipos experimentales, excepciones van desde el n-heptano hasta n-undecano, en los cuales experimentalmente se reporta *Tipo II*. Desde el n-tridecano en adelante, el modelo predice correctamente el comportamiento reportado experimentalmente, observándose principalmente sistemas que clasifican *Tipo III*.
- se ha desarrollado un mecanismo transicional para la barotropía (inversión de densidades másicas), llamado CMaDIEP, válido para sistemas no asociantes
- un incremento de la asimetría molecular promueve la barotropía en mezclas reales
- una excelente concordancia con lo observado experimentalmente, en cuanto a barotropía se obtiene para las mezclas de CO_2+n-hidrocarburos, donde ésta se encuentra principalmente en sistemas *Tipo III* y *Tipo IV*

- aun cuando una línea crítica líquido-gas discontinua entre componentes puros es observada convencionalmente en sistemas que presentan barotropía, la evidencia presentada en este trabajo, muestra sistemas *Tipo II*, que pueden también exhibir inversión de densidad
- Sistemas *Tipo II* barotrópicos, son observados bajo condiciones en las cuales el efecto más importante es la sinergia positiva
- en el caso de las mezclas de CO_2+n-alcanos el mecanismo DCEP combinado con el mecanismo límite barotrópico, define regiones dentro del spd-GPD, donde es posible encontrar sistemas *Tipo IV* con puntos barotrópicos en diferentes ramas LLG.

ANEXOS

Anexo I: Equilibrio de Fase y tensión interfacial en sistemas metil tert butil éter+ acetona+ciclohexano, metil tert butil éter+acetona y metil tert butil éter+ciclohexano

Artículo publicado en Fluid Phase Equilibria, 273 (2008) 68-77

Se determina el equilibrio de fases y la tensión interfacial experimentalmente, para la mezcla ternaria y sus binarias. Los tests de consistencia indican que la información obtenida es fidedigna. Los datos del ELV de la mezcla ternaria presentan desviación positiva de la idealidad y azeotropía para el binario metil tert butil éter+acetona. En el caso de la tensión interfacial, ésta muestra desviaciones negativas respecto del comportamiento lineal.

En el artículo que se adjunta, se puede revisar con mayor detalle el trabajo realizado

Fluid Phase Equilibria 273 (2008) 68–77

Contents lists available at ScienceDirect

Fluid Phase Equilibria

journal homepage: www.elsevier.com/locate/fluid

Phase equilibria and interfacial tensions in the systems methyl *tert*-butyl ether + acetone + cyclohexane, methyl *tert*-butyl ether + acetone and methyl *tert*-butyl ether + cyclohexane

Andrés Mejía*, Hugo Segura*, Marcela Cartes, Leslie Cifuentes, Mauricio Flores

Departamento de Ingeniería Química, Universidad de Concepción POB 160 – C, Correo 3, Concepción, Chile

ARTICLE INFO

Article history:
Received 19 May 2008
Received in revised form 21 August 2008
Accepted 25 August 2008
Available online 4 September 2008

Keywords:
Vapor–liquid equilibrium
Interfacial tension
Oxygenates
Model-free approach for data treatment

ABSTRACT

Isobaric vapor–liquid equilibrium (VLE) data have been measured for the ternary system methyl *tert*-butyl ether + acetone + cyclohexane, and for its methyl *tert*-butyl ether based binaries, at 94 kPa and in the temperature range 323–340 K. Equilibrium determinations were performed in a vapor–liquid equilibrium still with circulation of both phases. The dependence of interfacial tensions of these mixtures on concentration was also determined, at atmospheric pressure and 303.15 K, using the maximum bubble pressure technique.

From the experimental results, it follows that the investigated mixtures exhibit positive deviation from ideal behavior and azeotropy is present for the methyl *tert*-butyl ether + acetone system at 94 kPa. The application of a model-free approach allows concluding about the reliability of the present vapor–liquid equilibrium data for all the indicated mixtures. Furthermore, the determined interfacial tensions exhibit negative deviation from linear behavior for all the analyzed mixtures.

The vapor–liquid equilibrium data of the binary mixtures were well correlated using the NRTL, Wilson and UNIQUAC equations, while their interfacial tensions were smoothed using the Redlich–Kister equation. Scaling of these models to the ternary mixture allows concluding that both the VLE data and the interfacial tensions can be reasonably predicted from binary contributions.

1. Introduction

The experimental characterization of the phase and interface behavior of mixtures containing branched ethers (e.g. methyl *tert*-butyl ether or MTBE, ethyl *tert*-butyl ether or ETBE, *tert*-amyl methyl ether or TAME, 2,2′-oxybis[propane] or DIPE) is of fundamental importance for commercial gasoline blending and distribution [1,2]. On the one hand, phase equilibrium behavior is a clear indicator of the combustion evolution during the vaporization of fuels and, additionally, it allows estimating the Reid's vapor pressure (RVP), which is the widely accepted volatility indicator of fuels [1,2]. On the other hand, the interfacial tension of fuel droplets may be conveniently modified by adding new agents to fuels, so as to control the ignition kinetics and the atomization of fuels inside the engine's combustion chamber [3,4]. Furthermore, from an environmental protection viewpoint, interface tensions and phase equilibrium behavior (particularly, liquid phase miscibility) also play an important role in assessing risks related to the pollution of aquifers during gasoline distribution [5,6].

Despite of the practical relevance of both phase equilibrium and interface tensions in fuel processing and handling, experimental research has been mainly focused to the determination of phase equilibrium data only (vapor–liquid and liquid–liquid equilibrium), at several thermo-mechanic conditions (see, for instance: Marsh et al. [7], Chamorro et al. [8], and references therein). Thus, for the case of the system MTBE + cyclohexane, isothermal vapor–liquid equilibrium (VLE) data have been measured over the temperature range 298–333 K [9–11]. These isothermal data allow concluding that the mixture is not azeotropic, and exhibits moderate positive deviation from ideal behavior. For the case of the system MTBE + acetone, which is not directly related to gasoline production, Churkin et al. [12] reported isobaric VLE data at atmospheric pressure, while Gmehling and Bölts [13] characterized its azeotropic behavior over the range 302.65–324.35 K and 46.85–102.19 kPa. According to these experimental results, the MTBE + acetone system exhibits clear positive deviation from ideal behavior and azeotropy is present. Finally, the reported interface tension measurements are constrained to

* Corresponding authors. Tel.: +56 41 2203897; fax: +56 41 2247491.
E-mail addresses: amejia@udec.cl (A. Mejía), hsegura@udec.cl (H. Segura).

0378-3812/$ – see front matter © 2008 Elsevier B.V. All rights reserved.
doi:10.1016/j.fluid.2008.08.012

Table 1
GC purities (mass%), refractive index (n_D) at Na D line, densities ( ), normal boiling points (T_b) and interfacial tensions ( ) of pure components

Component (purity (mass%))	n_D (298.15 K)		(g cm^{-3}) (298.15 K)		T_b (K) (101.33 kPa)		(mN m^{-1}) (303.15 K)	
	Experimental	Literature[a]	Experimental	Literature[a]	Experimental	Literature[a]	Experimental	Literature[a]
MTBE (99.9+)	1.36766	1.36630	0.73545	0.73527	328.24	328.35	18.70	18.70
Acetone (99.9+)	1.35732	1.35600	0.78423	0.78658	329.33	329.44	22.45	22.42
Cyclohexane (99.9+)	1.42508	1.42235	0.77384	0.77314	353.82	353.87	24.10	24.04

[a] Daubert and Danner [18].

some few gasoline mixtures [14–17] and, to the best of our knowledge, no data have been reported for mixtures containing MTBE.

Following our ongoing research program on characterizing thermo-physical properties of fuels, this work is devoted to measure VLE data and interface tensions of systems constituted by gasoline components and potentially attractive additives. The ternary system MTBE + acetone + cyclohexane, for which no data have been reported previously, constitutes a clear example of this latter type of mixtures.

2. Experimental

2.1. Purity of materials

Acetone and cyclohexane were purchased from Merck, and were used without further purification. MTBE was purchased from Aldrich, and then was dried by percolation through dry calcium chloride in a bed column (50 cm height and 5 cm diameter). The properties and purity of the pure components, as determined by gas chromatography (GC), appear in Table 1. The densities and refractive indexes of pure liquids were measured at 298.15 K using an Anton Paar DMA 5000 densimeter (Austria) and a Multiscale Automatic Refractometer RFM 81 (Bellingham + Stanley, England), respectively. Temperature was controlled to ±0.01 K with a thermostated bath. The uncertainties in density and refractive index measurements are 5×10^{-6} g cm^{-3} and $\pm 10^{-5}$, respectively. The interfacial tensions of pure fluids were measured at 303.15 K using a maximum bubble pressure tensiometer, model PC500-LV (Sensadyne, USA). The uncertainties in interfacial tension measurements are ±0.1 mN m^{-1}. Temperature was controlled to ±0.1 K with a thermostated bath (Cole-Palmer, USA). The experimental values of these properties and the boiling points are given in Table 1 together with those given in the literature.

2.2. Apparatus and procedure

2.2.1. Vapor–liquid-equilibrium cell

An all-glass vapor–liquid-equilibrium apparatus model 601, manufactured by Fischer Labor und Verfahrenstechnik (Germany), was used in the equilibrium determinations. In this circulation-method apparatus, the mixture is heated to its boiling point by a 250 W immersion heater. The vapor–liquid mixture flows through an extended contact line (Cottrell pump) that guarantees an intense phase exchange and then enters a separation chamber whose construction prevents an entrainment of liquid particles into the vapor phase. The separated gas and liquid phases are condensed and returned to a mixing chamber, where they are stirred by a magnetic stirrer, and returned again to the immersion heater. The temperature in the VLE still is determined with a Systemteknik S1224 digital temperature meter, and a Pt 100 probe calibrated at the Swedish Statens Provningsanstält. The accuracy is estimated as ±0.02 K. The total pressure of the system is controlled by a vacuum pump capable of work under vacuum up to 0.25 kPa. The pressure is measured with a Fischer pressure transducer calibrated against an absolute mercury-in-glass manometer (22-mm diameter precision tubing with cathetometer reading), the overall accuracy is estimated as ±0.03 kPa.

On average the system reaches equilibrium conditions after 2–3 h of operation. 1.0 μL samples taken by syringe after the system

Table 2
Experimental VLE data for MTBE (1) + acetone (2) at 94.00 kPa

T (K)	x_1	y_1	φ_1	φ_2	$-B_{ij}$ (cm^3 mol^{-1})		
					11	22	12
327.16	0.000	0.000		1.000		1421	
325.69	0.057	0.100	1.809	1.003	1202	1406	802
324.72	0.109	0.173	1.692	1.008	1211	1421	809
323.99	0.159	0.233	1.594	1.016	1218	1432	813
323.39	0.210	0.286	1.510	1.028	1223	1441	817
322.91	0.260	0.333	1.438	1.043	1228	1449	820
322.54	0.313	0.377	1.367	1.064	1231	1455	823
322.22	0.363	0.416	1.313	1.088	1234	1460	825
322.07	0.413	0.453	1.260	1.114	1236	1462	826
321.93	0.464	0.489	1.214	1.146	1237	1465	827
321.87	0.514	0.523	1.175	1.182	1237	1466	827
321.86	0.561	0.556	1.142	1.221	1238	1466	827
321.91	0.613	0.592	1.110	1.273	1237	1465	827
322.03	0.662	0.628	1.084	1.328	1236	1463	826
322.25	0.716	0.669	1.060	1.396	1234	1460	825
322.52	0.764	0.709	1.042	1.467	1231	1455	823
322.94	0.815	0.755	1.025	1.557	1227	1449	820
323.51	0.867	0.809	1.012	1.656	1222	1440	816
324.10	0.908	0.858	1.005	1.756	1217	1430	813
324.82	0.953	0.921	1.004	1.855	1210	1419	808
325.98	1.000	1.000	1.000		1199		

Table 3
Experimental VLE data for MTBE (1) + cyclohexane (3) at 94.00 kPa

T (K)	x_1	y_1	φ_1	φ_3	$-B_{ij}$ (cm^3 mol^{-1})		
					11	33	13
351.37	0.000	0.000		1.000		1165	
348.91	0.046	0.118	1.296	0.996	1020	1186	1043
346.49	0.095	0.223	1.273	0.996	1037	1208	1061
344.43	0.143	0.309	1.248	0.996	1051	1227	1077
342.63	0.189	0.381	1.224	0.997	1065	1244	1091
341.01	0.235	0.446	1.205	0.997	1077	1260	1105
339.55	0.282	0.499	1.171	1.005	1088	1275	1117
338.15	0.330	0.552	1.151	1.010	1098	1289	1128
336.84	0.379	0.596	1.126	1.025	1109	1303	1140
335.69	0.427	0.638	1.106	1.034	1118	1315	1150
334.49	0.481	0.680	1.087	1.048	1127	1328	1160
333.44	0.529	0.718	1.076	1.056	1136	1339	1170
332.54	0.576	0.749	1.060	1.075	1143	1349	1178
331.58	0.629	0.784	1.045	1.093	1151	1360	1187
330.71	0.678	0.815	1.035	1.114	1158	1370	1195
329.92	0.726	0.843	1.026	1.136	1165	1379	1202
329.07	0.779	0.876	1.019	1.154	1172	1389	1210
328.29	0.832	0.905	1.010	1.190	1179	1398	1218
327.49	0.886	0.937	1.007	1.207	1186	1407	1225
326.76	0.940	0.967	1.003	1.229	1193	1416	1232
325.98	1.000	1.000	1.000		1199		

Table 4
Experimental VLE data for MTBE (1) + acetone (2) + cyclohexane (3) at 94.00 kPa

T (K)	x_1	x_2	y_1	y_2	Δ_1	Δ_2	Δ_3	$-B_{ij}$ (cm^3 mol^{-1})					
								11	22	33	12	13	23
324.09	0.073	0.833	0.100	0.777	1.485	1.036	3.266	1217	1430	1449	813	1259	755
340.29	0.093	0.031	0.174	0.202	1.210	4.381	1.004	1082	1208	1268	717	1110	674
324.04	0.096	0.600	0.103	0.665	1.151	1.235	1.901	1217	1431	1449	813	1260	755
323.83	0.100	0.802	0.131	0.748	1.436	1.046	3.087	1219	1435	1452	814	1262	756
323.71	0.102	0.708	0.119	0.700	1.274	1.112	2.415	1220	1436	1454	815	1263	757
325.20	0.103	0.404	0.105	0.609	1.054	1.620	1.380	1207	1413	1435	806	1248	749
326.35	0.104	0.303	0.109	0.573	1.046	1.959	1.220	1196	1396	1421	798	1237	743
324.27	0.105	0.533	0.109	0.642	1.108	1.334	1.695	1215	1428	1447	811	1257	754
325.23	0.107	0.402	0.109	0.605	1.053	1.615	1.383	1206	1413	1435	805	1248	749
332.96	0.114	0.095	0.159	0.385	1.129	3.403	1.037	1140	1302	1345	758	1174	709
328.57	0.116	0.189	0.134	0.501	1.074	2.551	1.104	1177	1363	1394	784	1215	731
323.69	0.141	0.806	0.190	0.741	1.483	1.035	3.291	1220	1437	1454	815	1263	757
323.16	0.193	0.707	0.229	0.668	1.322	1.084	2.650	1225	1445	1460	819	1269	760
323.37	0.194	0.606	0.209	0.627	1.185	1.181	2.087	1223	1442	1458	817	1267	759
324.56	0.198	0.410	0.197	0.566	1.055	1.515	1.467	1212	1423	1443	810	1254	752
323.52	0.199	0.559	0.208	0.609	1.145	1.239	1.906	1222	1439	1456	816	1265	758
325.68	0.201	0.307	0.204	0.525	1.035	1.809	1.284	1202	1406	1429	802	1243	746
323.83	0.202	0.503	0.205	0.591	1.106	1.321	1.723	1219	1435	1452	814	1262	756
327.81	0.202	0.194	0.223	0.456	1.051	2.329	1.143	1183	1374	1403	789	1222	735
331.72	0.213	0.095	0.279	0.332	1.095	3.062	1.056	1150	1319	1358	765	1185	715
322.76	0.287	0.611	0.314	0.596	1.228	1.138	2.304	1229	1451	1466	821	1273	762
323.93	0.290	0.414	0.286	0.527	1.063	1.432	1.566	1218	1433	1451	814	1261	756
327.00	0.292	0.198	0.310	0.418	1.034	2.146	1.181	1191	1386	1413	794	1230	739
323.17	0.293	0.512	0.299	0.558	1.127	1.256	1.876	1225	1445	1460	819	1269	760
334.17	0.294	0.045	0.419	0.182	1.105	3.278	1.042	1130	1286	1331	751	1163	703
325.07	0.296	0.307	0.294	0.480	1.030	1.695	1.351	1208	1415	1437	806	1249	750
330.81	0.310	0.090	0.384	0.280	1.067	2.801	1.083	1158	1331	1369	771	1194	720
323.27	0.381	0.418	0.373	0.494	1.078	1.359	1.678	1224	1443	1459	818	1268	759
326.16	0.384	0.203	0.394	0.383	1.023	1.978	1.234	1198	1399	1423	799	1238	744
322.54	0.385	0.514	0.395	0.527	1.157	1.208	2.027	1231	1455	1468	823	1275	764
324.36	0.393	0.308	0.382	0.443	1.033	1.597	1.422	1214	1426	1445	811	1256	754
329.51	0.409	0.090	0.478	0.247	1.047	2.585	1.110	1169	1350	1384	779	1206	726
322.57	0.478	0.420	0.467	0.462	1.100	1.297	1.809	1231	1454	1468	823	1275	763
325.28	0.483	0.207	0.479	0.349	1.017	1.821	1.305	1206	1412	1434	805	1247	749
323.63	0.486	0.312	0.466	0.412	1.041	1.505	1.509	1221	1438	1455	816	1264	758
330.40	0.498	0.051	0.595	0.145	1.041	2.593	1.128	1161	1337	1373	773	1198	722
328.22	0.509	0.094	0.561	0.222	1.028	2.339	1.155	1180	1368	1399	787	1218	733
324.40	0.583	0.210	0.561	0.321	1.018	1.700	1.376	1214	1426	1445	811	1256	753
322.89	0.587	0.310	0.555	0.380	1.052	1.435	1.594	1228	1449	1464	820	1272	762
327.18	0.605	0.094	0.638	0.198	1.015	2.157	1.198	1189	1384	1411	793	1228	738
323.52	0.683	0.214	0.644	0.296	1.024	1.590	1.459	1222	1439	1456	816	1265	758
327.66	0.694	0.054	0.742	0.118	1.013	2.212	1.200	1185	1377	1405	790	1224	736
326.10	0.699	0.096	0.706	0.181	1.007	2.000	1.250	1199	1400	1424	800	1239	744
325.04	0.795	0.098	0.775	0.166	1.005	1.860	1.310	1208	1416	1437	807	1250	750
325.33	0.887	0.056	0.871	0.098	1.003	1.917	1.291	1205	1411	1433	805	1247	748

had achieved equilibrium, were analyzed by gas chromatography on a Varian 3400 apparatus provided with a thermal conductivity detector and a Thermo Separation Products model SP4400 electronic integrator. The column was 3 m long and 0.3 cm in diameter, packed with SE-30. Column, injector and detector temperatures were 343.15, 423.15, and 493.15 K, respectively. Good separation was achieved under these conditions, and calibration analyses were carried out to convert the peak area ratio to the mass composition of the sample. The pertinent polynomial fit of the calibration data had a correlation coefficient R^2 better than 0.99. At least three analyses were made of each sample. Concentration measurements were accurate to better than ±0.001 in mole fraction.

2.2.2. Interfacial tension measurements

A maximum bubble pressure tensiometer model PC500-LV manufactured by Sensadyne Inc. (USA), was used in interfacial tension measurements. In this equipment, two probes of different orifice radii (r_1, r_2) are immersed in a vessel that contains the liquid sample to be measured. Then an inert gas, (e.g. nitrogen) is blown through the probes and the differential pressure (P) between them is recorded. According to the Laplace's equation, P and r_1, r_2 are related to the interfacial tension, , as:

$$P = P_1 - P_2 = 2 \left(\frac{1}{r_1} - \frac{1}{r_2}\right) \quad (1)$$

where P_i is the pressure exerted by the gas flow in the probe of radius r_i. The gas flow is controlled by a sensor unit connected to a personal computer through an interface board (PCI-DAS08, Measurement Computing, USA). Besides a constant volume flow controller, this sensor unit contains a differential pressure transducer, a temperature transducer and pressure regulator. The temperature of the sample in the vessel is measured by means of a K-type thermocouple, and maintained constant to within ±0.1 K using a thermostatic bath (Cole-Parmer, USA).

The experimental procedure for determining interfacial tension is as follows. The mixture to be analyzed is prepared by adding appropriate volumes of each pure fluid, then the concentration of the sample is measured by GC. The sample is then placed into the vessel and heated to the experimental temperature. Thereafter, an inert gas flows through the probes and the sensor unit translates the voltage signal (v) to a P signal. The relation between v and P is obtained by calibrating the sensor unit using two reference fluids of well-known interfacial tensions (e.g. water and ethanol, respec-

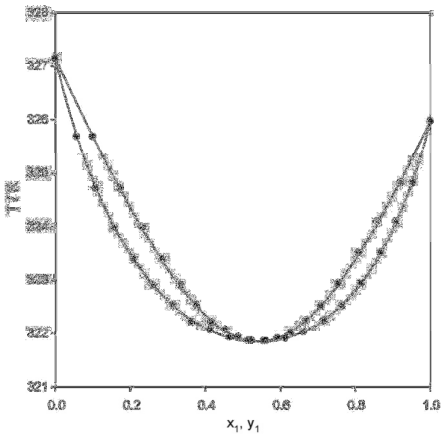

Fig. 1. Experimental VLE data for the binary system MTBE (1) + acetone (2) at 94.00 kPa: (●), experimental data determined in this work; (—), smoothed from a model-free data treatment for binary systems and the parameters presented in Table 8.

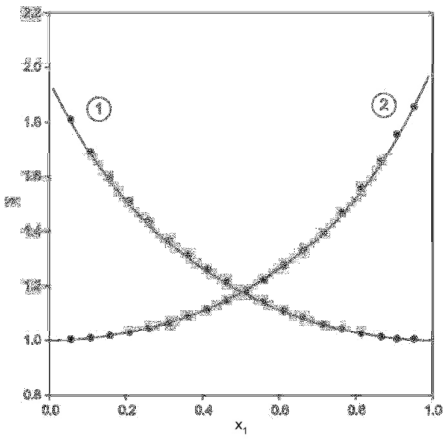

Fig. 2. Activity coefficient plot for the binary system MTBE (1) + acetone (2) at 94.00 kPa: (●), experimental data determined in this work; (—), smoothed from a model-free data treatment for binary systems and the parameters presented in Table 8.

tively). Finally, the interfacial tension is calculated according to Eq. (1). Additional details concerning to the maximum bubble pressure technique have been extensively described by Adamson and Gast [19] and Rusanov and Prokhorov [20].

3. Results and discussions

3.1. Vapor–liquid equilibrium

The equilibrium temperature T, liquid-phase x and vapor-phase y mole fraction measurements at $P = 94$ kPa are reported in Tables 2–4 and Figs. 1–5 together with the activity coefficients (γ_i) that were calculated from the following equation [21]:

$$\ln \gamma_i = \ln \frac{y_i P}{x_i P_i^0} + \frac{(B_{ii} - V_i^L)(P - P_i^0)}{RT} + \frac{P}{2RT} \sum_{j=1}^{3} \sum_{k=1}^{3} y_j y_k (2\delta_{ji} - \delta_{jk}) \quad (2)$$

where P is the total pressure and P_i^0 is the pure component vapor pressure. V_i^L is the liquid molar volume of component i, B_{ii} and B_{jj} are the second virial coefficients of the pure gases, B_{ij} is the cross second virial coefficient, and

$$\delta_{ij} = 2B_{ij} - B_{jj} - B_{ii} \quad (3)$$

According to Eq. (2), the standard state for calculating activity coefficients is the pure component at the pressure and temperature of the solution. Eq. (2) is valid from low to moderate pressures, where the virial equation of state truncated after the second term is adequate for describing the vapor phase of the pure components and their mixtures and, additionally, the liquid molar volumes of pure components are incompressible over the pressure range under consideration. Liquid molar volumes were estimated from the correlation proposed by Rackett [22]. Critical properties were taken from Daubert and Danner [18]. The molar virial coefficients B_{ii}, B_{jj} and B_{ij} were estimated by the method of Hayden and O'Connell [23] using the molecular and solvation parameters suggested by Prausnitz et al. [24] for the case of acetone and cyclohexane. For the case of MTBE, molecular parameters and physical properties were also taken from ref. [18] while the solvation parameter was estimated by smoothing experimental data of second virial coefficients, thus yielding the value $\eta = 0.078$. B_{ii}, B_{jj} and B_{ij} values are reported in Tables 2–4.

The vapor pressure of the pure components was determined experimentally as a function of temperature using the same equip-

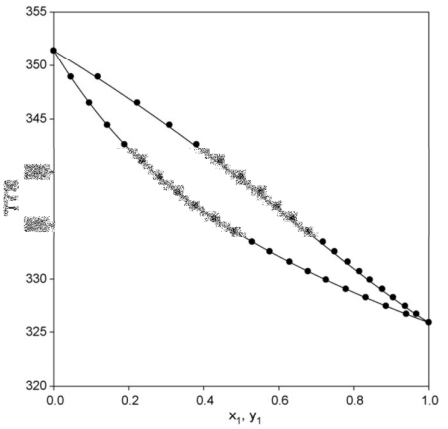

Fig. 3. Experimental VLE data for the binary system MTBE (1) + cyclohexane (3) at 94.00 kPa: (●), experimental data determined in this work; (—), smoothed from a model-free data treatment for binary systems and the parameters presented in Table 8.

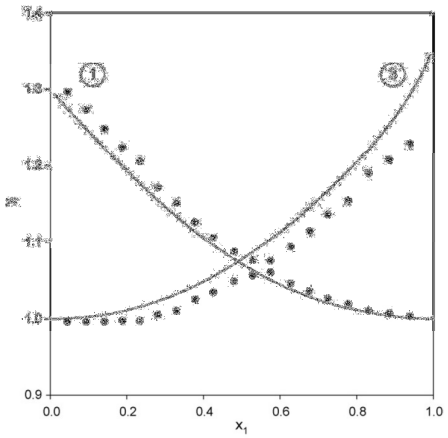

Fig. 4. Activity coefficient plot for the binary system MTBE (1) + cyclohexane (3) at 94.00 kPa: (●), experimental data determined in this work; (—), smoothed from the model-free data treatment for binary systems and the parameters presented in Table 8.

ment as that for obtaining the VLE data. The experimental values for acetone and cyclohexane have been previously reported elsewhere [17], while Table 5 presents the experimental values obtained for MTBE. The temperature dependence of the vapor pressure P_i^0 was correlated using the Antoine equation:

$$\log(P_i^0\,\{\text{kPa}\}) = A_i - \frac{B_i}{\{T\,\{\text{K}\}\} + C_i} \quad (4)$$

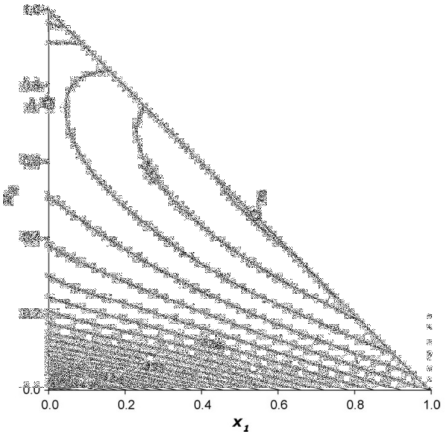

Fig. 5. Isotherms for the ternary system MTBE (1) + acetone (1) + cyclohexane (3) at 94.00 kPa: (—), smoothed with Eq. (5) and the coefficients given in Table 8.

Table 5
Experimental vapor pressure for MTBE

T (K)	p (kPa)
301.31	38.06
303.21	41.03
305.59	45.05
308.33	50.06
310.85	55.05
313.20	60.06
315.39	65.03
317.47	70.07
319.41	75.05
321.27	80.08
323.02	85.05
324.70	90.06
326.31	95.05
328.24	101.34

Table 6
Antoine coefficients, Eq. (4)

Compound	A_i	B_i	C_i	Temperature range (K)
MTBE	6.12370	1184.1727	−40.674	301.31–328.24
Acetone[a]	6.23239	1205.6491	−44.086	297.65–329.33
Cyclohexane[a]	6.52350	1543.1076	−12.254	302.91–354.06

[a] Parameters have been taken from ref. [17].

where the Antoine constants A_i, B_i, and C_i are reported in Table 6. Eq. (4) correlated the vapor pressure data of MTBE with an absolute percentage deviation (ADP) of 0.10%. Fig. 6 shows a comparison between the vapor pressure predicted from Eq. (4) with the parameters presented in Table 6 and the experimental data reported by Ambrose et al. [25]. From this figure it is possible to conclude about the reliability of the parameters presented in Table 6, since they predict very well the values reported by Ambrose et al., with an absolute percentage deviation of 0.10%.

The activity coefficients presented in Tables 2 and 4 are estimated accurate to within ±3%. The experimental data reported in these tables allow concluding that the binary mixtures exhibit positive deviation from ideal behavior and azeotropy is confirmed for the MTBE (1) + acetone (2) binary. The ternary mixture, in turn,

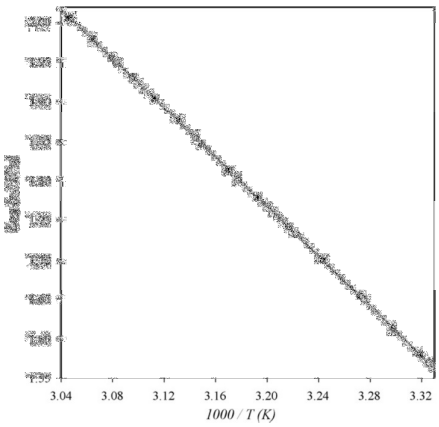

Fig. 6. Prediction of vapor pressure data. (—), Predicted by Eq. (4) and parameters reported in Table 6. Experimental data: (●), this work; (○), Ambrose et al. [25].

Table 7
Consistency test statistics for the binary systems MTBE (1) + acetone (2), and MTBE (1) + cyclohexane (3) at 94 kPa[a]

System	L_1[b]	$10^2 \times L_2$[b]	$100 \times \Delta y$[c]	δP[d] (kPa)
1 + 2	0.663	1.553	0.1	0.08
1 + 3	0.276	1.422	0.5	0.06

[a] The corresponding Legendre parameters for acetone (2) + cyclohexane (3) have been taken from ref. [17].
[b] Parameters for the Legendre polynomial [27] used in consistency.
[c] Average absolute deviation in vapor phase mole fractions $\Delta y = (1/N) \sum_{i=1}^{N} |y_i^{exp} - y_i^{cal}|$.
[d] Average absolute deviation in vapor pressure $\delta P = (1/N) \sum_{i=1}^{N} |P_i^{exp} - P_i^{cal}|$.

also exhibits positive deviation from ideal behavior, and no ternary azeotrope is observed.

The VLE data reported in Tables 2 and 3 for the binary systems were found to be thermodynamically consistent by the point-to-point test of Van Ness et al. [26], as modified by Fredenslund et al. [27]. For each mixture, the consistency criterion ($\Delta y < 0.01$) was met by fitting the equilibrium vapor pressure according to the Barker's reduction method [28]. Statistical analysis reveals that a two-parameter Legendre polynomial is adequate for fitting the equilibrium vapor pressure in the case of MTBE binary mixtures. Pertinent consistency statistics and Legendre polynomial parameters are presented in Table 7.

The consistency of the VLE data reported in Table 4 for the ternary system MTBE (1) + acetone (2) + cyclohexane (3) was tested by considering the model-free approach proposed by Lam et al. [29,30]. In this latter approach, the boiling temperatures of the ternary system have been correlated from the following empirical model [30]

$$T = \frac{\sum_{i=1}^{3} x_i \Delta H_i^{\circ}/R}{\sum_{i=1}^{3} x_i \Delta H_i^{\circ}/RT_i^0 - \Omega} \quad (5)$$

where ΔH_i° is the enthalpy of vaporization of pure components, T_i^0 is the boiling temperature of pure components at the pressure of the system, R is the gas constant, and Ω is given by the following Redlich–Kister type expansion on liquid phase mole fractions:

$$\Omega = \sum_{j>i}^{3} x_i x_j (A_{ij} + B_{ij}\Delta x_{ij} + C_{ij}\Delta x_{ij}^2 + D_{ij}\Delta x_{ij}^3 + E_{ij}\Delta x_{ij}^4 + F_{ij}\Delta x_{ij}^5 + G_{ij}\Delta x_{ij}^6 + H_{ij}\Delta x_{ij}^7) + x_1 x_2 x_3 \left(Q_{00} + x_1 Q_{11} + x_2 Q_{12} + \sum_{k\geq 2} [Q_{k1}\Delta x_{12}^k + Q_{k2}\Delta x_{13}^k + Q_{k3}\Delta x_{23}^k] \right) \quad (6)$$

where $\Delta x_{ij} = x_i - x_j$. As indicated in ref. [30], Eq. (5) is capable to fit the boiling temperatures of the ternary system and its constituent binaries within the range of experimental errors for T–x determinations. In addition, for mixtures that exhibit positive azeotropy, fitting constraints are required in order to avoid non-physical results when numerically calculating excess properties [30,31]. The various constants required in Eqs. (5) and (6), together with the correlation statistics for the case of the binary and ternary systems reported in this work, are presented in Table 8. As in the present case, once a satisfactory T–x fit has been obtained, the indicated model-free approach is able to calculate theoretical activity coefficients and vapor phase mole fraction of isobaric mixtures by

Table 8
Parameters and correlation statistics for the bubble temperatures of the system MTBE (1) + acetone (2) + cyclohexane (3) at 94.00 kPa

Parameters	Binary system		
	1 + 2	1 + 3	2 + 3[c]
Binary parameters for Eq. (6)			
A_{ij}	−0.650980	−0.596840	−1.900389
B_{ij}	0.018811	0.269075	1.184309
C_{ij}	−0.202902	−0.107638	−1.510760
D_{ij}	−0.004228	0.012969	0.925375
E_{ij}	−0.102006		−0.626615
F_{ij}			0.379153
G_{ij}			−1.564524
H_{ij}			0.949425
ΔT (K)[a]	0.01	0.02	0.01
$_T$ (K)[b]	0.02	0.02	0.02
Ternary parameters for Eq. (6)			
Q_{00}	−0.677222	Q_{23}	−2.633005
Q_{11}	−0.626807	Q_{31}	−0.637519
Q_{12}	2.837030	Q_{32}	1.079213
Q_{21}	−0.940037	Q_{33}	4.202784
Q_{22}	0.672507		
ΔT (K)[a]	0.03		
$_T$ (K)[b]	0.04		
Component		ΔH_i°[d] (J mol^{-1})	
Pure component heats of vaporization			
1		29594	
2		30830	
3		31714	

[a] Average absolute deviation, $\Delta T = 100/N \sum |T_i^{exp} - T_i^{cal}|$.
[b] Standard deviation.
[c] Parameters taken from ref. [17].
[d] Heats of vaporization calculated from the Antoine equations presented in Table 6 at the boiling temperatures of pure species at 94.00 kPa.

numerically integrating the Gibbs–Duhem equation. For this latter purpose, and considering the isobaric condition of the present VLE measurements, it has been assumed that the enthalpies of mixing of the binary and ternary mixtures (which are required by the isobaric application of the present model-free approach [30]) are well predicted by the UNIFAC group contribution method [32].

Figs. 1–4 depict the comparison of the experimental data and predicted results for the VLE and activity coefficients of the binary systems, as obtained from the model-free data treatment. Particularly, from Figs. 1 and 3, it is possible to observe that the model-free technique is able to predict VLE in a very good agreement with the experimental data. In addition, the predicted activity coefficients (Figs. 2 and 4) are in excellent agreement with the experimental data obtained for the MTBE (1) + acetone (2) mixture and in fair good agreement with the experimental data for the MTBE (1) + cyclohexane (3) mixture. Fig. 5 displays the map of isotherms of the ternary system as obtained from Eq. (5), allowing concluding that, although the binaries that contain acetone exhibit positive azeotropy (see points A and B in the Fig. 5), no ternary azeotrope is present in the mixture.

Fig. 7 depicts the vapor phase mole fraction residuals calculated from the model-free data treatment approach. According to the quoted figure, the overall deviations satisfy the point-to-point consistency criteria proposed by Fredenslund et al. and are within the order of magnitude of the reported experimental uncertainties for mole fractions ($\delta y_1 = 0.001$, $\delta y_2 = 0.003$). However, as also shown in Fig. 7, although residuals tend to scatter randomly around zero, they are slightly biased toward an over-prediction of the vapor-phase concentration for acetone. The numerically calcu-

Table 7
Consistency test statistics for the binary systems MTBE (1) + acetone (2), and MTBE (1) + cyclohexane (3) at 94 kPa[a]

System	L_1[b]	$10^2 \times L_2$[b]	$100 \times \Delta y$[c]	δP[d] (kPa)
1 + 2	0.663	1.553	0.1	0.08
1 + 3	0.276	1.422	0.5	0.06

[a] The corresponding Legendre parameters for acetone (2) + cyclohexane (3) have been taken from ref. [17].
[b] Parameters for the Legendre polynomial [27] used in consistency.
[c] Average absolute deviation in vapor phase mole fractions $\Delta y = (1/N) \sum_{i=1}^{N} |y_i^{exp} - y_i^{cal}|$.
[d] Average absolute deviation in vapor pressure $\delta P = (1/N) \sum_{i=1}^{N} |P_i^{exp} - P_i^{cal}|$.

also exhibits positive deviation from ideal behavior, and no ternary azeotrope is observed.

The VLE data reported in Tables 2 and 3 for the binary systems were found to be thermodynamically consistent by the point-to-point test of Van Ness et al. [26], as modified by Fredenslund et al. [27]. For each mixture, the consistency criterion ($\Delta y < 0.01$) was met by fitting the equilibrium vapor pressure according to the Barker's reduction method [28]. Statistical analysis reveals that a two-parameter Legendre polynomial is adequate for fitting the equilibrium vapor pressure in the case of MTBE binary mixtures. Pertinent consistency statistics and Legendre polynomial parameters are presented in Table 7.

The consistency of the VLE data reported in Table 4 for the ternary system MTBE (1) + acetone (2) + cyclohexane (3) was tested by considering the model-free approach proposed by Lam et al. [29,30]. In this latter approach, the boiling temperatures of the ternary system have been correlated from the following empirical model [30]

$$T = \frac{\sum_{i=1}^{3} x_i \Delta H_i^{\circ}/R}{\sum_{i=1}^{3} x_i \Delta H_i^{\circ}/RT_i^0 - \Omega} \quad (5)$$

where ΔH_i° is the enthalpy of vaporization of pure components, T_i^0 is the boiling temperature of pure components at the pressure of the system, R is the gas constant, and Ω is given by the following Redlich–Kister type expansion on liquid phase mole fractions:

$$\Omega = \sum_{j>i}^{3} x_i x_j (A_{ij} + B_{ij}\Delta x_{ij} + C_{ij}\Delta x_{ij}^2 + D_{ij}\Delta x_{ij}^3 + E_{ij}\Delta x_{ij}^4 + F_{ij}\Delta x_{ij}^5 + G_{ij}\Delta x_{ij}^6 + H_{ij}\Delta x_{ij}^7) + x_1 x_2 x_3 \left(Q_{00} + x_1 Q_{11} + x_2 Q_{12} + \sum_{k\geq 2} [Q_{k1}\Delta x_{12}^k + Q_{k2}\Delta x_{13}^k + Q_{k3}\Delta x_{23}^k] \right) \quad (6)$$

where $\Delta x_{ij} = x_i - x_j$. As indicated in ref. [30], Eq. (5) is capable to fit the boiling temperatures of the ternary system and its constituent binaries within the range of experimental errors for T–x determinations. In addition, for mixtures that exhibit positive azeotropy, fitting constraints are required in order to avoid non-physical results when numerically calculating excess properties [30,31]. The various constants required in Eqs. (5) and (6), together with the correlation statistics for the case of the binary and ternary systems reported in this work, are presented in Table 8. As in the present case, once a satisfactory T–x fit has been obtained, the indicated model-free approach is able to calculate theoretical activity coefficients and vapor phase mole fraction of isobaric mixtures by

Table 8
Parameters and correlation statistics for the bubble temperatures of the system MTBE (1) + acetone (2) + cyclohexane (3) at 94.00 kPa

Parameters	Binary system		
	1 + 2	1 + 3	2 + 3[c]
Binary parameters for Eq. (6)			
A_{ij}	−0.650980	−0.596840	−1.900389
B_{ij}	0.018811	0.269075	1.184309
C_{ij}	−0.202902	−0.107638	−1.510760
D_{ij}	−0.004228	0.012969	0.925375
E_{ij}	−0.102006		−0.626615
F_{ij}			0.379153
G_{ij}			−1.564524
H_{ij}			0.949425
ΔT (K)[a]	0.01	0.02	0.01
$_T$ (K)[b]	0.02	0.02	0.02
Ternary parameters for Eq. (6)			
Q_{00}	−0.677222	Q_{23}	−2.633005
Q_{11}	−0.626807	Q_{31}	−0.637519
Q_{12}	2.837030	Q_{32}	1.079213
Q_{21}	−0.940037	Q_{33}	4.202784
Q_{22}	0.672507		
ΔT (K)[a]	0.03		
$_T$ (K)[b]	0.04		
Component		ΔH_i°[d] (J mol^{-1})	
Pure component heats of vaporization			
1		29594	
2		30830	
3		31714	

[a] Average absolute deviation, $\Delta T = 100/N \sum |T_i^{exp} - T_i^{cal}|$.
[b] Standard deviation.
[c] Parameters taken from ref. [17].
[d] Heats of vaporization calculated from the Antoine equations presented in Table 6 at the boiling temperatures of pure species at 94.00 kPa.

numerically integrating the Gibbs–Duhem equation. For this latter purpose, and considering the isobaric condition of the present VLE measurements, it has been assumed that the enthalpies of mixing of the binary and ternary mixtures (which are required by the isobaric application of the present model-free approach [30]) are well predicted by the UNIFAC group contribution method [32].

Figs. 1–4 depict the comparison of the experimental data and predicted results for the VLE and activity coefficients of the binary systems, as obtained from the model-free data treatment. Particularly, from Figs. 1 and 3, it is possible to observe that the model-free technique is able to predict VLE in a very good agreement with the experimental data. In addition, the predicted activity coefficients (Figs. 2 and 4) are in excellent agreement with the experimental data obtained for the MTBE (1) + acetone (2) mixture and in fair good agreement with the experimental data for the MTBE (1) + cyclohexane (3) mixture. Fig. 5 displays the map of isotherms of the ternary system as obtained from Eq. (5), allowing concluding that, although the binaries that contain acetone exhibit positive azeotropy (see points A and B in the Fig. 5), no ternary azeotrope is present in the mixture.

Fig. 7 depicts the vapor phase mole fraction residuals calculated from the model-free data treatment approach. According to the quoted figure, the overall deviations satisfy the point-to-point consistency criteria proposed by Fredenslund et al. and are within the order of magnitude of the reported experimental uncertainties for mole fractions ($\delta y_1 = 0.001$, $\delta y_2 = 0.003$). However, as also shown in Fig. 7, although residuals tend to scatter randomly around zero, they are slightly biased toward an over-prediction of the vapor-phase concentration for acetone. The numerically calcu-

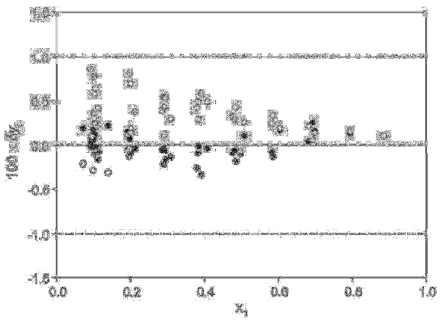

Fig. 7. Vapor phase mole fraction residuals for the ternary system MTBE (1) + acetone (2) + cyclohexane (3) at 94.00 kPa: (●), δy_1; (○), δy_2.

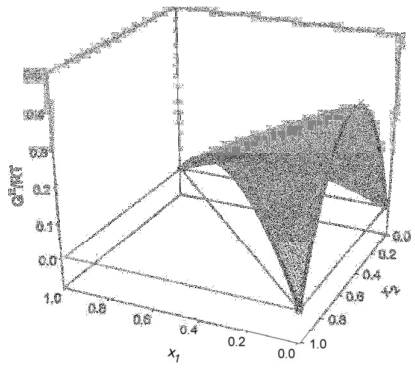

Fig. 8. Excess Gibbs energy function for the ternary system MTBE (1) + acetone (2) + cyclohexane (3) at 94.00 kPa: (—), as calculated from the model-free data treatment for ternary systems.

lated G^E function of the ternary is presented in Fig. 8, which clearly confirms that the mixture exhibits positive deviations from ideal behavior.

The activity coefficients for the binary system were correlated with the Redlich–Kister expansion [33]

$$\frac{G^E}{RT} = \sum_{i=0}^{2}\sum_{j>i}^{2} x_i x_j [b_{ij} + c_{ij}(x_i - x_j) + d_{ij}(x_i - x_j)^2] \quad (7)$$

where b_{ij}, c_{ij} and d_{ij} are the constants for the ij binary. All the constants in Eq. (7) are assumed to be temperature-independent. The Redlich–Kister coefficients for the binaries were obtained by a Simplex optimization technique and the results are shown in Table 9. In addition, ternary data were predicted from the binary systems. From Table 9, it is possible to observe that the equilibrium vapor pressures and vapor phase mole fractions of the ternary system were well predicted by the Redlich–Kister equation when using only the binary constants.

The VLE data for the binary systems reported in Tables 2 and 3 were also correlated with the NRTL, Wilson and UNIQUAC [34] equations, whose adjustable parameters were obtained by minimizing the following objective function (OF):

$$\mathrm{OF} = \sum_{i=1}^{N}\left(\frac{|P_i^{exp} - P_i^{cal}|}{P_i^{exp}} + |y_i^{exp} - y_i^{cal}|\right)^2 \quad (8)$$

Pertinent parameters are reported in Table 10, together with the relative deviation for the case of bubble- and dew-point pressures.

From the results presented in Table 10, it is possible to conclude that all the fitted models gave a reasonable correlation of the binary systems and the best fit is obtained with the Wilson model. The capability of predicting simultaneously the bubble- and dew-point pressures and the vapor and liquid phase mole fractions, respectively, has been used as the ranking factor. In order to establish the coherency of the present binary data and to test the predictive capability of the parameters reported in Table 10, we have used the best ranked model (Wilson's model) to predict the binary VLE data reported in other sources. Figs. 9 and 10 allow one to conclude that a good agreement between the predicted and the experimental data reported by other authors at other temperature conditions is obtained. Finally, similar to the

Table 9
Constants for the Redlich–Kister model, fit, correlation and prediction statistics[a]

Binary data (parameters for Eq. (7))						
System	b_{ij}			$10^2 \times c_{ij}$		
1 + 2	0.663			1.553		
1 + 3	0.276			1.422		
VLE correlation and predictions						
System	Bubble point pressures			Dew point pressures		
	ΔP (%)[b]	$100 \times \Delta y_1$[c]	$100 \times \Delta y_2$	ΔP (%)	$100 \times \Delta x_1$	$100 \times \Delta x_2$
1 + 2	0.09	0.1	0.1	0.08	0.1	0.1
1 + 3	0.07	0.5	–	0.41	0.5	–
1 + 2 + 3[d]	0.23	0.1	0.2	0.21	0.1	0.3

Systems MTBE (1) + acetone (2), and MTBE (1) + cyclohexane (3) at 94 kPa.

[a] The corresponding Redlich–Kister parameters and VLE correlation and predictions for acetone (2) + cyclohexane (3) have been taken from ref. [17].

[b] Average percentage deviation in pressure $\Delta P = (100/N)\sum_i^N |P_i^{exp} - P_i^{cal}|/P_i^{exp}$.

[c] Average absolute deviation in mole fraction $\Delta y = 1/N\sum_i^N |y_i^{exp} - y_i^{cal}|$.

[d] Prediction from binary parameters.

Table 10
Parameters and prediction statistics for different G^E models in MTBE (1) + acetone (2) + cyclohexane (3)[a]

Model	System	A_{ij}	A_{ji}	α_{ij}	Bubble-point pressures			Dew-point pressures		
					ΔP (%)[e]	$100 \times \Delta y_1$[f]	$100 \times \Delta y_2$	ΔP (%)	$100 \times \Delta x_1$[f]	$100 \times \Delta x_2$
NRTL[b]	1+2	1196.9	681.4	0.3	0.10	0.1	0.1	0.09	0.1	0.1
	1+3	667.1	140.5	0.3	0.09	0.5	...	0.51	0.6	...
	2+3	2102.7	3029.6	0.3	0.63	0.4	–	0.73	1.1	–
	1+2+3				0.34	0.1	0.3	0.35	0.2	0.5
Wilson[b,c]	1+2	−780.8	2742.3	–	0.11	0.1	0.1	0.10	0.1	0.1
	1+3	186.8	628.4	...	0.08	0.5	...	0.52	0.6	...
	2+3	4432.9	1421.8	–	0.15	0.3	–	0.53	0.6	–
	1+2+3				0.21	0.1	0.1	0.27	0.1	0.2
UNIQUAC[b,d]	1+2	1636.8	664.1	...	0.11	0.1	0.1	0.09	0.1	0.1
	1+3	74.1	73.8	–	0.15	0.6	–	0.54	0.7	–
	2+3	−234.6	2250.4	–	0.71	0.5	–	0.80	1.2	–
	1+2+3				0.26	0.2	0.3	0.24	0.2	0.4

[a] The corresponding parameters for G^E, and their statistics for acetone (2) + cyclohexane (3) have been taken from ref. [17].
[b] Parameters in J mol^{-1}.
[c] Liquid molar volumes have been estimated from the Rackett equation [22].
[d] Molecular parameters are those calculated from UNIFAC [27,32] using the following r an q parameters: $r_1 = 4.0678$, $r_2 = 2.573$, $r_3 = 4.046$, $q_1 = 3.632$, $q_2 = 2.336$, $q_3 = 3.240$.
[e] $\Delta P = (100/N)\sum_i^N |P_i^{exp} - P_i^{cal}|/P_i^{exp}$.
[f] $\Delta\delta = 1/N\sum_i^N |\delta_i^{exp} - \delta_i^{cal}|$ with $\delta = y$ or x.

trend of the results presented in Table 9, Table 10 shows that the binary contributions allow a reasonable prediction of the ternary system.

3.2. Interfacial tension data

The interfacial tension measurements at $T = 303.15$ K and $P = 101.3$ kPa are reported in Tables 11 and 12. From these results, it is observed that the interfacial tensions of the ternary mixture and its constituent binary systems exhibit negative deviation from linear behavior ($\sum x_i \ _i$). Neither the MTBE based binary mixtures nor the ternary system exhibited aneotropy at the experimental conditions.

The experimental IFT data were correlated using the following Redlich–Kister expansion [35]

$$= \left\{ \sum_{i=0}^{3} \sum_{j>i}^{3} x_i x_j [b_{ij} + c_{ij}(x_i - x_j) + d_{ij}(x_i - x_j)^2] \right.$$

$$\left. + x_1 x_2 x_3 [C + D_1 x_1 + D_2 x_2] \right\} + \sum_{k=1}^{3} \ _k x_k \quad (9)$$

where is the interfacial tension of the mixture, while $_k$ is the interfacial tension of the pure components. b_{ij}, c_{ij} and d_{ij} are the con-

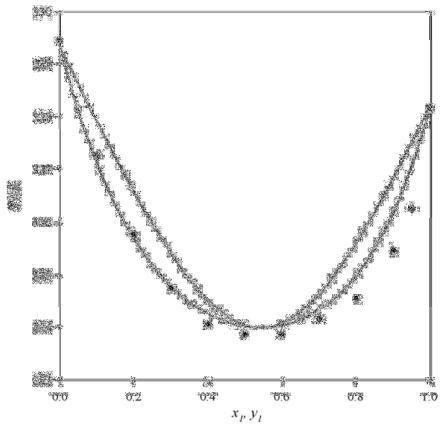

Fig. 9. Isobaric phase diagram for the system MTBE (1) + acetone (2) at 101 kPa. (—), Predicted from the Wilson model with the parameters indicated in Table 10. (●), Experimental data reported by Churkin et al. [12].

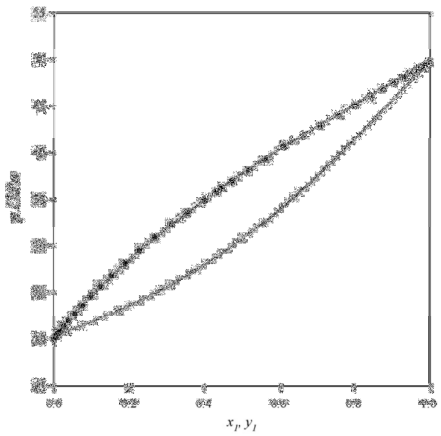

Fig. 10. Isothermal phase diagram for the system MTBE (1) + cyclohexane (3) at 308.15 K. (—), Predicted from the Wilson model with the parameters indicated in Table 10. (●), Experimental data reported by del Rio et al. [11].

Table 11
Experimental interfacial tensions for MTBE binary systems at 303.15 K and 101.3 kPa

MTBE (1) + acetone (2)		MTBE (1) + cyclohexane (3)	
x_1	σ (mN m^{-1})	x_1	σ (mN m^{-1})
0.031	22.14	0.046	23.39
0.074	21.76	0.100	22.97
0.171	21.13	0.205	22.23
0.272	20.59	0.308	21.57
0.378	20.09	0.409	21.03
0.484	19.75	0.510	20.58
0.585	19.47	0.614	20.12
0.681	19.22	0.716	19.71
0.784	18.98	0.816	19.34
0.884	18.74	0.901	19.05
0.940	18.55	0.947	18.89

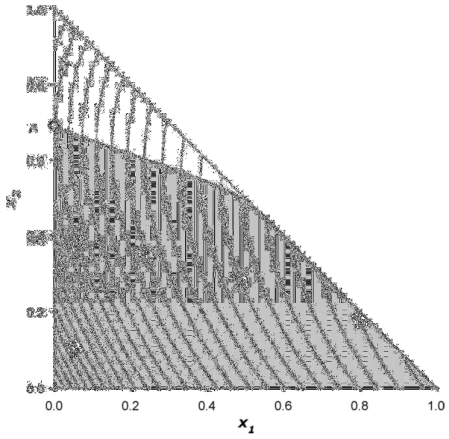

Fig. 11. Isotension plot for the ternary system MTBE (1) + acetone (2) + cyclohexane (3) at 303.15 K and 101.3 kPa: (—), smoothed with Eq. (9) and the coefficients given in Table 13.

stants for the ij binary, and C, D_1 and D_2 are ternary constants. The Redlich–Kister coefficients for the MTBE binaries and the values of the constants C, D_1 and D_2 for the ternary mixture were obtained by a Simplex optimization technique and pertinent results are shown in Table 13. Statistical analysis revealed that the ternary constants C, D_1 and D_2 were not significant, suggesting that the ternary IFT data can be predicted directly from the binary contributions. In fact, the interfacial tensions of the ternary system were well predicted by the Redlich–Kister equation when using only the binary constants and the maximum deviation observed over the whole mole fraction range was 0.49 mN m^{-1}. Finally, Fig. 11 displays the isotension map of the ternary system as obtained from Eq. (9). From this latter figure, it is possible to conclude that the acetone + cyclohexane system exhibits negative aneotropy only (see point A), and that no ternary aneotrope is present in the mixture. The shaded region in Fig. 11 indicates the range of mole fractions where the addition of acetone to the ternary mixtures implies reduction of interfacial tensions.

Table 12
Experimental interfacial tensions for the ternary system MTBE (1) + acetone (2) + cyclohexane (3) at 303.15 K and 101.3 kPa

x_1	x_2	σ (mN m^{-1})
0.394	0.089	20.89
0.182	0.089	21.95
0.288	0.089	21.33
0.497	0.090	20.30
0.601	0.093	19.88
0.080	0.093	22.58
0.703	0.094	19.46
0.801	0.099	19.13
0.430	0.189	20.46
0.540	0.190	19.97
0.745	0.194	19.22
0.315	0.195	20.97
0.643	0.196	19.57
0.201	0.196	21.52
0.081	0.201	22.20
0.037	0.287	22.38
0.124	0.299	21.85
0.229	0.307	21.33
0.349	0.311	20.76
0.480	0.312	20.12
0.614	0.318	19.55
0.149	0.378	21.89
0.568	0.401	19.70
0.352	0.405	20.64
0.468	0.406	20.11
0.217	0.416	21.23
0.055	0.431	21.96
0.403	0.497	20.29
0.093	0.500	21.82
0.298	0.500	20.83
0.195	0.500	21.36
0.029	0.514	22.10
0.124	0.528	21.58
0.247	0.535	20.99
0.392	0.553	20.30
0.308	0.603	20.74
0.202	0.603	21.15
0.095	0.604	21.63
0.086	0.712	21.86
0.195	0.715	21.31
0.092	0.821	21.94

4. Conclusions

Isobaric vapor–liquid equilibrium data at 94 kPa and atmospheric interfacial tensions at 303.15 K have been reported for binary and ternary mixtures that contain MTBE, acetone, and/or cyclohexane. Experimental results revealed that the phase equilibrium data of ternary mixture and its MTBE based binaries exhibit positive deviations from ideal behavior, and azeotropy was observed for the MTBE with acetone binary mixture. The interfacial tensions of the ana-

Table 13
Coefficients and deviations (maximum, average and standard) obtained in correlation of interfacial tension, Eq. (9), for binary systems of the ternary system MTBE (1) + acetone (2) + cyclohexane (3) at 303.15 K and 101.3 kPa

System	b_{ij} (mN m^{-1})	c_{ij} (mN m^{-1})	d_{ij} (mN m^{-1})	Maximum deviation ($10^3 \times$ mN m^{-1})	Average deviation ($10^3 \times$ mN m^{-1})	Standard deviation ($10^3 \times$ mN m^{-1})
1 + 2	−3.2087	0.6850	−0.6332	4.21	0.82	1.13
1 + 3	−2.9887	1.7336	−1.7094	2.98	0.40	0.79
2 + 3[a]	−4.3658	0.0691	−0.1415	2.09	0.46	0.58

[a] The binary parameters for the system acetone (2) + cyclohexane (3) were taken from ref. [17].

lyzed mixtures exhibit negative deviation from linear behavior.

The consistency of the present ternary VLE data was tested using a model-free data treatment approach that numerically calculated the Gibbs excess energy from experimental T–x data. The theoretical predictions of vapor phase mole fractions and activity coefficients are in excellent agreement with the reported experimental data, for both binary and ternary mixtures.

The activity coefficients and boiling points of all the binary mixtures were well correlated with the mole fraction using the NRTL, Wilson and UNIQUAC equations, the best fit corresponding to the Wilson model. The interfacial tensions of the binary mixtures were smoothed using the Redlich–Kister equation. From these models it is possible to conclude that the binary contributions allow a reasonable prediction of the VLE of the properties of the ternary system.

List of symbols

A_i, B_i, C_i	Antoine's equation parameters in Eq. (4)
A_{ij}, B_{ij}, C_{ij}	Redlich–Kister parameters in Eq. (6)
b_{ij}, c_{ij}, d_{ij}	Redlich–Kister parameters in Eqs. (7) and (9)
B_{ii}	second virial coefficients of the pure gases ($cm^3\ mol^{-1}$)
B_{ij}	cross second virial coefficient ($cm^3\ mol^{-1}$)
C	Redlich–Kister parameter, Eq. (9)
D_1, D_2	Redlich–Kister parameters, Eq. (9)
ΔH_i°	enthalpy of vaporization of pure components ($J\ mol^{-1}$)
n_D	refractive index
N	number of data points
P	absolute pressure (kPa)
P^0	pure component vapor pressure (kPa)
Q_{ij}	Redlich–Kister parameter in Eq. (6)
r_i	radii of probe orifice i (mm)
R	universal gas constant ($J\ mol^{-1}\ K^{-1}$)
T_i^0	boiling temperature of pure component i at the pressure of the system (K)
T	absolute temperature (K)
v	voltage (V)
V	volume ($cm^3\ mol^{-1}$)
x, y	fractions of the liquid and vapor phases

Greek letters

Δ	differential
Γ_{ji}	Gibbs adsorption of species j in species i
Ω	Redlich–Kister expansion, Eq. (5)
δ	mixing rule of second virial coefficients
	activity coefficient
	solvation parameter
	density ($g\ cm^{-3}$)
	interfacial tension ($mN\ m^{-1}$)

Superscripts

cal	calculate
exp	experimental
L	pertaining to the liquid phase
0	reference state (pure component)

Subscripts

1, 2	number of orifice
b	normal boiling points
i, j	component i, j, respectively

Acknowledgment

This work was financed by FONDECYT, Santiago, Chile (Project 1080596).

References

[1] E. Weber de Menezes, R. da Silva, R. Cataluna, R.J.C. Ortega, Fuel 85 (2006) 815–822.
[2] E. Weber de Menezes, R. Cataluna, D. Samios, R. da Silva, Fuel 85 (2006) 2567–2577.
[3] F. Gonzalez, United States Patent #5,141 (1992) 524.
[4] D. Jóźwiak, A. Szlek, J. Energy Inst. 80 (2007) 35–39.
[5] P.A. de Pereira, L.M.B. Santos, E.T. Sousa, J.B. de Andrade, J. Braz. Chem. Soc. 15 (2004) 646–651.
[6] F.E. Ahmed, Toxicol. Lett. 123 (2001) 89–113.
[7] K.N. Marsh, P. Niamskul, J. Gmehling, R. Bölts, Fluid Phase Equilib. 156 (1999) 207–227.
[8] C.R. Chamorro, M.C. Martín, M.A. Villamañán, J.J. Segovia, Fluid Phase Equilib. 220 (2004) 105–112.
[9] A. del Río, S. Horstmann, J.A.R. Renuncio, J. Gmehling, J. Chem. Eng. Data 46 (2001) 1181–1187.
[10] J.J. Segovia, M.C. Martín, C.R. Chamorro, M.A. Villamañán, Fluid Phase Equilib. 133 (1997) 163–172.
[11] A. del Río, B. Coto, C. Pando, J.A.R. Renuncio, Phys. Chem. Chem. Phys. 1 (1999) 4995–4998.
[12] V.N. Churkin, V.A. Gorshkov, S. Yu Pavlov, M.E. Basner, Promst. Sint. Kauch. 4 (1979) 2–4.
[13] J. Gmehling, R. Bölts, J. Chem. Eng. Data 41 (1996) 202–209.
[14] B. Coto, F. Mößner, C. Pando, R.G. Rubio, J.A.R. Renuncio, J. Chem. Soc., Faraday Trans. 92 (1996) 4435–4440.
[15] A. Mejía, H. Segura, M. Cartes, P. Bustos, Fluid Phase Equilib. 255 (2007) 121–130.
[16] A. Mejía, H. Segura, M. Cartes, Phys. Chem. Liq. 46 (2008) 185–200.
[17] A. Mejía, H. Segura, M. Cartes, C. Calvo, Fluid Phase Equilib. 270 (2008) 75–86.
[18] T.E. Daubert, R.P. Danner, Physical and thermodynamic properties of pure chemicals, in: Data Compilation, Taylor and Francis, Bristol, PA, 1989.
[19] A.W. Adamson, A.P. Gast, Physical Chemistry of Surfaces, Wiley Interscience, USA, 1997.
[20] A.I. Rusanov, V.A. Prokhorov, Interfacial Tensiometry, Elsevier, Amsterdam, 1996.
[21] H.C. Van Ness, M.M. Abbott, Classical Thermodynamics of Nonelectrolyte Solutions, McGraw-Hill Book Co., New York, 1982.
[22] H.G. Rackett, J. Chem. Eng. Data 15 (1970) 514–517.
[23] J. Hayden, J. O'Connell, Ind. Eng. Chem. Process Des. Dev. 14 (1975) 209–216.
[24] J.M. Prausnitz, T. Anderson, E. Grens, C. Eckert, R. Hsieh, J. O'Connell, Computer Calculations for Multicomponent Vapor–Liquid and Liquid–Liquid Equilibria, Prentice-Hall, New York, 1980.
[25] D. Ambrose, J.H. Ellender, H.S. Sprake, R. Townsend, J. Chem. Thermodyn. 8 (1976) 165–178.
[26] H.C. Van Ness, S.M. Byer, R.E. Gibbs, AIChE J. 19 (1973) 238–244.
[27] A. Fredenslund, J. Gmehling, P. Rasmussen, Vapor–Liquid Equilibria Using UNIFAC, A Group Contribution Method, Elsevier, Amsterdam, 1977.
[28] J.A. Barker, Aust. J. Chem. 6 (1953) 207–210.
[29] E. Lam, A. Mejía, H. Segura, J. Wisniak, S. Loras, Ind. Eng. Chem. Res. 40 (2001) 2134–2148.
[30] E. Lam, A. Mejía, H. Segura, J. Wisniak, S. Loras, Ind. Eng. Chem. Res. 40 (2001) 2149–2159.
[31] J. Wisniak, A. Apelblat, H. Segura, Chem. Eng. Sci. 52 (1997) 4393–4402.
[32] R. Wittig, J. Lohmann, J. Gmehling, Ind. Eng. Chem. Res. 42 (2003) 183–188.
[33] O. Redlich, A.T. Kister, Ind. Eng. Chem. 40 (1948) 341–345.
[34] J.M. Prausnitz, R.N. Lichtenthaler, E. Gomes de Azevedo, Molecular Thermodynamics of Fluid-Phase Equilibria, third ed., Prentice-Hall, New Jersey, 1999.
[35] D.B. Myers, R.L. Scott, Ind. Eng. Chem. 55 (1963) 43–46.

REFERENCIAS

Anderko, A., Fluid Phase Equilibria. 61 **(1990)** 145.

Aparicio, S. Hall, H.R., Ind. Eng. Chem. Res. 46 **(2007)** 273.

Aparicio, S. J., of Supercritical Fluids. 46 **(2008)** 10.

Bidart, C., Tesis de Magister, Departamento de Ingeniería Química, Universidad de Concepción, **(2007)**

Bidart, C., Segura, H., Wisniak, J., Ind. Eng. Chem. Res. 46 **(2007)** 947.

Blas, F. J., Vega, L. F. Molec. Phys.,92 **(1997)** 135.

Blas, F. J., Vega, L. F., J. Chem. Phys., 115 (8) **(2001)** 3906.

Blas, F. J., Vega, L. F., J. Chem. Phys., 115 (9) **(2001)** 4355.

Boshkov, L., Mazur, V., *Phys. Letters*, 104 **(1984)** 415.

Boshkov, L., Yelash, L., *Fluid Phase Equilibria*, 141 **(1997)** 105.

Brunner, E., J. Chem. Thermodyn., 17 **(1985)** 871.

Brunner, E., J. Chem. Thermodyn., 22 (1990) 335

Chang, C.J., Chang, Y., Lee, H., Ind. Eng. Chem. Res. 39 **(2000)** 4521.

Chapman, W. G., Jackson, J., Gubbins, K. E., Molec. Phys., 65 **(1988)** 1057.

Chapman, W.G., Gubbins, K. E., Jackson, G., Radosz, M., Ind. Eng. Chem. Res. 29 **(1990)** 1709.

Enick, R. *et* al, Fluid Phase Equilib., 22 **(1985)** 209

Fernández, J., Tesis de Magister, Departamento de Ingeniería Química, Universidad de Concepción, **(2003)**

Firoozabadi, A. Thermodynamics of hydrocarbon, McGraw-Hill **(1999)**.

Flores, M., Informe para Optar al Título de Ingeniero Civil Químico. Departamento de Ingeniería Química, Universidad de Concepción, **(2003)**

Flores, M., Segura, H, Mejia, A., J. of Supercritical Fluids, 48 **(2008)** 108.

Furman, D., Griffiths, R.B., Phys. Rev. A. 17 **(1978)** 1139.

García, J., Lugo, L., Fernández, J. Ind. Eng. Chem. Res. 43 **(2004)** 8345.

Gardner, J.W., Orr, F.M., Pet, J. , Tech, **(1981)** 2061.

Gaubert, M.A., Gerbaud, V., Joulia, X., Peyrigain, P. S., Ind. Eng. Chem. Res. 40 **(2001)** 2914.

Gross, J., Sadowski, G., Ind. Eng. Chem. Res., 40 **(2001)** 1244.

Guggenheim, E.A, Mixtures, Clarendon Press, Oxford, **(1952)**

Hauk, A., Weidner, E., Ind. Eng. Chem. Res, 39 **(2000)** 4646.

Henley, E. and Seader, J.D., Equilibrium-stage separation operations in chemical enginneering, Wiley & Sons **(1981)**.

Huang, S.H., Radosz, M., Ind. Eng. Chem. Res., 29 **(1990)** 2284.

Jackson, G., Villegas, G., Galindo, A., J.Chem. Phys., 106 **(1997)** 4168.

Johnson, J., Zollweg, J., Gubbins, K. E., Molec. Phys., 78 **(1993)** 591.

Van Konynenburg, P. H., PhD Thesis, UCLA **(1968)**.

Van Konynenburg, P.H., Scott, R.L., Phil. Trans. R. Soc. London. 298 **(1980)** 495.

Kamerlingh Onnes, H. Proc. Kon. Akad (Común. Phys. Lab.Leiden 96). 9 **(1906a)** 459.

Kamerlingh Onnes, H., Keesom, W.H., Proc. Kon. Akad (Común. Phys. Lab.Leiden 96b). 9 **(1906b)** 501.

Kamerlingh Onnes, H., Keesom, W.H., Proc. Kon. Akad (Común. Phys. Lab.Leiden Suppl. 15). 9 **(1906c)** 786.

Kamerlingh Onnes, H., Keesom, W.H., Proc. Kon. Akad (Común. Phys. Lab.Leiden Suppl. 16). 10 **(1907)** 274.

Karakatsani, E.K., Peters, C.J, Economou, I.G., J. Phys. C., 111 **(2007)** 15487.

Van der Kooi, H. J, PhD. Thesis, The technical university of Delft, Netherlands, **(1981)**.

Kolafa, J., Phys. Chem. Chem. Phys., 1 **(1999)** 5665.

Kolafa, J., Bumba, J., Phys. Chem. Chem. Phys. 6 **(2004)** 2301.

Kraska, T. and Yelash, L. V., Phys. Chem. Chem. Phys. 1 **(1999)** 4315.

Loos, Th. W., van der Steen, J., Fluid Phase Equilibria, 51 **(1989)** 353

Maier, V.W., Saupe, A., Z. Naturforsch., 13a **(1958)** 564

Maier, V.W., Saupe, A., Z. Naturforsch., 14a **(1959)** 882

Maier, V.W., Saupe, A., Z. Naturforsch., 15a **(1960)** 287

McHugh, M., Krukonis, V., Supercritical fluid extraction, Butterworth-Heinemann, 2da Ed. **(1994)**.

Müller, E. A., Gubbins, K. E., Ind. Eng. Chem. Res.,40 **(2001)** 2193.

Pamies, J.C., Dias, A. M., Marrucho, I. M., Coutinho, J. A. P., Vega, L. F. , Journal of Physical Chemistry B, 118 **(2004)** 1450.

Prausnitz, J.M., Molecular thermodynamics of fluid-phase equilibria, Prentice-Hall Inc., 2da Ed., **(1986)**.

Peters, C.J., Economou, I.G., J. Phys. B, 110 **(2006)** 9262.

Quiñones-Cisneros, S., Phys. Chem. Chem. Phys., 6 **(2004)** 2307

Quiñones-Cisneros, S. *et* al, International Journal of Refrigeration, 28 **(2005)** 714.

Sadus, R. and Wei, Y., AICHE J. 46 **(2000)** 169.

Scott, R. L., Van Konynenburg, P.H., Disc. Farad Soc., 49 **(1970)** 87.

Segura, H., Wisniak, J., Toledo P. G., Mejía A.. Fluid Phase Equilibria, 166 **(1999)** 141.

Segura, H., Wisniak, J., Toledo, P., Separata, (2001).

Segura, H., González, R., Polishuk, I., Vera, J., Phys. Chem. Chem. Phys., 6 **(2004)** 5189.

Thies, M.C., Burgess, W.A., Ind.Eng.Chem.Res., 46 **(2007)** 7018.

Topliss, R., PhD. Thesis, University of California, Berkley, **(1985)**.

Valderrama, J. O., Ind. Eng. Chem. Res. 42 **(2003)**1603.

Wertheim, M. S., J. Stat. Phys. 35 **(1984a)** 19.

Wertheim, M. S., J. Stat. Phys., 35 **(1984b)** 35.

Wertheim, M. S., J. Stat. Phys., 42 **(1986a)** 459.

Wertheim, M. S., J. Stat. Phys., 42 **(1986b)** 477.